Control of condensate shape and composition via chemical reaction networks

Dissertation
zur Erlangung des akademischen Grades
Doctor rerum naturalium

vorgelegt

der Fakultät Physik
Bereich Mathematik und Naturwissenschaften
der Technischen Universität Dresden

von

Giacomo Bartolucci
geboren am 21.02.1993 in Urbino, Italien

erstellt am

Max-Planck-Institut für Physik komplexer Systeme
Dresden, 2022

Gutachter:

Prof. Dr. Christoph A. Weber
Prof. Dr. Frank Jülicher, co-signed by Prof. Dr. Benjamin Friedrich

Acknowledgments

Is hard to find words to quantify my gratitude toward the people that accompanied me during this journey. First of all, I want to thank my supervisors Christoph Weber and Frank Jülicher. Christoph, from the very beginning, I felt deeply understood and supported by you. The enthusiasm you have transmitted to me shaped my way of approaching research. I am exceptionally grateful for the moments we lived doing research together but also outside of the working environment. I deeply value the resonance that developed between us. Frank, I feel enormously privileged for having the possibility of working with you. Your scientific rigour and your vast knowledge of the most diverse fields of physics are a continuous source of inspiration. I would also like to thank members of the CBG and CSBD, in particular, Patrick, Tyler, Giulia, Mareike, Riccardo and Katja for the coffee. I would like to thank all my collaborators: Alf Honigmann, Job Boekhoven, Dieter Braun and Christof Mast, Thomas Michaels, and all the members of their labs. In particular Isabel and Daxiao, Adriana and Philipp, and Carsten and Alex.

I want to thank all the present and past members of the Weber web, in particular Jacqueline, Sudarshana, Jonathan, Kafa, Ivar, Pranay, Xueping, Susanne, Lars, Argo, Archi and Yash. Not only you contributed to creating an amazing scientific environment but were also wonderful companions during the many group activities. I want to thank all members of the biophysics division that I had the pleasure to interact with, especially Johanna, Adolfo, Daniel, Russland, Aida, Kathrin, Christian, Omar, Martin, Charlie, Aboutaleb, Stefano, Alvaro, Felix, Ivan, Matteo and of course my spectacular office mate Fabrizio. Special thanks go to Stefano, Sudarshana, Jonathan, and of course Christoph for their great comments on my thesis. Finally, I would like to thank Ulrike, Anna, Rita and Elise for making the environment at PKS so enjoyable and friendly.

I want to thank my father, my mother, my awesome brother and all my family, for their patience and constant care. I want to thank those who have been my second family in Dresden, namely the members of my WG and the crew of Banda Comunale. I want to thank friends I always counted on, especially Marco, Elisa, Simone, Francesca, Giovanni, Emma, Marco Signoretti e Marco Stuani, Luca, Angela, Matteo, Fabio and Jacopo. Finally, I want to express deep gratitude for the existence of Fabrizio, Alberto, Ivan, Filippo, Julia, Felix, Antonio, Anthony, Eleonora, Irina, Monica, Cate, Marti, Laura, James and Gabriel.

Given the number of people I wanted to thank (and I have for sure forgotten many important names), I could not spend a word for each of them. I will make sure, however, to keep these bonds alive and to show practically my gratitude to every single one of you.

Abstract

Interactions among the multitude of macromolecules populating the cytoplasm can lead to the emergence of coexisting phases formed via phase separation. This phenomenon plays a crucial role in the spatial organization of cells and the regulation of their functions. Many of the molecules that drive phase separation can undergo transitions among different states. Proteins, for example, can go through conformational transitions and switch among different phosphorylation states. In addition, proteins that are relevant for phase separation can assemble into oligomers of different sizes. Both molecular transitions and oligomerization can be described as chemical reactions in the context of theories that account for phase separation in multicomponent mixtures. In this work, we discuss how chemical reactions can be used to control coexisting phase composition and shape. In particular, focusing on molecular transitions among two states of a protein, we find a discontinuous thermodynamic phase transition in the composition of the protein-dense phase, as a function of temperature. Breaking detailed balance of the molecular transition by continuous fuel addition can also be used to control the number of distinct coexisting phases and their composition. Additionally, fuel turnover can lead to the emergence of novel patterns as the system approaches a non-equilibrium stationary state. We focus on the mechanism that leads to the formation of ring-like patterns, motivated by the observation of similar shapes in experiments with chemical reaction cycles coupled to a fuel reservoir. We propose that, due to chemical reactions, the composition at the centre of the dense phase can be altered, leading to an instability that drives the formation of a new interface.

Controlling the composition of coexisting phases becomes crucial when the number of components and the number of reactions among them rises. This is the case in mixtures containing proteins that can be found in a monomeric state but also form aggregates of arbitrary size. We characterise the equilibrium of such systems in the limit of maximum aggregate size going to infinity. For systems that phase separate, we show that the aggregate size distribution can be different in each of the coexisting phases and is determined by the temperature and the energy of bonds between monomers. Mixtures composed of disk-like or spherical aggregates can undergo a gelation transition. Gelation can be considered as a special case of phase coexistence between a dilute phase (the ”sol”) containing aggregates of finite size, and a “gel” phase, corresponding to an aggregate of infinite size. Lowering the temperature leads to a transition from two coexisting ”sol” phases to the coexistence of a “sol” phase and a ”gel” phase. In summary, this work provides a theoretical framework to study phase-separating systems composed of many components that undergo chemical reactions. Furthermore, we discuss how to exploit such reactions to control the composition of coexisting phases.

Zusammenfassung

Wechselwirkungen zwischen der Vielzahl von Makromolekülen im Zytoplasma können zur Entstehung koexistierender Phasen führen, die durch Phasenseparation entstehen. Dieses Phänomen spielt eine entscheidende Rolle bei der räumlichen Organisation von Zellen und der Regulierung ihrer Funktionen. Viele der Moleküle, die für die Phasentrennung verantwortlich sind, können Übergänge zwischen verschiedenen Zuständen durchlaufen. Zum Beispiel können Proteine Konformationsübergänge vollziehen und zwischen verschiedenen Phosphorylierungszuständen wechseln. Darüber hinaus können sich Proteine, die für die Phasentrennung relevant sind, zu Oligomeren unterschiedlicher Größe zusammensetzen. Sowohl die molekularen Übergänge als auch die Oligomerisierung können als chemische Reaktionen im Rahmen von Theorien beschrieben werden, die die Phasentrennung in Multikomponentengemischen erklären. Diese Arbeit untersucht unter Verwendung von Methoden aus der Thermodynamik fern vom Gleichgewicht, wie mit Hilfe chemischer Reaktionen die Zusammensetzung und die Form koexistierender Phasen kontrolliert werden können. Wir konzentrieren uns auf molekulare Übergänge zwischen zwei Zuständen eines Moleküls, zum Beispiel eines Proteins, und finden einen diskontinuierlichen thermodynamischen Phasenübergang in der Zusammensetzung der proteindichten Phase in Abhängigkeit von der Temperatur. Des Weiteren kann das Brechen des detaillierten Gleichgewichts der molekularen Übergange durch die kontinuierliche Zugabe eines chemischen Moleküls, das analog wie ein Brennstoff fungiert, auch dazu verwendet werden, die Anzahl der verschiedenen koexistierenden Phasen und ihre Zusammensetzung zu regulieren. Darüber hinaus kann eine Veränderung der Konzentration des brennstoffähnlichen Moleküls zur Entstehung neuartiger Muster führen, wenn sich das System einem stationären Zustand fern vom Gleichgewicht nähert. Hier konzentrieren wir uns auf einen Mechanismus, der zur Bildung ringförmiger Muster führt. Dies ist motiviert durch die Beobachtung ähnlicher Formen in Experimenten mit chemischen Reaktionszyklen, die mit einem Reservoir in dem brennstoffähnlichen Molekülen angereichert sind, gekoppelt sind. Wir schlagen vor, dass die Zusammensetzung im Zentrum der dichten Phase durch chemische Reaktionen verändert werden kann, was zu einer Instabilität führt, die die Bildung einer neuen Grenzfläche bewirkt. Wir bezeichnen diesen Zustand, der nur stabil ist, wenn das System fern vom Gleichgewicht gehalten wird, als Vakuole.

Die Kontrolle der Zusammensetzung koexistierender Phasen wird entscheidend, wenn die Anzahl der Komponenten und die Anzahl der zwischen diesen ablaufenden Reaktionen steigt. Dies ist der Fall bei Mischungen, die Proteine enthalten, die in einem Zustand als einzelne Monomere vorliegen können, aber auch Aggregate beliebiger Größe bilden können. Wir charakterisieren das Gleichgewicht solcher Systeme im Grenzfall der unendlich großen maximalen Aggregatsgröße. Für Systeme mit Phasentrennung zeigen wir, dass die Größenverteilung der Aggregate in jeder der koexistierenden Phasen unterschiedlich sein kann und von der Temperatur und der Energie der Bindungen zwischen den Monomeren bestimmt wird.

Mischungen, die aus scheibenförmigen oder kugelförmigen Aggregaten bestehen, können einen Gelierungsübergang durchlaufen. Die Gelierung kann als Sonderfall der Phasenkoexistenz zwischen einer verdünnten Phase (dem "Sol"), die Aggregate endlicher Größe enthält, und einer "Gel"-Phase betrachtet werden, die in der Thermodynamik einem Aggregat unendlicher Größe entspricht. Eine Senkung der Temperatur führt zu einem Übergang von zwei koexistierenden "Sol"-Phasen zur Koexistenz einer "Sol"- und einer "Gel"-Phase. Zusammenfassend lässt sich sagen, dass diese Arbeit einen theoretischen Rahmen für die Untersuchung von phasentrennenden Systemen bietet, die aus vielen Komponenten bestehen, die chemischen Reaktionen unterliegen. Darüber hinaus wird erörtert, wie solche Reaktionen genutzt werden können, um die Zusammensetzung der koexistierenden Phasen zu steuern.

Contents

1 **Introduction: phase separation in complex mixtures** **1**

2 **Thermodynamics of mixtures with many reacting components** **4**
  2.1 The interplay between phase equilibrium and chemical equilibrium . . 5
    2.1.1 Helmholtz free energy for many interacting components 5
    2.1.2 Phase equilibrium 6
    2.1.3 Chemical equilibrium 9
    2.1.4 Thermodynamic equilibrium 12
  2.2 Relaxation kinetics of multicomponent mixtures in the presence of chemical reactions 15
    2.2.1 Detailed balance of the rates and relaxation to chemical equilibrium in homogeneous system 16
    2.2.2 Chemical kinetics with compartments at phase equilibrium . . 17
    2.2.3 Kinetics of coexisting phases in the presence of chemical reactions 19

3 **Controlling phase composition via molecular transitions** **21**
  3.1 Molecular transitions at equilibrium 22
    3.1.1 Reentrant phase behaviour 23
    3.1.2 Temperature induced first-order transition in phase composition 26
  3.2 Phase separation kinetics with molecular transitions maintained away from equilibrium via fuel 27
    3.2.1 Control of the number of coexisting phases via fuel 29
    3.2.2 Active switch of condensate composition 32

4 **Controlling the shape of coexisting phases via molecular transitions** **34**
  4.1 Fuel controls the shape of coexisting phases 35
  4.2 Fuel-driven chemical reactions lead to vacuole formation 37
    4.2.1 The effective droplet model 37
    4.2.2 Spinodal instability at the centre of chemically active droplets . 40
    4.2.3 Describing vacuoles within the effective droplet model 44
  4.3 Theory of active vacuole compared with experiments using chemically-active coacervates 49
    4.3.1 Experimental system using active coacervates 49

4.3.2 Phase diagram for coacervates 50
4.3.3 Vacuole formation in coacervate systems coupled to a fuel reservoir 53
4.3.4 Recapitulating experimental findings with the effective droplet model 53

5 Controlling phase composition in the limit of a large number of components 57
5.1 Equilibrium theory of aggregation and phase separation 58
5.1.1 A chemical reaction network to describe aggregation 58
5.1.2 Scaling laws in the multicomponent aggregation free energy . . 59
5.1.3 Chemical equilibrium in homogeneous systems 60
5.1.4 Phase and thermodynamic equilibrium 62
5.1.5 The interplay between phase separation and aggregation equilibrium 65
5.1.6 Gelation transition in the limit of infinitely large aggregates . . 68
5.2 Aggregation kinetics at phase equilibrium 70

6 Conclusion and future perspectives 74

A Phase equilibrium in multicomponent mixtures 77

B Derivation of equilibrium fuel profile 79

C One-dimensional aggregates infinite size 81

D Gelation transition for two and three-dimensional aggregates 83

Bibliography 84

Chapter 1

Introduction: phase separation in complex mixtures

In 2005, the American writer David Foster Wallace gave a commencement speech to the graduating class at Kenyon College. His speech began with the following story:

There are these two young fish swimming along and they happen to meet an older fish swimming the other way, who nods at them and says "Morning, boys. How's the water?" And the two young fish swim on for a bit, and then eventually one of them looks over at the other and goes "What the hell is water?" [1]

I personally think that, with this anecdote, Wallace wanted to emphasise how, sometimes, things we know the least about are the very things we are immersed in. The Italian author Laura Tripaldi, in her recent book 'Parallel Minds', expresses this concept crystal clearly: "It is probable" she says "indeed it is almost certain, that common women or men can describe Schrödinger's cat paradox better than the chemical structure of the polyester in their socks" [2]. Let us consider water, which I think is the perfect example of something we give for granted. We are very familiar with this element, which constitutes more than half of our bodies. Water has always been part of our everyday lives, our body and our planet are full of it. In Italy, we tend to consider water boring to the extent that we use the saying "hai scoperto l'acqua calda" (literally "you discovered warm water") when someone has just discovered something that most people already knew.

But the truth is that there is still so much to be understood about water and its bizarre behaviour, which has earned water the title of "the most anomalous liquid". Indeed there are many scientists all around the world who everyday work very hard trying to answer Wallace's question: "What the hell is water?". Arguably, most of the enthusiasm about this fluid comes from the extraordinary properties of its phases, which made the emergence of life on earth possible [3]), and the transitions between them. The existence of two different kinds of liquid water, for example, has only recently been experimentally characterised [4].

The phase transition that excites me the most, however, manifests when water is mixed with other liquids. When we pour alcohol into the water, for example, we obtain a homogeneous mixture. This is because molecules in the liquid state can quickly rearrange, and the entropy in the mixed state is higher than the corresponding value in the demixed state. We are used to well-mixed aqueous solutions, but this is not the only option. Pouring oil in water, for example, leads to the coexistence of oil-rich droplets surrounded by a water-rich phase. This is caused by interactions among molecules. Specifically, in this case, the energy in the phase-separated state is much lower than the energy corresponding to the homogeneous state, and this difference outcompetes the entropic gain in mixing molecules. In the next chapter, I will discuss the key factors that have generated so much interest in the phase separation phenomenon in the last several years.

Phase separation in living cells and at the origin of life

The cytoplasm is an aqueous fluid filling the cell that is composed of a multitude of macromolecules such as proteins, lipids, and nucleic acids. As a consequence of thermal motion, these components continuously float around. A crude estimate [5] reveals that it takes roughly 0.01 s for a protein to travel across an E. Coli cell, which has a diameter in the order of 1μm. For this reason, the formation of compartments to organise the interior of cells is of crucial importance. These compartments, called organelles, were traditionally thought to be surrounded by selectively permeable membranes. In typical textbook pictures, cells look dominated by all sorts of barriers and rigid structures. In 2009, however, Clifford Brangwynne and a team formed, among the others, by Frank Jülicher and Anthony Hyman, saw evidence that P granules in C elegant embryos behave like liquid drops [6]. Indeed these organelles were observed to fuse, shear, and wet the nucleus. This experiment paved the way for the discovery of many other membrane-less organelles with different material properties (such as viscosity or surface tension) that, besides membrane-bound organelles, inhabit the cell [7, 8]. In addition, liquid-like phases enriched in certain macromolecules, sometimes referred to as “biomolecular condensates”, are thought to play a major role in many biological functions [9] and dysfunctions [10, 11].

Another liquid mixture that has been the focus of a lot of recent research is the prebiotic soup. According to the prebiotic soup hypothesis, simple organic compounds accumulated in aqueous solutions on the surface of prebiotic earth and then combined into complex organic molecules, such as nucleic acids, which are the building blocks of life. For this reason, a lot of effort has been made to study mixtures in pre-biotic plausible conditions and characterise their properties, such as their phase behaviour. In particular, recent studies have shown that oligonucleotides phase separate forming coacervates [12, 13], liquid crystals [14, 15] or hydrogels [16, 17], which can lead to a local enrichment of specific oligonucleotides. The idea that the emergence of phase separation in pre-biotic mixtures could have played a role in facilitating one or more key steps in the origin of life (for example local enrichment and selection of nucleotides [18] or protocell division [19, 20]) is currently under debate, and many theoretical and experimental work is likely to be done in the next years in this direction.

Chapter 2

Thermodynamics of mixtures with many reacting components

In the previous chapter, we have come to appreciate the raising importance of phase separation in different research fields, ranging from cell biology to the origin of life. Unfortunately, for reasons that will be discussed in this chapter, modelling the phase behaviour of mixtures composed of many components remains a challenging task. Much work has still to be done in refining the existing methods [21, 22, 23, 24] to achieve this goal. Here we provide an overview of a specific approach, namely the mean-field theory of multi-component mixtures, that we will adopt throughout the thesis to study complex mixtures composed of many components. We will show that introducing chemical reactions among these components and imposing chemical equilibrium reduces the number of relevant degrees of freedom at thermodynamic equilibrium. This reduction can become crucial in treating systems with a large number of components.

In the first section, we will focus on how to characterise the thermodynamic equilibrium of multicomponent mixtures in the presence of chemical reactions. In the second part, we will review different methods to study the passive relaxation kinetics that leads to the equilibrium state.

2.1 The interplay between phase equilibrium and chemical equilibrium

2.1.1 Helmholtz free energy for many interacting components

In this section, we describe the thermodynamic behaviour of a system composed of $M+1$ interacting components. We describe the mixture in the T-V-N_i-ensemble, N_i being the particle number of component $i = 0, \ldots, M$. The system volume reads

$$V = \sum_{i=0}^{M} N_i v_i \,, \tag{2.1}$$

where we have introduced the molecular volumes v_i. We proceed by introducing the volume fractions of each component $\phi_i = N_i v_i / V$. The thermodynamic behaviour of the system is encoded in the Helmholtz free energy

$$F\left(T, V, \{N_i\}\right) = \int \mathrm{d}V \left[f\left(T, V, \{\phi_i\}\right) + \sum_{i,j=0}^{M} \frac{\kappa_{ij}}{2} \nabla\phi_i \nabla\phi_j \right] . \tag{2.2}$$

In this work, we consider the Flory-Huggins free energy density, defined as [25, 26]

$$f = \frac{k_B T}{v_0} \left[\sum_{i=0}^{M} \frac{\phi_i}{\nu_i} \ln\left(\frac{\phi_i}{\nu_i}\right) + \frac{\omega_i}{k_B T}\phi_i + \sum_{i,j=0}^{M} \frac{\chi_{ij}}{2 k_B T}\, \phi_i \phi_j \right] , \tag{2.3}$$

where we made use of the volume ratios $\nu_i = v_i / v_0$. The first term represents the mixing entropy, which favours homogeneous solutions. ω_i is the internal free energy per monomer of the i-th solute component accounting for internal bonds and configurational rearrangements in the creation of a unit of component i [1]. In the last term, the off-diagonal, symmetric matrix χ_{ij} captures interactions among components [27]. If the molecular volumes change only slightly upon variations of the control parameters, we can exploit a further assumption, namely that v_i are independent of system volume, temperature, and composition [28]. This assumption defines *incompressible* systems for which, as is clear from Eq. (2.1), not all N_i and V can vary independently [29]. For example, one could adopt N_i with $i = 0, \ldots, M$ as independent state variables, with V given by Eq. (2.1). We adopt an alternative description

---

[1] To better understand the physical meaning of internal free energies we can consider homogeneous states $\tilde{\phi}$ composed entirely of the i-th component, defined by $\tilde{\phi}_j = \delta_{ij}$, where δ_{ij} is the Kronecker delta. We get the relation

$$\omega_i = \frac{F(\tilde{\phi})}{N_i \nu_i} - k_B T \nu_i^{-1} \ln \nu_i^{-1} \,.$$

Thus we identify ω_i as the free energy needed to "construct" a single monomer of the i-th component, subtracting the conformational entropy coming from having more states if the i-th species has a different size than the others in terms of V and ϕ_i with $i = 1, \dots, M$, and ϕ_0 given by Eq. (2.1), rewritten as

$$\phi_0 = 1 - \phi_{\text{tot}} \,, \qquad \phi_{\text{tot}} = \sum_{i=1}^{M} \phi_i \,. \tag{2.4}$$

We denote the 0-th component as the solvent and the components $i = 1, \dots, M$ as solutes. Without loss of generality, we set $k_{i0} = 0$ for $i = 0, \dots, M$. We introduce the exchange chemical potentials of the i-th solute component,

$$\bar{\mu}_i = v_i \frac{\delta}{\delta \phi_i} F\left(\phi_1, \dots \phi_M\right) \,. \tag{2.5}$$

Making use of Eq. (2.2) and Eq. (2.3) we get an expression for the exchange chemical potential of the form

$$\begin{aligned}\bar{\mu}_i = k_B T \left(\ln \phi_i + 1\right) + \nu_i \Bigg[& - k_B T \left(\ln \phi_{\mathrm{s}} + 1\right) + \omega_i - \omega_0 \\ & + \sum_{j=0}^{M} \left(\chi_{ij} - \chi_{0j}\right) \phi_j - \kappa_{ij} \nabla \phi_j^2 \Bigg] \,,\end{aligned} \tag{2.6}$$

where in the first line we made use of Eq. (2.4) to eliminate the dependency on ϕ_0. We also introduce the osmotic pressure

$$\Pi = -\frac{\partial F}{\partial V} = -f\left(\phi_1, \dots \phi_M\right) + \sum_{i=1}^{M} \bar{\mu}_i \frac{\phi_i}{v_i} \,. \tag{2.7}$$

Since the derivative with respect to volume in the equation above is meant to be performed keeping the number of solute molecules $N_1, \dots, N_M$ constant, the osmotic pressure quantifies responses to volume variations coming from changes in the solvent amount. Its physical meaning becomes clear placing the system in contact with a solvent reservoir through a semi-permeable membrane: the osmotic pressure quantifies the pressure exerted on the membrane by the mixture. The osmotic pressure in Eq. (2.7), together with the exchange chemical potential, will be used in the next section to study the phase behavior of the mixture.

2.1.2 Phase equilibrium

Due to the presence of interaction terms (χ_{ij} in Eq. (2.3)), for a fixed temperature T the equilibrium state of the system can consist of n_{p} phases, i.e. homogeneous subdomains with specific values of the volume fractions ϕ_i. We now focus on locating the points in the phase space $(\{\phi_i^\alpha\}, T)$ associated with each phase $\alpha = \mathrm{I}, \dots, n_{\mathrm{p}}$. This corresponds to determining the phase behavior of the system described by the free energy

$$F = \sum_{\alpha=\mathrm{I}}^{n_{\mathrm{p}}} f\big(\{\phi_i^\alpha\}\big) V^\alpha \,, \qquad \alpha = \mathrm{I}, \dots, n_{\mathrm{p}} \,, \tag{2.8}$$

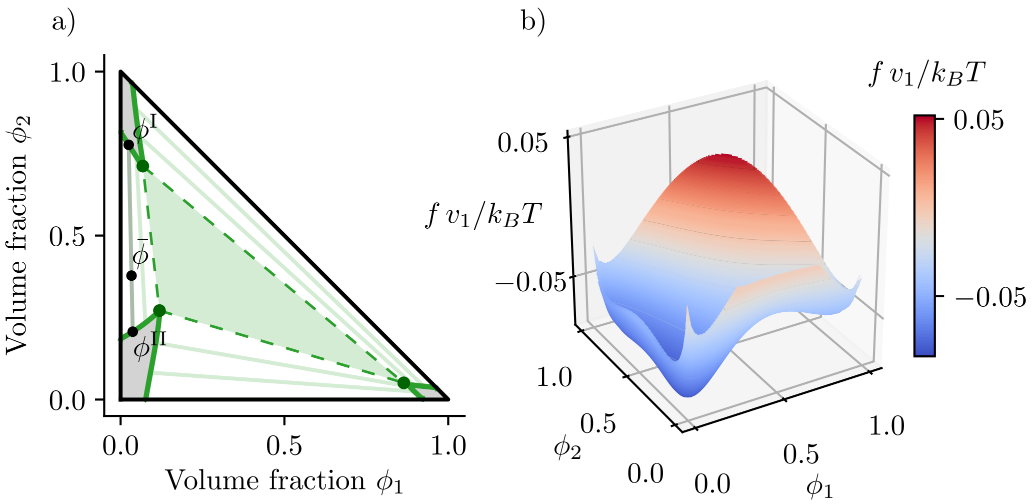

FIGURE 2.1: **Phase equilibrium in ternary mixture** a) The solutions of Eqs. (2.9) divide the $\phi_1 - \phi_2$ domain in three distinct regions. The grey area corresponds to a homogeneous mixture, while the green striped area to two-phase coexistence. In particular, in green, we depict the tie lines which connect the average system volume fraction with the two coexisting phases. The triangle shaded in green corresponds to three-phase coexistence, with the dark green dots representing the volume fractions in the three phases. In b) we plot the free energy density that leads to the phase behavior discussed in a). Here, $\chi_{01}/k_BT = 1.5$, $\chi_{02}/k_BT = 1.25$, $\chi_{12}/k_BT = 1$, $\nu_1 = \nu_2 = 1$.

where we have introduced the phase volumes V^α. Minimising F with the constraints $V = \sum_{\alpha=\mathrm{I}}^{n_\mathrm{p}} V^\alpha$ and $\bar{\phi}_i V = \sum_{\alpha=\mathrm{I}}^{n_\mathrm{p}} \phi_i^\alpha V^\alpha$ results in the following conditions, see App. A

$$\bar{\mu}_i\big(\{\phi_j^{\mathrm{I}}\}\big) = \bar{\mu}_i\big(\{\phi_j^{\alpha}\}\big)\,, \tag{2.9a}$$

$$\Pi\big(\{\phi_i^{\mathrm{I}}\}\big) = \Pi\big(\{\phi_i^{\alpha}\}\big)\,, \tag{2.9b}$$

where the index α runs over all phases different from I, i.e. $\alpha = \mathrm{II}, \ldots, n_\mathrm{p}$, and $i, j = 1, \ldots, M$. The conditions in Eqs. (2.9) constrain the dimension of the manifold on which vectors ϕ_i^α lie. In particular, we count $(Mn_\mathrm{p} + 1)$ degrees of freedom (n_p volume fraction vectors of M components each, plus the temperature). To establish equilibrium between n_p phases, we have to impose the $(M+1)$ equalities in Eqs. (2.9) (M exchange chemical potential plus the osmotic pressure) between $n_\mathrm{p} - 1$ couple of phases. Thus, the number of truly independent intensive degrees of freedom n_d is given by

$$n_\mathrm{d} = Mn_\mathrm{p} + 1 - (M+1)(n_\mathrm{p} - 1) = M + 2 - n_\mathrm{p}\,. \tag{2.10}$$

This equation is commonly known as the Gibbs phase rule for incompressible mixtures [30, 31]. It implies that each point in the (T, ϕ_i^α) phase representing one of the n_p coexisting phases is constrained to lie on a n_d-dimensional manifold, called the n_p phase boundary. We notice that the dimension of this manifold decreases increasing the number of coexisting phases n_p. In fact, the Gibbs rule sets an upper bound on the number of coexisting phases, $n_\mathrm{p}^* = M + 2$, for which the phase manifold reduces to n_p^* points in the phase diagram (with $n_\mathrm{d} = 0$). We stress that this is an upper bound, and the maximum number of phases that are effectively found in a phase diagram depends on the choice of the interaction matrix χ_{ij}.

As an example, we can examine ternary mixtures, where $M = 2$. Homogeneous states ($n_\mathrm{p} = 1$) lie on a three-dimensional manifold, in fact, each homogeneous state is determined by fixing the solutes volume fractions ϕ_1 and ϕ_2 and the temperature T. Couples of points, $n_\mathrm{p} = 2$ associated with two phases that coexist, lie on a two-dimensional manifold, often called the binodal. In fact, to locate each of such points it is sufficient to specify, for example, T and ϕ_1, with ϕ_2 being determined by the equilibrium condition. Three and four-phase coexistence ($n_\mathrm{p} = 3$ and $n_\mathrm{p}^* = 4$) span three lines ($n_\mathrm{d} = 1$) and four points ($n_\mathrm{p} = 0$), respectively. In Fig. 2.1a) we plot one slice of the ternary phase diagram corresponding to fixed temperature T.

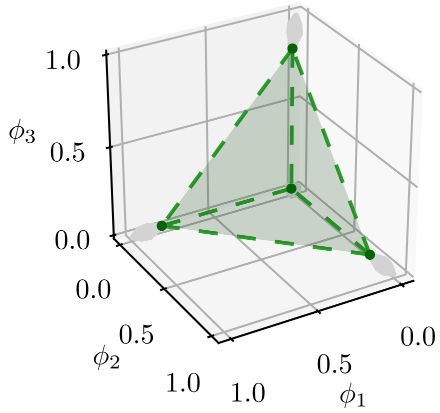

FIGURE 2.2: **Phase equilibrium in quaternary mixtures** We highlight in grey and green the area corresponding to a homogeneous mixture and four-phase coexistence, respectively. The dark green dots represent the volume fractions in the four phases. Here, $\chi_{ij}/k_B T = 3.5$ and $\nu_i = 1$ for $i \neq j = 0, 1, 2, 3$.

Here homogeneous states lie on two-dimensional manifolds (grey areas), while each binodal branch is a curve (dark green). Tie lines (in light green) connect pairs of coexisting phases. For T fixed, three phases are unique points, dark green dots in 2.1a). Four-phase coexistence is not compatible with the set of interaction parameters chosen. In Fig. 2.1 b) we plot the free energy density profile that led to such phase behavior. In Fig. 2.2 a) we illustrate a constant T slice of the phase diagram of a quaternary mixture ($M = 3$), where green dots represent the composition of 4 coexisting phases. In green, we highlight the region corresponding to four-phase coexistence. Once the different n_p phase boundaries, with $n_\mathrm{p} = 1, \ldots, n_\mathrm{p}^*$, are determined via Eqs. (2.9), it is possible to determine the volume V^α and composition ϕ_i^α of the n_p coexisting phases associated to any fixed temperature T, average composition

$$\bar{\phi}_i V = \sum_{\alpha=\mathrm{I}}^{n_\mathrm{p}} \phi_i^\alpha V^\alpha \,, \tag{2.11a}$$

and total volume

$$V = \sum_{\alpha=\mathrm{I}}^{n_\mathrm{p}} V^\alpha \,. \tag{2.11b}$$

In fact, the $n_\mathrm{d} = (M + 1 - n_\mathrm{p})$ degrees of freedom necessary to locate n_p points on the respective phase boundaries plus the n_p phase volume V^α add up to $M + 1$ parameters, that are uniquely determined by the $M + 1$ constraints in Eqs. (2.11). This is illustrated in Fig. 2.1 a), where we study the phase decomposition of a state with average volume fraction $\bar{\phi}$. This choice of the average uniquely identifies a tie line (shaded in gray) connecting a pair of points ϕ^I and ϕ^II (black points) and fixes the phase volumes V^I and V^II, which are given by

$$V^\mathrm{I} = \frac{\bar{\phi}_i - \phi_i^\mathrm{II}}{\phi_i^\mathrm{I} - \phi_i^\mathrm{II}}, \qquad V^\mathrm{II} = \frac{\phi_i^\mathrm{I} - \bar{\phi}_i}{\phi_i^\mathrm{I} - \phi_i^\mathrm{II}}\,, \tag{2.12}$$

and have the geometrical interpretation of the distances $\|\bar{\phi} - \phi^\mathrm{II}\|$ and $\|\bar{\phi} - \phi^\mathrm{I}\|$, respectively, normalised by the length $\|\phi^\mathrm{I} - \phi^\mathrm{II}\|$.

In practice, solving Eqs. (2.9) to determine the parametric form of phase boundaries is a hard task. Instead, one typically specifies an average volume fraction $\bar{\phi}_i^\alpha$ and looks for the phase decomposition associated with that specific average composition only. This entails looking for n_p vectors ϕ_i^α, composed in total of $n_\mathrm{p}M$ volume fractions values, plus n_p phase volumes V^α. These are uniquely determined by the $M(n_\mathrm{p} - 1)$ equations in Eq. (2.9) plus the $M + 1$ constraints in Eqs. (2.11). Again see Fig. 2.1 a) for an illustration. To determine the phase equilibrium of the system we have to scrutinise solutions of Eqs. (2.9) corresponding to different numbers of phases $n_\mathrm{p} = 1, \ldots M + 2$, and determine the one with the lower total free energy, defined in Eq. (2.8). Finally, we note that solving for the phase volume fractions is equivalent to constructing the convex hull of the free energy density. In fact, recalling the definitions in Eqs. (2.5) and (2.7), the set of equations in Eqs. (2.9) can be geometrically interpreted as finding an $(n_\mathrm{p} - 1)$-dimensional hyperplane tangent to f at each point ϕ^α. For example, for $n_\mathrm{p} = 2$, Eqs. (2.9) are equivalent to the common tangent construction [32].

2.1.3 Chemical equilibrium

The framework presented in this section follows closely the presentation in [33] and references therein. We now introduce a set of R chemical reactions

$$\sum_{i=1}^{M} \sigma_{ia}^{+} C_i \rightleftharpoons \sum_{i=1}^{M} \sigma_{ia}^{-} C_i \,, \qquad a = 1, \ldots R\,, \tag{2.13}$$

where C_i indicate the i-th component and $\sigma_{ia}^{\pm}$ are stoichiometric coefficients. Notice that the index i runs from 1 to M only since we focus on chemical reactions that do not involve the solvent ($i = 0$). If the reaction a occurs from left to right once, σ_{ia}^{+}

and σ^-_{ia} represent the amount of component i-th that has reacted and is produced, respectively. They combine to form the stoichiometric matrix and the volume stoichiometric matrix, defined, respectively, as

$$\sigma_{ia} = \sigma^+_{ia} - \sigma^-_{ia}\,, \qquad \tilde{\sigma}_{ia} = \sigma_{ia}\nu_i\,. \tag{2.14}$$

Since we made the incompressibility assumption (constant v_i) and have chosen an ensemble with V fixed, for consistency, we restrict to reaction networks that conserve the sum of molecular volumes, namely

$$\sum_{i=1}^{M} \sigma_{ia} v_i = 0\,, \qquad \forall\, a = 1, \dots R\,. \tag{2.15}$$

Assuming that the reaction network leads to linearly independent columns of σ_{ia}, the stoichiometric matrix can be used to determine the $(M - R)$ conserved quantities associated with the chemical reaction network. This is done with the aid of Q_{ij}, defined via

$$\sum_{j=1}^{M} Q_{ij}\sigma_{ja}\nu_j = 0\,. \tag{2.16}$$

In other words, Q is a $(M - R) \times R$ matrix whose rows are the basis of the null space of $\sigma_{aj}v_j$. The $(M - R)$ conserved quantities then read

$$\psi_i = \sum_{j=1}^{M} Q_{ij}\phi_j\,. \tag{2.17}$$

These represent a set of quantities that are not affected by chemical reactions, as we will prove in the following. Since the basis for the null space of $\sigma_{aj}v_j$ is not unique, the choice of conserved quantities is also not unique. For volume-conserving reactions, the stoichiometric matrix is such that one row of Q (that we chose to be the first) is a constant vector: $Q_{0i} = 1$. In fact, the null space equation, Eq. (2.16) for for $Q_{0i} = 1$ reduces to the constraint in Eq. (2.15). The corresponding conserved quantity is ϕ_{tot}, defined in Eq. (2.4). We can also introduce the R reaction extents, defined as

$$\xi_\alpha = \sum_{i=1}^{M} E_{aj}\phi_i\,. \tag{2.18}$$

With the aid of the matrix E, the pseudo inverse of the volume stoichiometric matrix $\sigma_{ia}v_i$, defined through $\sum_i E_{ai}\sigma_{ib}\nu_i = \delta_{ab}$. As for Q, the matrix E is not unique. We can now combine Q and E into a square matrix

$$U = \left(\begin{array}{c} Q \\ \hline E \end{array} \right) . \tag{2.19}$$

Its inverse is simply

$$U^{-1} = \left(\begin{array}{c|c} Q^{-1} & \tilde{\sigma} \end{array} \right) , \tag{2.20}$$

were $\tilde{\sigma}$ is the volume stoichiometric matrix defined in Eq. (2.14), and Q^{-1} is the pseudo inverse of Q. In fact, by making use of the definitions of Q and E, one can easily show that

$$U\,U^{-1} = \left(\begin{array}{c|c} I & 0 \\ \hline 0 & I \end{array} \right) . \tag{2.21}$$

These definitions allow to establish a mapping between ϕ_i and (ψ_i, ξ_a) via

$$\phi_i = U^{-1}\phi = \sum_{i=1}^{M-R} Q^{-1}_{ij}\psi_i + \sum_{a=1}^{R} \sigma_{ia} v_i \xi_a \,. \tag{2.22}$$

To get familiar with these definitions we now discuss one example that will be useful in the following chapters.

Single reaction $A \rightleftharpoons B$ Here we discuss the case of a ternary mixture composed of three components: C_0, the solvent, $C_1 = A$ $C_2 = B$, with $v_A = v_B = v$, and $v/v_0 = \nu$. We allow the reaction ($a = 1$) $A \rightleftharpoons B$. The stochiometric and volume stoichiometric matrices read

$$\sigma = \begin{array}{cc} a=1 & \\ \begin{pmatrix} +1 \\ -1 \end{pmatrix} & \begin{array}{c} A \\ B \end{array} \end{array} , \qquad \tilde{\sigma} = \begin{array}{cc} a=1 & \\ \begin{pmatrix} +v \\ -v \end{pmatrix} & \begin{array}{c} A \\ B \end{array} \end{array} . \tag{2.23}$$

We can introduce the vector Q imposing $Q_i\tilde{\sigma}_i = 0$, leading to $Q_1 = Q_2$. As previously outlined, this condition leads to the constant vector, which is always a basis (in this case the only one), of the null space of $\tilde{\sigma}$. In conclusion, we get:

$$Q = \begin{pmatrix} 1 & 1 \end{pmatrix} , \qquad \psi = \phi_{\text{tot}} = \phi_A + \phi_B \,. \tag{2.24}$$

We now introduce E to be the pseudo-inverse of $\tilde{\sigma}$, namely $E_i v_i \sigma_i = 1$, resulting in the constraint $-E_1 + E_2 = 1/v$. We choose $B_1 = 0$ and get

$$E = \begin{pmatrix} 0 & v^{-1} \end{pmatrix}, \qquad \xi = \phi_B/\nu\,. \tag{2.25}$$

To discuss chemical equilibrium, we introduce the so-called forward (+) and backward (−) reaction free energies

$$\Delta\mu_a^{\pm} = \sum_{i=1}^{M} \sigma_{ia}^{\pm}\bar{\mu}_i\,, \tag{2.26}$$

and the net reaction free energy

$$\Delta\mu_a = \sum_{i=1}^{M} \sigma_{ia}\bar{\mu}_i\,. \tag{2.27}$$

Chemical equilibrium is then enforced via

$$\Delta\mu_a = 0\,, \qquad a = 1\ldots, R\,. \tag{2.28}$$

We can now exploit the decomposition in Eq. (2.22) to express $\bar{\mu}_i$ as a function of $(\{\psi_i\},\{\xi_a\})$. The set of R equations in (2.28), allows us to find the reaction extents as a function of the conserved quantities $\xi_a = \xi_a(\{\psi_i\})$. In conclusion, chemical equilibrium reduces the number of independent volume fractions to $M-R$, which we identify with the conserved quantities ψ_i, see Eq. (2.17). In the presence of chemical reactions, ψ_i are the only quantities that can be controlled experimentally since they do not change as the reaction progresses. Thus, they are the only proper variables that should be used to describe systems at chemical equilibrium. Once specified the value of ψ_i, the system is completely determined and the dependent variables ξ_a, defined in Eq. (2.18), can be determined via chemical equilibrium, Eq. (2.28), exploiting Eq. (2.22).

2.1.4 Thermodynamic equilibrium

In a mixture composed of M components in the presence of R chemical reactions, the global equilibrium of the system is reached once both chemical equilibrium and phase equilibrium are enforced. We first impose chemical equilibrium, exploiting the theory developed in the previous section. There we have discussed a change of variables $\{\phi_i\} \leftrightarrow (\{\psi_i\},\{\xi_a\})$, via the mapping in equation Eq. (2.22). The $(M-R)$-dimensional vector ψ contains the conserved quantities, see Eq. (2.17), which are the only independent degrees of freedom in systems at chemical equilibrium. The R-dimensional vector ξ contains the reaction extents, see Eq. (2.18), which at equilibrium are a function of ψ_i that can be determined solving the set of equations in (2.28) making use of Eq. (2.22).

Once the functions $\xi_a = \xi_a(\{\psi_i\})$ are determined this way, we can use it together with the change of variables in Eq. (2.22) to express the free energy density in Eq. (2.3)

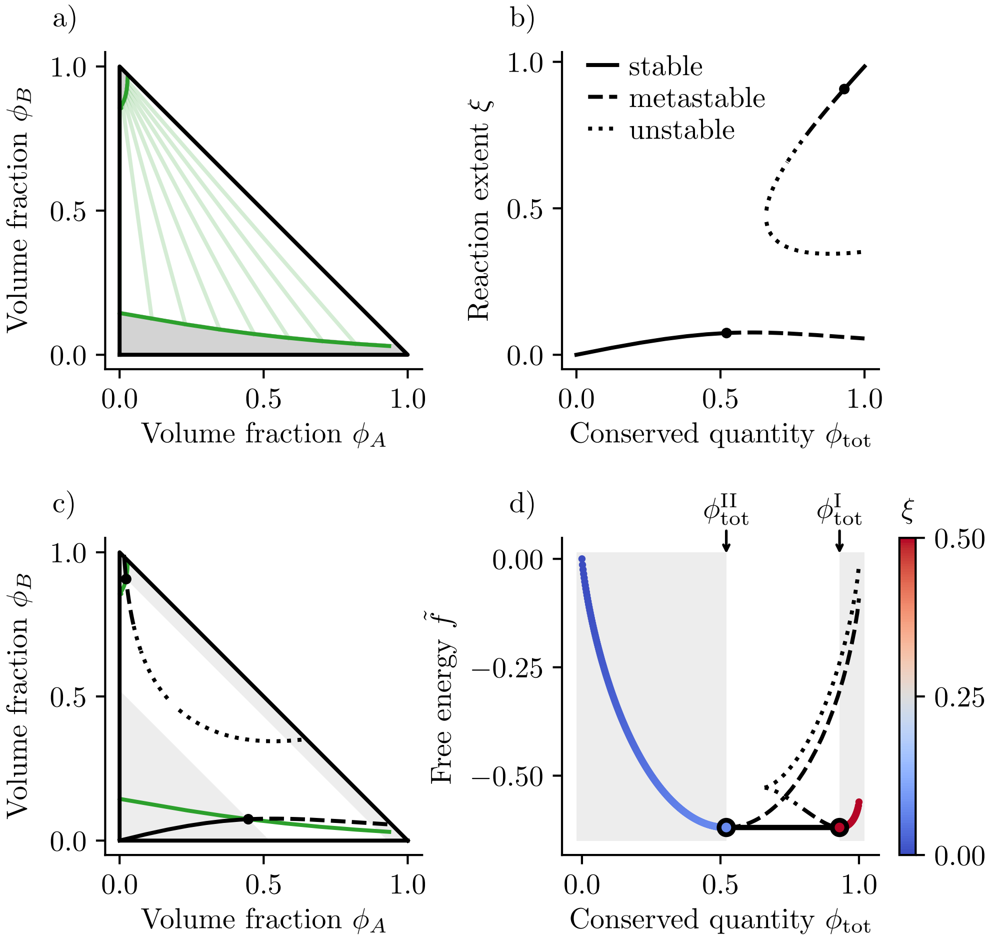

FIGURE 2.3: **Chemical, phase and thermodynamic equilibrium in the presence of the $A \rightleftharpoons B$ reaction** a) We study a ternary mixture that, at phase equilibrium, can remain homogeneous (grey area) or demix into two phases (striped area, with tie lines in light green). The boundaries between these two regions are called binodal lines (in dark green). b) The chemical equilibrium condition, Eq. (2.28), allows to find the chemical extent $\xi = \phi_B/\nu$ as a function of the conserved quantity ϕ_{tot}. Note that the presence of interactions makes multiple solutions possible. See panel d) for the stability analysis. c) Chemical equilibrium curve (in black) plotted in the $\phi_A - \phi_B$ plane. Its interceptions with the binodal (black dots) determine the values of ϕ_{tot} for which the system remains homogeneous (grey areas). Its boundaries, corresponding to $\phi_{\mathrm{tot}}^{\mathrm{I}}$ and $\phi_{\mathrm{tot}}^{\mathrm{II}}$, encompass the two-phase coexistence region, the black dots indicating the volume fractions in the two phases. d) Assuming chemical equilibrium, thermodynamic equilibrium can be studied as a function of the only relevant control parameter, the conserved quantity ϕ_{tot}. We plot the rescaled free energy $\tilde{f}$ (see Eq. (2.30)) and identify the branches where homogeneous states are stable (coloured lines), metastable (dashed lines), and unstable (dotted lines). Coexisting phases $\phi_{\mathrm{tot}}^{\mathrm{I/II}}$ and their respective free energies are represented by circled points, joined by the black solid line. The colour code indicates the value of the reaction extent ξ. Here $k_B T = 0.4\chi_{B0}$, $\chi_{A0} = 0.25\chi_{B0}$, $\chi_{AB} = 1.5\chi_{B0}$, $\omega_A = \omega_0 = 0$, $\omega_B = 0.2\chi_{B0}$, $\nu_A = \nu_B = 1$.

as a function of the conserved quantities only. We then impose phase equilibrium and repeat the convex hull construction described in Sec 2.1.2 with $f = f(\{\psi_i\})$ in the space $(\{\psi_i\}, T)$. Explicitly, phase equilibrium conditions for systems at chemical equilibrium read

$$\bar{\mu}_i\big(\{\psi_i^\alpha\}\big) = \bar{\mu}_i\big(\{\psi_i^\beta\}\big)\,, \tag{2.29a}$$

$$\Pi\big(\{\psi_i^\alpha\}\big) = \Pi\big(\{\psi_i^\beta\}\big)\,. \tag{2.29b}$$

Once the value of the conserved quantities in each phase is determined, we can make use of the relation $\xi_a = \xi_a(\{\psi_i\})$ to completely characterise the mixture. This construction is illustrated in Fig. 2.3 for the chemical reaction $A \rightleftharpoons B$ introduced in paragraph 2.1.3. In Fig. 2.3 a) we illustrate the ternary mixture phase equilibrium, with tie lines and binodal highlighted in light and dark green, respectively. Fig. 2.3 b) depict the relation between the conserved quantity ϕ_{tot} and the reaction extent ξ, stemming from chemical equilibrium, Eq. (2.28). In Fig. 2.3 c) the same chemical equilibrium curve is plotted in the $\phi_A - \phi_B$ plane, along with the ternary phase diagram. Its interceptions with the phase boundary (black dots) determine the values of ϕ_{tot} for which the system remains homogeneous (grey areas). In the remaining region, the system phase separates, with phase volume fractions indicated by black dots. In Fig. 2.3 d) we switch to a representation in terms of the only relevant control parameter at chemical equilibrium, the conserved quantity ϕ_{tot}. For visualization purposes, we plot the rescaled free energy

$$\tilde{f} = \frac{v_0}{k_B T}\left(f - m\,\phi_{\text{tot}}\right)\,, \qquad m = \frac{f(\phi_{\text{tot}}^{\text{I}}) - f(\phi_{\text{tot}}^{\text{II}})}{\phi_{\text{tot}}^{\text{I}} - \phi_{\text{tot}}^{\text{II}}}\,. \tag{2.30}$$

Examining its curvature and its convex hull, we identify regions corresponding to homogeneous states (grey background), and phase separation (white background). We further distinguish between metastable (dashed lines), and unstable (dotted lines) branches, corresponding to positive and negative free energy curvature, respectively. Coexisting phases are represented by circled points, joined by a black solid line. The colour code indicates the reaction extent ξ which, together with ϕ_{tot}, completely determines the state of the system.

For systems with chemical reactions, the Gibbs must be generalised to account for the reduction of the independent components, caused by chemical equilibrium [34, 35]

$$n_{\text{d}} = (M - R) + 2 - n_{\text{p}}\,. \tag{2.31}$$

This imposes, for systems at chemical equilibrium, the maximum number of coexisting phases to be $n_{\text{p}}^* = M - R + 2$. Thus chemical equilibrium suppresses the dimension of the manifold where points corresponding to n_{p}-coexistence live, as illustrated in Fig. 2.4, and the maximum number of coexisting phases. In Fig. 2.4 a) we show that for this choice of parameters, below a certain temperature, the system without chemical reaction exhibits three-phase coexistence. The reaction $A \rightleftharpoons B$, however, leads to two-phase coexistence, except for fine-tuned values of the temperature. This has an interesting effect on the composition of the dense phase, as can be seen by fixing $\omega_A = 0$ and varying ω_B. Indeed, the dense phase is mainly composed of A for $\omega_B/\chi_{B0} = 0.15$ while for $\omega_B/\chi_{B0} = -0.05$ is dominated by B. In Fig. 2.4. In Fig. 2.4 b) and c) we show the free energy densities as a function of ϕ_{tot}, corresponding to the same two internal free energies ω_B chosen in a). Here this effect manifests in a strong difference between the reaction extents ξ, captured by the colour code, in the dense phases.

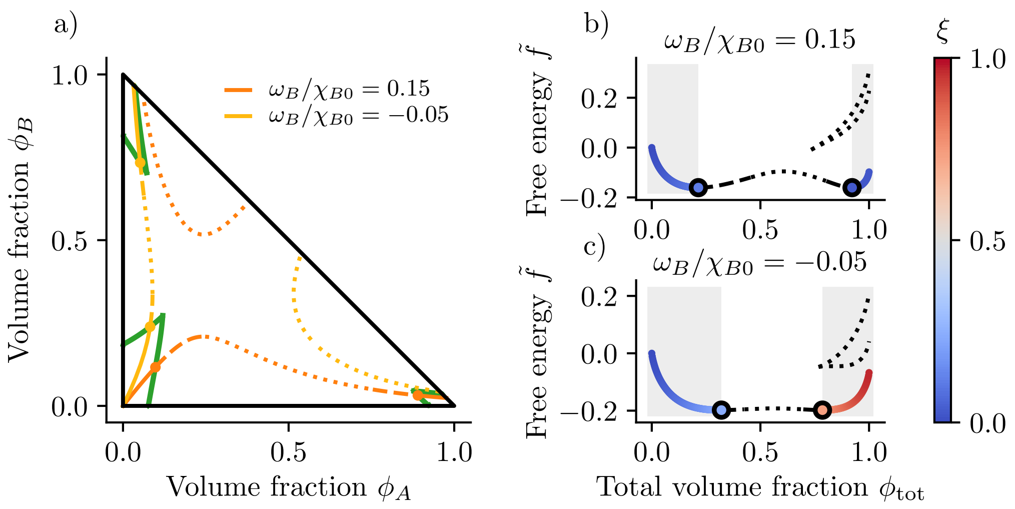

FIGURE 2.4: **Three-phase coexistence suppression leads to a sudden change of dense phase composition**. a) Chemical equilibrium lines corresponding to different internal free energy values, superimposed to the ternary phase diagram of Fig. 2.1, that allowed for three-phase coexistence. Chemical equilibrium leads to two-phase coexistence, phase volume fractions indicated by coloured dots. Fixing $\omega_A = 0$ but letting ω_B vary, the chemical equilibrium curve intercepts different branches of the binodal (in green), leading to a significant change in dense phase volume fractions. b) and c) free energy densities corresponding to $\omega_A = 0$ while $\omega_B/\chi_{B0} = 0.15$ and $\omega_B/\chi_{B0} = -0.05$, respectively. We identify the branches where homogeneous states are stable (coloured lines), metastable (dashed), and unstable (dotted). Coexisting phases are represented by circled points, while the colour code indicates the reaction extent ξ. The change of dense phase composition is highlighted by the difference in dense phase extent, namely low in a) and high b). Here, $k_BT = 0.425\chi_{B0}$, $\chi_{A0} = 1.25\chi_{B0}$, $\chi_{AB} = 1.5\chi_{B0}$, $\nu_A = \nu_B = 1$

2.2 Relaxation kinetics of multicomponent mixtures in the presence of chemical reactions

In the next chapters, we outline some methods to study the passive relaxation kinetics that leads to thermodynamic equilibrium. We will apply these approaches to different biochemically inspired examples, and discuss how to generalise such kinetic schemes to systems that cannot relax to equilibrium.

2.2.1 Detailed balance of the rates and relaxation to chemical equilibrium in homogeneous system

We start studying the kinetics of mixtures described in the previous sections, focusing on spatially homogeneous systems that relax to chemical equilibrium; see Ref. [36, 33]. We look for an equation of the form

$$\frac{\mathrm{d}\phi_i}{\mathrm{d}t} = r_i \, . \tag{2.32}$$

Since the source term originates from R chemical reactions, described by the stoichiometric matrix σ_{ia}, the chemical rates must be of the form

$$r_i = \sum_{a=1}^{M} v_i \sigma_{ia} r_a \, . \tag{2.33}$$

Recalling the definitions of conserved quantities and reaction extents, (Eq. (2.17) and Eq. (2.18), respectively) one obtains

$$\frac{\mathrm{d}\psi_i}{\mathrm{d}t} = 0 \, , \qquad \frac{\mathrm{d}\xi_a}{\mathrm{d}t} = r_a \, , \tag{2.34}$$

where we used the properties $\sum_j Q_{ij}\sigma_{ja}v_j = 0$ and $\sum_i E_{ai}\sigma_{ib}v_i = \delta_{ab}$. Now we can fully appreciate the importance of the conserved quantities ψ_i, which stay constant as the reaction proceeds, and the reaction extents ξ_a, which can be related to the cumulative amount of reaction a that occurred per unit volume. In Sec. 2.1.3, we introduced a change of variables (Eq. (2.22)) that allows to decompose ϕ_i in a constant part (the conserved quantities ψ_i) and a part that evolves in time (the reaction extents ξ_a) due to chemical reactions. We can write dynamic equations for the latter

$$\frac{\mathrm{d}\xi_a}{\mathrm{d}t} = r_a^+ - r_a^- \, , \tag{2.35}$$

with r_a^+ and r_a^- forward and backward reaction rates. The mixture evolves towards equilibrium if the rates obey detailed balance of the rates, namely

$$\frac{r_a^+}{r_a^-} = \exp\left(-\frac{\Delta\mu_a}{k_B T}\right) \, , \tag{2.36}$$

with $\Delta\mu_a$ defined in Eq. (2.27). For a discussion on the detailed balance of the rates see Appendix C in reference [32]. We chose

$$r_a^+ - r_a^- = \Lambda_a \left[1 - \exp\left(\frac{\Delta\mu_a}{k_B T}\right)\right] \, , \tag{2.37}$$

where we have introduced the kinetic coefficients Λ_a that must be positive and can depend on mixture composition. Recalling the decomposition in Eq. (2.22), the time evolution of the volume fractions reads

$$\frac{\mathrm{d}\phi_i}{\mathrm{d}t} = r_i \,, \qquad \text{for} \qquad i = 1 \dots M \,. \tag{2.38}$$

With the sources defined with the aid of $\Delta\mu_a$, see in Eq. (2.27)

$$r_i = \sum_{a=1}^{R} v_i \sigma_{ia} \left(r_a^+ - r_a^- \right) = \sum_{a=1}^{R} v_i \sigma_{ia} \Lambda_a \left[1 - \exp\left(\frac{\Delta\mu_a}{k_B T} \right) \right] . \tag{2.39}$$

2.2.2 Chemical kinetics with compartments at phase equilibrium

We now study the kinetics of multicomponent mixtures described in the previous sections, taking into account that interactions can lead to spatial inhomogeneities. We study passive systems and their relaxation kinetics towards the thermodynamic equilibrium, focusing on very slow chemical reactions and very fast diffusive kinetics. In this regime, the average system composition varies slowly so that at all times we can consider the system to be at phase equilibrium. By choosing initial average volume fractions corresponding to two-phase coexistence, we can consider the system volume to be divided into two homogeneous compartments as a result of phase separation. We then study the evolution of compartment sizes and volume fractions due to chemical reactions, enforcing instantaneous phase equilibrium at all times. The theoretical framework that we are about to review has been developed by Jonathan Bauermann and Sudarshana Laha in Ref. [37] and will be useful in the last chapter to study passive kinetics in the limit of a large number of components that can form molecular assemblies. To this aim, we start from the variation of particle numbers in compartments I and II

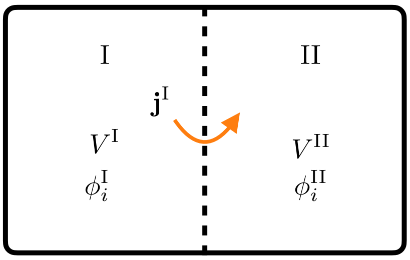

$$\frac{\mathrm{d}N_i{}^{\mathrm{I/II}}}{\mathrm{d}t} = -J_i^{\mathrm{I/II}} + R_i^{\mathrm{I/II}} \,, \tag{2.40}$$

where $R_i^{\mathrm{I/II}}$ are the variations due to chemical reactions while $J_i^{\mathrm{I/II}}$ due to particle hopping between the two phases. Particle conservation during crossing implies $J_i^{\mathrm{I}} = -J_i^{\mathrm{II}}$. The volumes in the two phases read

$$V^{\mathrm{I/II}} = \sum_{i=0}^{M} N_i^{\mathrm{I/II}} v_i \,. \tag{2.41}$$

Furthermore $V = V^{\mathrm{I}} + V^{\mathrm{II}}$. We now introduce volume fractions $\phi_i^{\mathrm{I/II}} = N_i^{\mathrm{I/II}} / V^{\mathrm{I/II}}$ and the rescaled rates $j_i^{\mathrm{I/II}} = v_i \, J_i^{\mathrm{i/II}} / V^{\mathrm{I/II}}$ and $r_i^{\mathrm{I/II}} = v_i \, R_i^{\mathrm{I/II}} / V^{\mathrm{I/II}}$ arriving to

$$\frac{\mathrm{d}\phi_i}{\mathrm{d}t}^{\mathrm{I/II}} = -j_i^{\mathrm{I/II}} + r_i^{\mathrm{I/II}} - \phi_i^{\mathrm{I/II}} \frac{\mathrm{d}\ln V}{\mathrm{d}t}^{\mathrm{I/II}} . \tag{2.42}$$

We derived a generalised version of Eq. (2.38), that accounts for the two-phase coexistence. Since we consider the two phases to be spatially homogeneous, an analogue derivation that led us to Eq. (2.39) allows us to set

$$r_0^{\mathrm{I/II}} = 0 , \tag{2.43}$$

$$r_i^{\mathrm{I/II}} = \sum_{a=1}^{R} v_i \sigma_{ia} \Lambda_a^{\mathrm{I}} \left[1 - \exp\left(\frac{\Delta\mu_a^{\mathrm{I/II}}}{k_B T} \right) \right] \qquad \text{for} \quad i = 1, \dots M . \tag{2.44}$$

where $r_0 = 0$ stems from the restriction to chemical reactions that do not involve the solvent and $\Delta\mu_a = \sum_{i=1}^{M} \sigma_{ia} \bar{\mu}_i$. Eq. (2.40) and Eq. (2.41) can be combined to get $\mathrm{d}_t V^{\mathrm{I/II}} = V^{\mathrm{I/II}} \sum_{i=0}^{M} (r_i^{\mathrm{I/II}} - j_i^{\mathrm{I/II}})$. Using the volume conserving properties of the rates $\sum_{i=0}^{M} r_i^{\mathrm{I/II}} = 0$, we finally get

$$\frac{\mathrm{d}\ln V}{\mathrm{d}t}^{\mathrm{I/II}} = -\sum_{i=0}^{M} j_i^{\mathrm{I/II}} . \tag{2.45}$$

Using conservation during particle hopping, expressed in terms of the rescaled currents $j_i^{\mathrm{i/II}}$

$$j_i^{\mathrm{I}} = -j_i^{\mathrm{II}} \frac{V^{\mathrm{II}}}{V^{\mathrm{I}}} , \tag{2.46}$$

is easy to check that the volume dynamics obeys $\mathrm{d}_t(V^{\mathrm{I}} + V^{\mathrm{II}}) = 0$. We then look for an expression for the currents $j_i^{\mathrm{I/II}}$. They must guarantee that phase equilibrium is satisfied at all times, which can be expressed by taking a time derivative of Eq.s (2.9)

$$\sum_{j=0}^{M} \frac{\partial \bar{\mu}_i^{\mathrm{I}}}{\partial \phi_j^{\mathrm{I}}} \frac{\mathrm{d}\phi_j^{\mathrm{I}}}{\mathrm{d}t} = \sum_{j=0}^{M} \frac{\partial \bar{\mu}_i^{\mathrm{II}}}{\partial \phi_j^{\mathrm{II}}} \frac{\mathrm{d}\phi_j^{\mathrm{II}}}{\mathrm{d}t} , \tag{2.47a}$$

$$\sum_{j=0}^{M} \frac{\partial \Pi^{\mathrm{I}}}{\partial \phi_j^{\mathrm{I}}} \frac{\mathrm{d}\phi_j^{\mathrm{I}}}{\mathrm{d}t} = \sum_{j=0}^{M} \frac{\partial \Pi^{\mathrm{II}}}{\partial \phi_j^{\mathrm{II}}} \frac{\mathrm{d}\phi_j^{\mathrm{II}}}{\mathrm{d}t} . \tag{2.47b}$$

Provided that the initial phase volume and volume fractions $V^{\mathrm{I}}(t = 0)$, and $\phi_i^{\mathrm{I/II}}(t = 0)$ are a solution of Eqs. (2.9). Once an expression for $\partial\bar{\mu}_i/\partial\phi_j$ and $\partial\Pi/\partial\phi_j$ is calculated, we can derive an a set of $M + 1$ equations for j_i^{I} inserting Eq. (2.42), Eq. (2.45), and Eq. (2.46) in Eqs. (2.47). These equations are linear and enable us to find an expression for $j_i^{\mathrm{I/II}}$ as a function of $\phi_i^{\mathrm{I/II}}$ and V^{I}/V. We have finally all the ingredients to characterise the dynamics of the phase volume and volume fractions $\phi_i^{\mathrm{I/II}}(t)$ and

$V^{\mathrm{I}}(t)$, integrating Eq. (2.42) and (2.45) and provided we can solve the initial phase equilibrium problem to find $V^{\mathrm{I}}(t=0)/V$, and $\phi_i^{\mathrm{I/II}}(t=0)$.

2.2.3 Kinetics of coexisting phases in the presence of chemical reactions

We now move to the general case of spatially heterogeneous systems, in which we can define a volume fraction field ϕ_i that varies in space within the system volume that obeys the conservation law

$$\frac{\partial \phi_i}{\partial t} = -\nabla \cdot \mathbf{j}_i + r_i \, . \tag{2.48}$$

The Onsager theory allows us to identify [38]

$$\mathbf{j}_i = -v_i \sum_{j=1}^{M} \Lambda_{ij} \nabla \bar{\mu}_j \, , \tag{2.49a}$$

$$r_i = -\sum_{a=1}^{R} v_i \sigma_{ia} \Lambda_a \, \Delta\mu_a \, , \tag{2.49b}$$

where $\Delta\mu_a$ is the reaction free energy defined in Eq. (2.27). Λ_{ij} are kinetic coefficients, that must be chosen positive and such to balance the divergences coming from the logarithmic terms in $\bar{\mu}$ in the dilute limit $\phi_i \to 0$, see Eq (2.5). A possibility is to chose Λ_{ij} diagonal, in the form [39]

$$\Lambda_{ij} = \Lambda \phi_i \phi_0 \, \delta_{ij} \, , \tag{2.50}$$

Another possible choice is [33]

$$\Lambda_{ij} = \Lambda \phi_i \left(\delta_{ij} - \phi_j \right) \, , \tag{2.51}$$

that, in the limit of non-reacting components with equal size ($v_i = v_0$) and interactions $\chi_{ij} = \chi_{i0}$, allows to recover Fick's diffusion law

$$\frac{\mathrm{d}\phi_i}{\mathrm{d}t} = D \nabla^2 \phi_i \, , \tag{2.52}$$

with $D = v_0 \Lambda k_B T$. Examining now the chemical rates, we notice that Eq. (2.49b) can be considered an expansion of Eq.(2.39) close to chemical equilibrium, i.e. if $\Delta\mu_a / k_B T \ll 1$.

Finally, we can repeat the same passages that led to Eq. (2.34), to derive dynamical equations of the conserved quantities

$$\frac{\mathrm{d}\psi_i}{\mathrm{d}t} = -\nabla \cdot \mathbf{j}_i^{\psi} \, , \tag{2.53}$$

where we have defined $\mathbf{j}_i^{\psi} = \sum_k Q_{ik}\mathbf{j}_k$. This implies, that at steady state, the flux associated with conserved quantities is constant in space.

Chapter 3

Controlling phase composition via molecular transitions

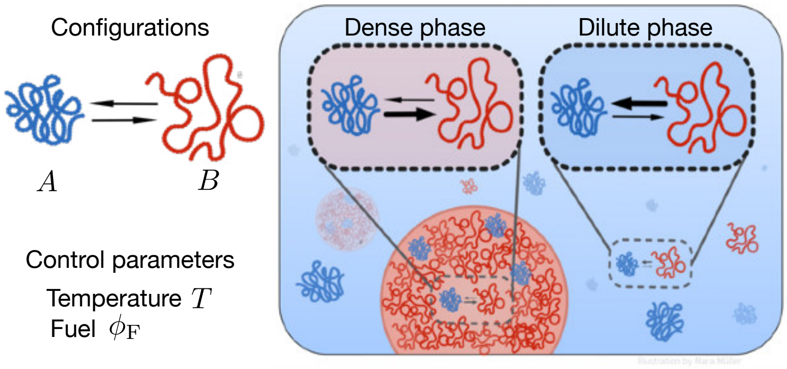

FIGURE 3.1: **Illustration of the model to study molecular transitions and phase separation.** In our model, we consider a molecule that can be found in two states A, B immersed in a solvent C_0. We allow reversible molecular transitions between A and B which are controlled by temperature T or fuel volume fraction ϕ_{F}. In the presence of phase separation, molecular transitions occur in the dense and dilute phases, respectively. Depending on the molecular interactions of A and B molecules, the total volume fraction of both components and their composition (i.e. the relative amount of B molecules) change in each of the phases. Illustration by Mara Müller.

Here, we apply the framework described in the previous chapter to mixtures composed of unstructured macromolecules, such as DNA or proteins, and a solvent. In our model, these macromolecules can undergo molecular transitions (e.g. changes in conformation or charge) between two states, referred to as A and B, see Fig. 3.1. The transition between the two states can be described with the chemical reaction scheme exemplified in the previous chapter, see paragraph 2.1.3. The corresponding transition rates depend on thermodynamic control parameters such as temperature T and macromolecule concentration, as well as fuel volume fraction ϕ_{F} that drives the transition away from thermodynamic equilibrium. In our model, both components A and B can phase-separate due to interactions among them and with the solvent, see Fig. 3.1. This project is the result of a very fruitful collaboration with Omar Adame-Arana and Xueping Zhao, under the supervision of Christoph Weber.

3.1 Molecular transitions at equilibrium

We introduce a ternary mixture composed of three components: C_0, the solvent, $C_1 = A$, and $C_2 = B$, with $v_A = v_B = v$, and $v/v_0 = \nu$. Its thermodynamic behaviour descends from the free energy density introduced in Eq. (2.3). In particular, the interactions among molecules are characterised by χ_{AB}, while χ_{A0} and χ_{B0} describe the interaction between the solvent and A and B, respectively. We recall that ω_i accounts for the free energy needed to create the molecular component i (e.g. via molecular transitions) in units of $k_B T$. Since the internal free energies are defined modulo a constant, we chose

$$\omega_A = 0\,, \qquad \omega_B = e_{\text{int}} - s_{\text{int}} T\,. \tag{3.1}$$

Here, e_{int} and s_{int} are the energetic and entropic differences between state A and B. As a prototypical example, we consider molecular transitions leading to an energy and entropy increase converting A to B, i.e. $e_{\text{int}} > 0$ and $s_{\text{int}} > 0$. Such a scenario corresponds for example to polymers breaking some internal bonds to adopt a more flexible conformation, with negligible change in the molecular volume.
The chemical equilibrium in Eq. (2.28) can be cast in the form

$$\frac{\phi_A}{\phi_B} = \exp\left[\frac{\nu}{k_B T}\Big(e_{\text{int}} - s_{\text{int}} T + \chi_{AB}\left(\phi_A - \phi_B\right) + \left(\chi_{B0} - \chi_{A0}\right)\left(1 - \phi_{\text{tot}}\right)\Big)\right] \tag{3.2}$$

that can be used to determine the so-called melting temperature, T_{m}, at which $\phi_A = \phi_B = \phi_{\text{tot}}/2$, i.e. the mixture is equally composed of A and B

$$T_{\text{m}} = \frac{e_{\text{int}} + \left(\chi_{B0} - \chi_{A0}\right)\left(1 - \phi_{\text{tot}}\right)}{s_{\text{int}}}\,. \tag{3.3}$$

Above and below T_{m} the favoured molecular state is B and A, respectively. The melting temperature can be shifted by tuning the internal energy e_{int} and entropy s_{int}, parameters that are easy to control experimentally. In this section, we study the equilibrium phase diagrams as a function of the conserved quantity associated with the chemical reaction, namely the total volume fraction ϕ_{tot} as described in paragraph 2.1.3, and the rescaled temperature T/T_0, with

$$T_0 = \chi_{B0}/k_B\,. \tag{3.4}$$

In such phase diagrams, the binodal lines separate demixed and mixed thermodynamic states. Along the binodal, we also depict the composition in terms of the relative abundance of B molecules, ϕ_B/ϕ_{tot}, see the colour code in Fig. 3.2. We prefer ϕ_B/ϕ_{tot} to the reaction extent $\xi = \phi_B/\nu$ introduced before since it provides more direct information on the relative composition of the mixture. We then study how such phase diagrams are affected by molecular transitions, described by the melting temperature T_{m}, defined in Eq. (3.3), and interaction strengths. As a reference system, we consider a binary mixture composed of only B and W molecules, see the black lines in Figs. 3.2. This case corresponds to suppression of the A conformation, achieved for $\omega_A \gg \omega_B$, for which $\phi_{\text{tot}} = \phi_B$. In all our studies, we choose the relative molecular volume $\nu = 2$ to account for differences in molecular volumes between macromolecules and water.

3.1.1 Reentrant phase behaviour

We first focus on the class of system (i), defined via

$$\chi_{AB} \sim \chi_{B0}\,, \qquad \chi_{A0} \ll \chi_{B0}\,. \tag{3.5}$$

With this choice of parameters, A can be thought of as an inert conformation in which the interacting sites are self-saturated due to the formation of internal bonds, while B is the interacting conformation. This becomes clear when considering that, in the limit $\chi_{AB} = \chi_{B0}$, the quadratic part of Eq. (2.3) reduces $\chi\phi_B(1-\phi_B)$. Along with the binodal, in Fig. 3.2 a) we also plot the melting curve $T_{\mathrm{m}}(\phi_{\text{tot}})$, defined in Eq. (3.3). For this choice of parameters, T_{m} decreases with ϕ_{tot}, meaning that the denser the mixture, the more B, which is the interacting conformation, would be produced at the expense of A. As is clear from Fig. 3.2 a), at high temperatures entropy dominates, thus the system remains homogeneous, and mainly composed of the conformation B, which is entropically favoured. Lowering the temperature below a threshold called the upper critical solution temperature T_c, the system demixes into a ϕ_{tot}-rich and a ϕ_{tot}-poor phase, in the following referred to as the dense and dilute phase, respectively. In the vicinity of T_c, the state B dominates in both phases. This can be quantified via the colour code encoding the system composition, defined as the relative amount of molecules in the B conformation, ϕ_B/ϕ_{tot}.

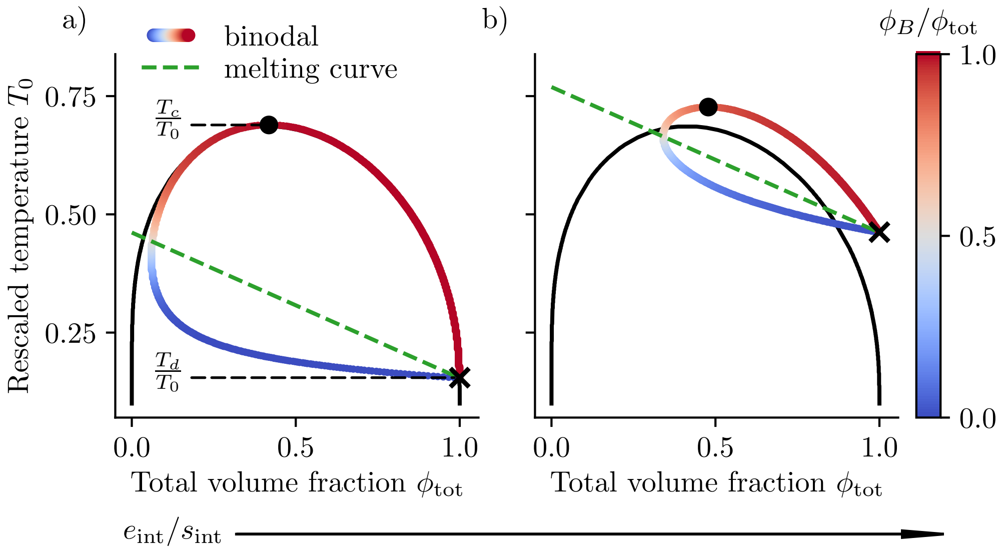

FIGURE 3.2: **Molecular transitions can lead to a lower critical dissolution temperature.** The binodal encompasses the demixing region in the plane spanned by total volume fraction ϕ_{tot} and rescaled temperature T/T_0. The composition of each phase is indicated by the colour code displayed on each of its branches. The black line corresponds to the binary B-W reference mixture. a) Due to the presence of molecular transitions, the phase diagram becomes reentrant, i.e., bounded above from the critical temperature T_c but also from below by a lower dissolution temperature T_d. b) Increasing e_{int}, the binodal is upshifted until the demixing region shrinks into a point for $e_{\text{int}} = s_{\text{int}} T_0\, \nu/2$.

The temperature at which the dilute branch of the binodal and the melting curve intercept determines the regime where coexisting phases differ not only in ϕ_{tot}, but also in the amount of B relative to A, see the colour code in Fig. 3.2. This is intuitive since, according to the definition of the melting curve (Eq. (3.3)), below the interception temperature in the dense branch $\phi_B > \phi_A$, while in the dilute one $\phi_B < \phi_A$. Along with the change in composition in the dilute branch, as the temperature decreases the ϕ_{tot} domain corresponding to phase separation shrinks and shifts close to $\phi_{\text{tot}} = 1$. This is because, with this choice of parameters, B molecules are the only interacting ones, to have phase separation the system must contain enough B. According to the melting curve, this is guaranteed for high ϕ_{tot}. The fact that B molecules are the only interacting ones explains also why the composition changes along the dilute branch but remains rather uniform in the dense branch. In fact, the temperature at which the melting curve and the dense cross, corresponding to the A molecules populating the dense phase, determines the dissolution of the two phases. In other words, depletion of the interacting material B due to internal energy gain ultimately leads to a lower dissolution temperature T_{d}, below which the system cannot phase separate. The dissolution temperature T_{d} can be estimated setting $\phi_{\text{tot}} = 1$ in the definition of the melting temperature, see (3.3), leading to

$$T_{\text{d}} = \frac{e_{\text{int}}}{s_{\text{int}}} \, . \tag{3.6}$$

Systems that exhibit both an upper critical solution temperature T_c and a lower dissolution temperature T_d, are called *reentrant*. In such cases, both increasing and decreasing the temperature leads to a phase transition from a demixed to a mixed state. Increasing the internal energy stored in the A component, e_{int} enhances the dominance of the molecular transition at low temperatures, and according to Eq. (3.6), an increase in T_{d}, see Fig. 3.2 b). For high enough e_{int} the melting curve passes gets close to the critical point of the reference binary mixture (composed of B and the solvent only), indicated by a black dot in Fig. 3.2 b). In this regime, the upper critical solution temperature T_{c} and critical volume fraction ϕ_{c} exceed the corresponding values in the binary case. This is because, at the interception between $T_{\text{m}}$and the dilute branch of the binodal, the dilute phase is composed of A and B in equal amounts.

Even though, with our choice of interaction parameters, B effectively repels both A and the solvent, differences in molecular volumes of A and B with respect to the solvent (i.e. $\nu > 1$) favour phase-separating B from A. In other words, the addition of A and B in the dilute and dense phase respectively, at the expense of the solvent, leads to an entropic advantage. This implies that the two phases will be up-shifted in ϕ_{tot} leading to two coexisting phases rich in B and A, respectively, instead of B and solvent rich, as in the binary reference, and an increase in critical temperature. This effect can be appreciated by comparing panels a) and b) in Fig.3.2, and manifests only for $\nu > 1$.

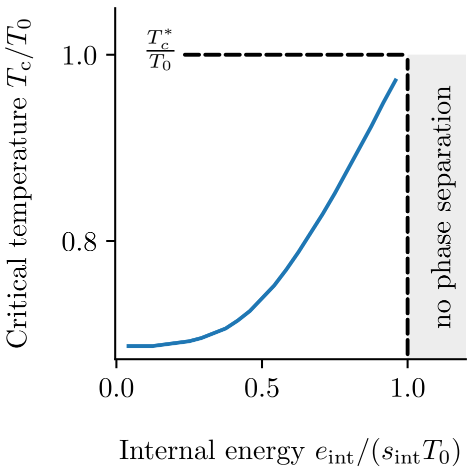

FIGURE 3.3: **Scaling of the critical temperature with the internal energy** For $e_{\text{int}} = 0$ we get the critical temperature of the binary reference $Tc/T_0 = (\nu + 2\sqrt{\nu} + 1)/2$ while for $e_{\text{int}} = s_{\text{int}}T_0\,\nu 2$, we get $T_c = T_c^* = T_0\nu/2$.

To sum up, the higher the internal energy e_{int} the lower the solvent amount is present in both phases. This implies that the critical temperature, has an upper bound, as shown in Fig 3.3. In fact in the limit of zero solvent, the polymer blend composed of A and B only phase separate below $T_c^* = T_0\,\nu/2$. Thus we find a threshold e_{int}^* at which the phase diagram shrinks to a point, and below which the system remains homogeneous for all ϕ_{tot} and T values. This threshold can be found imposing that $T_d = T_c^*$ which, recalling Eq. (3.6), leads to

$$e_{\text{int}}^* = \frac{\nu}{2}\, s_{\text{int}}T_0\,. \tag{3.7}$$

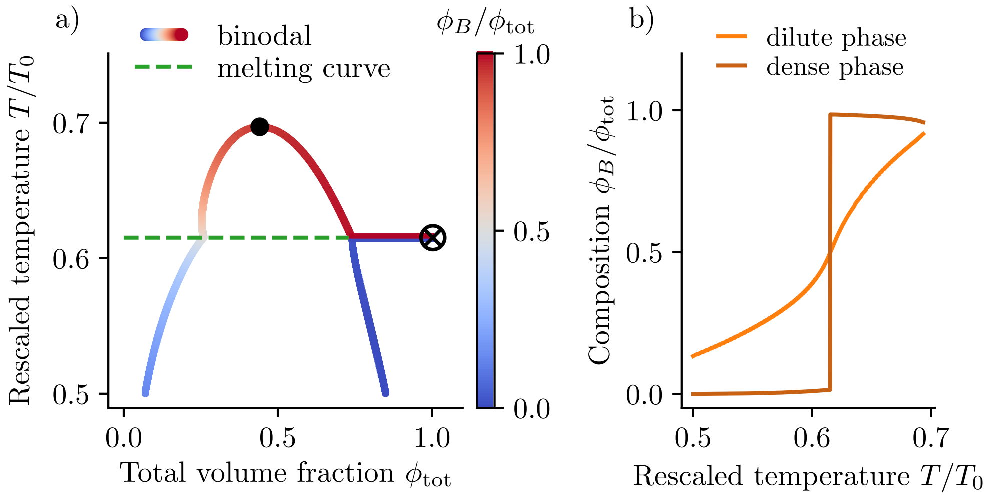

FIGURE 3.4: **Strong interactions of both states lead to a first-order phase transition in the composition of the dense phase.** a) In the limiting case of $\chi_{A0} = \chi_{B0}$, for sufficiently high χ_{AB}, the melting curve becomes horizontal $T_m = e_{\mathrm{int}}/s_{\mathrm{int}}$ and coincide with a triple line (green dashed line) at which a dilute phase coexists with two dense phases of different compositions. Such two dense phases have collapsed into the degenerate point at $\phi_{\mathrm{tot}} = 1$ ($\otimes$ symbol). Note that both, the order parameter ϕ_{tot} and the relative composition $\phi_B/\phi_{\mathrm{tot}}$ are discontinuous at T_{m}. b) Quantification of the compositional jump in the dense phase and comparison with the continuous variation of the composition in the dilute phase.

3.1.2 Temperature induced first-order transition in phase composition

We now consider another category of systems, class (ii), for which both components have the same effective interaction with the solvent

$$\chi_{A0} = \chi_{B0} \,, \quad \chi_{AB} > \chi_{B0} \,. \tag{3.8}$$

For simplicity, we now fix e_{int}. With this choice of parameters, the dense phase composition can change, and for sufficiently high χ_{AB} it does so discontinuously, see Fig. 3.4 a). The transition occurs at the melting temperature, which loses its dependence on ϕ_{tot} and reads $T_{\mathrm{m}} = e_{\mathrm{int}}/s_{\mathrm{int}}$. As a result, the melting curve becomes horizontal and denotes a triple line; see the dashed green line in Fig. 3.4 a). At the corresponding triple line temperature, three phases coexist for any value of ϕ_{tot} between the dilute binodal and 1. The reason is that for $\chi_{A0} = \chi_{B0}$, both molecular states have the same phase separation propensity from the solvent, and the internal free energy balance determines the composition of the dense phase.

In Fig. 3.4 b) we quantify the change in dense phase composition and we show that, in contrast, the composition of the dilute phase changes continuously. The discontinuous change in the composition of the dense phase is a fingerprint of three-phase coexistence in the underlying ternary phase diagram, which is typical for high χ_{B0}, χ_{A0} and $\chi_{AB} > 0$ and will be analysed in the next session (Fig. 3.6). The jump in $\phi_B^{\mathrm{I}}/\phi_{\mathrm{tot}}^{\mathrm{I}}$ can then be explained with a mechanism similar to the one described in Fig 2.4. Indeed changing temperature implies changing the internal free energy

ω_B, without altering significantly the underlying ternary phase diagram. We notice that, in our case, the molecular transition at thermodynamic equilibrium reduces the dimensionality of the manifold in which points associated with three-phase coexistence live, in agreement with the Gibbs rule (see Eq. (2.31)). In our case, the molecular transition at thermodynamic equilibrium reduces also the dimensionality of the domain in which three-phase coexistence is observed from a plane (green triangle in Fig. 2.4 a) or Fig. 3.6 d)), to a line (portion of the green dashed line within the binodal in Fig 3.4 a)). The coexistence of three phases and thus also the jump in dense phase composition is controlled by the effective interaction χ_{AB}, for a detailed discussion see Ref. [40].

3.2 Phase separation kinetics with molecular transitions maintained away from equilibrium via fuel

In the last section, we focused on how temperature affects the composition of coexisting phases. Temperature is a great control parameter for in vitro systems, however, there is no evidence that living systems control their temperature to regulate phase separation. In living cells, molecular transitions are regulated by a "fuel" component F which affects the balance between the two molecular states. A prototypical example is phosphorylation, where we can identify ATP as the fuel whose hydrolysis is known to regulate the balance between phosphorylated states and thereby regulate protein phase separation [41, 42, 43].

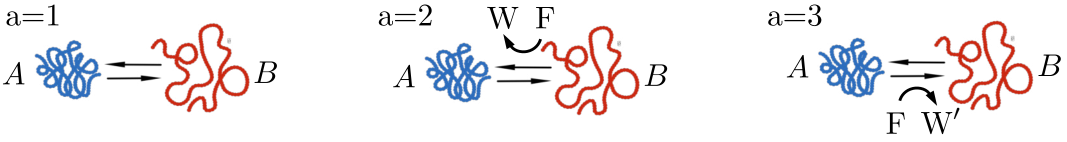

FIGURE 3.5: Illustration of the reaction pathways involving the fuel

In the previous chapter, we studied the kinetics of passive systems that relax to equilibrium, see Sec. 2.2. We now use a similar theoretical framework to account for the effect of the fuel [44, 32]. As illustrated in Fig. 3.5, this is done considering explicitly two new reaction pathways, ($a = 2$ and $a = 3$) that involve fuel and a waste component, F and W respectively. In analogy with Eq. (2.48), we consider kinetic equations of the form

$$\partial_t \phi_A = \nabla \cdot (\Lambda_A \nabla \bar{\mu}_A) + r \,, \tag{3.9a}$$

$$\partial_t \phi_B = \nabla \cdot (\Lambda_B \nabla \bar{\mu}_B) - r \,, \tag{3.9b}$$

where we chose $\Lambda_i = \phi_i \left(1 - \phi_A - \phi_B\right) \Lambda_D/(k_B T)$. Including now both reaction pathways in Fig. 3.5, with and without the fuel, we can write the reaction flux in the spirit of Eq. (2.39)

$$\begin{aligned} r = \Lambda_r \left[1 - \exp\left(\frac{\bar{\mu}_A - \bar{\mu}_B}{k_B T}\right)\right] + \Lambda_1 \left[1 - \exp\left(\frac{\bar{\mu}_A + \bar{\mu}_{\mathrm{W}} - \bar{\mu}_B - \bar{\mu}_{\mathrm{F}}}{k_B T}\right)\right] \\ + \Lambda_2 \left[1 - \exp\left(\frac{(\bar{\mu}_A + \bar{\mu}_{\mathrm{F}} - \bar{\mu}_B - \bar{\mu}'_{\mathrm{W}})}{k_B T}\right)\right] . \end{aligned} \tag{3.10}$$

We can now expand the first term for $(\bar{\mu}_B - \bar{\mu}_A)/k_B T \ll 1$ and the second and third at first order in ϕ_B and ϕ_A, respectively, to get

$$r = \Lambda_r \frac{(\bar{\mu}_B - \bar{\mu}_A)}{k_B T} + k_{\leftarrow}\, \phi_B \phi_{\mathrm{F}} - k_{\rightarrow}\, \phi_A \phi_{\mathrm{F}} \, . \tag{3.11}$$

Here, $k_{\leftarrow}$ and $k_{\rightarrow}$ are the volume fraction independent rate constants of the backward and forward transition, respectively. This independence of rate constants implies that detailed balance of the rates corresponding to the molecular transition is broken; for a conceptual discussion see Ref. [32]. In contrast to systems described in Sec. 2.2, a system with a reaction flux r given by Eq. (3.11) cannot fulfil the two equilibrium conditions of equal and spatially constant chemical potentials. Thus, stationary solutions to Eqs. (3.9) using Eq. (3.11) are non-equilibrium steady states. Consistently with this, in the absence of fuel ($\phi_{\mathrm{F}} = 0$), the reaction flux above reduces to Eq. (2.49b) and the system can relax to thermodynamic equilibrium. Thus, in our model, the fuel level controls how far the system is maintained away from thermodynamic equilibrium. Finally, we look for an equation for the fuel volume fraction ϕ_{F}. To this end, we focus on the case where the diffusion of fuel is fast compared to the diffusion of the macromolecules A and B, respectively. This limit is indeed reasonable for many biological systems since diffusivities for example between phase-separating macromolecules (proteins, RNA,...) and ATP differ by about two orders in magnitude [45, 46]. For simplicity, we consider the case of fuel being conserved, i.e., it is maintained constant in time. This scenario applies to living cells under physiological conditions and in in vitro systems, where these conditions could be realized by encapsulated ATP or regeneration of ATP. Moreover, we assume that the fuel molecules interact in the same way with A and B. In this case, we can quasi-statically slave the fuel volume fraction ϕ_{F} to the total concentration of A and B,

$$\phi_{\mathrm{F}}(\vec{x}, t) = \bar{\phi}_{\mathrm{F}} \left(\Gamma + \Upsilon\, \phi_{\mathrm{tot}}(\vec{x}, t)\right) \, , \tag{3.12}$$

where $\bar{\phi}_{\mathrm{F}}$ denotes the average volume fraction of fuel that is constant in time. The choice above allows capturing the partitioning of fuel by accounting for the spatial correlations between fuel and the total volume fraction ϕ_{tot}. The fuel partitioning coefficient P_{F}, which is experimentally accessible, determines the values of the parameters Γ and Υ in Eq. (3.12) (see Appendix B for a definition of P_{F} and the link to Γ and Υ). In the following, we choose three parameter sets for Γ and Υ corresponding to three qualitatively different scenarios. First, the fuel partitions inside the ϕ_{tot}-rich phase for $\Gamma = 0$ and $\Upsilon = 1/\bar{\phi}_{\mathrm{tot}}$. Second, fuel is enriched outside corresponding to

$\Gamma = -\Upsilon = 1/(1-\bar{\phi}_{\text{tot}})$. Finally, we also consider the case of a homogeneous fuel for $\Gamma = 1, \Upsilon = 0$. The latter case has been studied for example in Refs. [47, 48].

We numerically solve the kinetic Eqs. (3.9) and (3.11) in two dimensions with periodic boundary conditions combining the energy quadratization method [49, 49, 50] with with the stabilization method [51], see also Appendix F and G in Ref. [40].

3.2.1 Control of the number of coexisting phases via fuel

For the rest of the chapter, we study systems belonging to class (ii), defined in Eq. (3.8). We measure the effective rates in units of $t_D = L^2/\Lambda_D$, which represents the time a macromolecule takes to diffuse across a length $L = 100\sqrt{\kappa_{AA}/(k_{\mathrm{B}}T)}$, where L corresponds to the system size. Moreover, the length scale $\sqrt{\kappa_{AA}/(k_{\mathrm{B}}T)}$ approximates the droplet interface width [32]. In all simulations, we set $\Lambda_r = 5\,t_D^{-1}$. We also set the effective backward rate $\bar{\phi}_{\mathrm{F}}\,k_{\leftarrow} = 0$ and $k_{\rightarrow} = 2\,10^3\,t_D^{-1}$ and consider variations of the effective forward rate induced by the average fuel amount. In Fig. 3.6 a)-c) we plot representative stationary states at three different fuel levels. In the absence of fuel ($\bar{\phi}_{\mathrm{F}} = 0$), the system reaches its thermodynamic equilibrium, which for the parameters chosen here corresponds to an A-rich phase coexisting with a solvent-rich, see Fig. 3.6 a). Intermediate amounts of fuel induce a transition to a non-equilibrium stationary state comprised of three coexisting domains, see Fig. 3.6 b). For an even larger amount of fuel, the system transits to a non-equilibrium stationary state where B-rich domains stably coexist with a solvent-rich domain.

As expected, for high values of $k_{\rightarrow}$ and $k_{\leftarrow}$, we find that the local composition of each domain is no more governed by the thermodynamic equilibrium values. The effective description in terms of a single degree of freedom (i.e. ϕ_{tot}), discussed in Sect. 2.1.3 and Sect. 2.1.4) breaks down, and the system must be characterised by two degrees of freedom (i.e., ϕ_A and ϕ_B). The corresponding ternary phase diagram for the chosen temperature is depicted in Fig. 3.6 d). As anticipated at the end of the previous section, for parameters corresponding to case (ii), the phase diagram exhibits three-phase coexistence (green triangle), but also three domains of two-phase coexistence (blue, red and white). In the absence of fuel, the average (blue circled dot) is constrained by chemical equilibrium to the lower blue domain, thus the demixes in two phases, their composition specified by the blue dots in Fig. 3.6 d). Changing the fuel amount (and consequently the effective forward rate $k_{\rightarrow}\bar{\phi}_{\mathrm{F}}$) amounts to moving the average volume fraction vector along the conserved trajectory $\phi_B = \phi_{\text{tot}} - \phi_A$, as indicated by the gray arrow. For intermediate fuel amount, the average volume fraction moves into the green area, and the system exhibits three-phase coexistence, as we saw in Fig. 3.6 b).

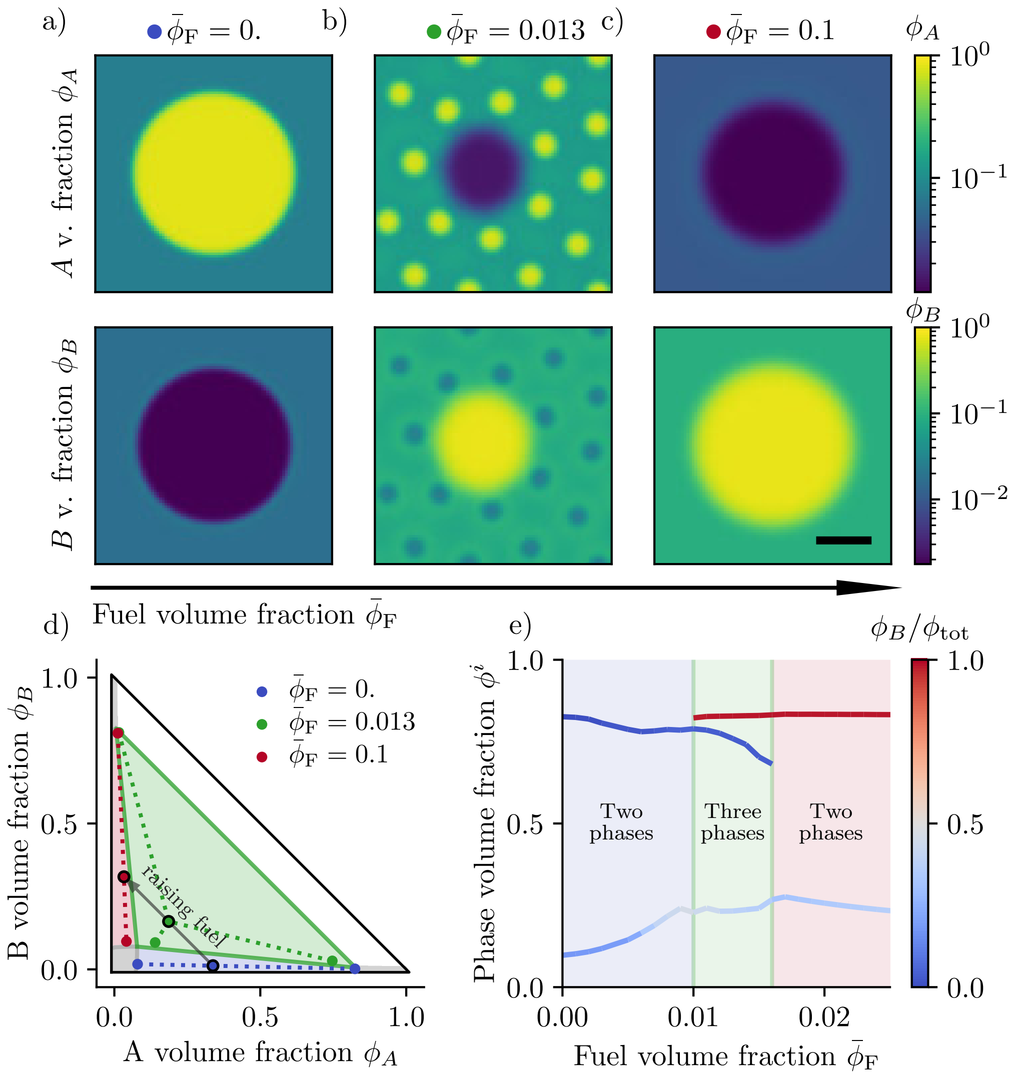

FIGURE 3.6: **Breaking detailed balance of the molecular transition enables controlling the number of distinct phases** a)-c) ϕ_A and ϕ_B spatial profiles at the stationary state for increasing fuel average volume fraction $\bar{\phi}_F$. a) Without fuel the system demixes into an A-rich phase and a solvent-rich phase, whose composition is set by thermodynamic equilibrium. b) Increasing fuel leads to the emergence of three phases: many A-rich drops and a single B-rich drop surrounded by a solvent-rich phase, respectively. c) Increasing further the fuel amount leads to two domains at steady state, enriched in B and solvent, respectively. d) Increasing the fuel level results in moving the average system composition in the ternary phase diagram. Average volume fractions for different fuel values are indicated by the circled coloured dots. The dashed lines connect average volume fractions with the volume fraction values in the respective demixed domains (colored dots), at steady state. We notice that the phase compositions are not too far from the reference values obtained imposing phase equilibrium in the ternary mixture, without chemical equilibrium. (e) The number of phases along with their density and composition as a function of the amount of fuel in the system. Here, interactions correspond to parameter set (ii), i.e. $\chi_{A0} = \chi_{B0}$, $\chi_{AB} > \chi_{B0}$,

Surprisingly, the local composition of each domain in the fueled system is almost equal to the equilibrium value of a ternary mixture without molecular transitions, as can be seen comparing the green dots with the vertices of the green triangle in Fig. 3.6 d). This remains true for high fuel amounts, for which the average volume fraction lies in the red domain corresponding to a B-rich droplet. Although the three-phase coexistence regime occupies the majority of the ϕ_A-ϕ_B-plane, the coexistence of three domains is actually only accessible over a narrow range of fuel values. To see this, compare the green regions in the phase diagram of Fig. 3.7 d) with the green region in Fig. 3.7 e). Thus, when the fuel is changed by an amount larger than this narrow window, the long-time, stationary state of the systems swaps from an A-rich to a B-rich domain. In general, this does not necessarily imply that the initial single droplet swaps its composition without dissolving. However, our results suggest the intriguing possibility, that under some conditions, a droplet may be able to change its composition without losing its identity, related to the profile of the total volume fraction.

3.2.2 Active switch of condensate composition

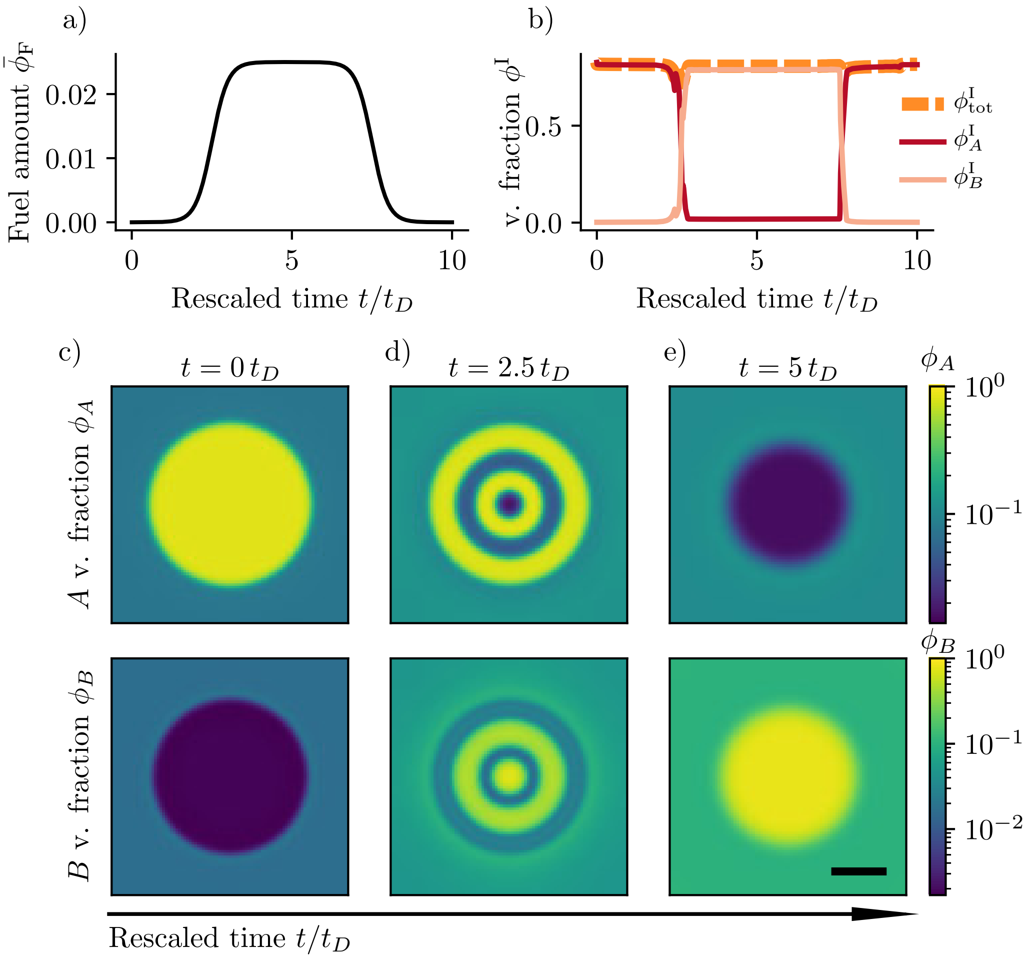

FIGURE 3.7: **Fuelling leads to droplet composition switch in time** The active switch in droplet composition is achieved by changing fuel in time according to the protocol in a). b) Time traces of ϕ_A, ϕ_B and ϕ_tot inside the dense phase show an abrupt compositional switch with time, reminiscent of the discontinuous switch observed at thermodynamic equilibrium when quasi-statically varying the temperature. c)-e) Snapshots of ϕ_A ϕ_B profile evolving in time within the first half of the fueling ramp shown in a). The rescaled temperature is kept constant to $T/T_0 = 0.525$.

To test the possibility of a single droplet kinetically swapping its composition with time as the fuel is increased, we initially start with an A-rich droplet at thermodynamic equilibrium ($\bar{\phi}_\mathrm{F} = 0$) and gradually increase the average fuel volume fraction until it reaches a plateau value, and then gradually decrease it, see Fig. 3.7 a). This causes an abrupt change in the composition of the dense phase, defined by means of a threshold in the total volume fraction, i.e. $\phi_\text{tot} > \phi^*_\text{tot}$, as can be seen in Fig. 3.7 b). Here we have chosen

$$\phi^*_\text{tot} = (\phi^\text{max}_\text{tot} + \phi^\text{min}_\text{tot})/2 + \delta_\text{tot}\,, \tag{3.13}$$

where $\phi_{\text{tot}}^{\text{max}}$ and $\phi_{\text{tot}}^{\text{min}}$ correspond to the maximum and minimum value of $\phi_{\text{tot}}(x)$, for a given time, while $\delta_{\text{tot}} = 0.4\,(\phi_{\text{tot}}^{\text{max}} - \phi_{\text{tot}}^{\text{min}})$. As the average fuel volume fraction is increased, a B-rich domain appears in the centre of the initial A-rich droplet. This domain grows and splits into concentric rings enriched in A and B, respectively, see Fig. 3.7 d). The outermost B-rich domain radially propagates inwards and outwards facilitating the formation of a final B-rich droplet. This inversion occurs approximately concomitant to the average fuel amount exceeding some specific value, see Fig. 3.7 e). Thus, the composition has indeed swapped with time compared to the initial state. As the fuel is gradually decreased, B material is consumed causing the droplet to shrink and a release of A material near its interface. This process forms an A-rich outer ring that relaxes with time to the spherical shape – the composition has returned back to its initial value. These results demonstrate that the composition of a droplet can indeed be controlled and reversibly switched by fuel that breaks detailed balance of the rates without dissolving and re-nucleating the droplet at another position.

Chapter 4

Controlling the shape of coexisting phases via molecular transitions

In the previous chapter, we generalised our reaction scheme to account for the presence of a fuel component. We have shown that breaking the detailed balance of the rates, via constant fuel supply, causes deviations from chemical equilibrium, thus paving the way for controlling phase composition. We also discussed how maintaining chemical reactions away from equilibrium leads to violations of the Gibbs phase rule, in turn releasing the strict limitations on the dimension of multi-phase coexistence regions (Eq. (2.31)). In our example, breaking detailed balance of the rates led to three-phase coexistence for a wide temperature range, instead of fine-tuned temperature values imposed by equilibrium (compare Fig. 3.4 with Fig. 3.6). Accounting for the presence of the fuel, we could not resort to the dimensional reduction coming from chemical equilibrium (see Sect, 2.1.3), but it proved useful to refer to the underlying M dimensional phase diagram. However, this has many limitations, as can be clearly appreciated by taking a closer look at the patterns that emerged in the last chapter, like the fixed-sized droplets in Fig. 3.6 b) and the (transient) rings in Fig. 3.6 d). In fact, breaking detailed balance of the rates, in general, prevents both the relaxation to chemical and phase equilibrium. In this chapter, we focus on non-equilibrium patterns that emerge due to fuel-driven chemical reactions. We first discuss the impact of interaction propensity and effective rates on the emergence of patterns and then introduce a simplified framework to characterise rings. We then show experimental evidence of an analogue pattern in 3D, namely spherical shells, forming in fuelled coacervate systems. We conclude by showing that theoretical predictions are in good agreement with experimental results. The results presented here, have been obtained within a very fruitful collaboration involving Jonathan Bauermann, Frank Jülicher and Christoph Weber on the theory side, and Alexander Bergmann, Carsten Donau, and Job Boekhoven on the experimental side.

4.1 Fuel controls the shape of coexisting phases

We start from the ternary mixture described in previous chapters, composed of the solvent and a molecule in two states (A and B). We consider the classes of systems outlined in the previous chapter: (i) weak A-solvent interactions: $\chi_{A0} \ll \chi_{B0}$, while $\chi_{AB} \sim \chi_{B0}$ and (ii) strong A-solvent and A-B interactions: $\chi_{A0} \sim \chi_{B0}$, with $\chi_{AB} > \chi_{B0}$. At thermodynamic equilibrium, we observed reentrant phase behavior for (i), see Fig. 3.2, and a discontinuous phase transition in droplet composition for (ii), see Fig. 3.4. We study the system kinetic, described in Eq. (3.9), considering both a thermodynamic and a fuel-related contribution to the reaction flux; see Eq. (3.11). Most importantly, the fuel-related contribution breaks detailed balance of the rates. This causes the system to settle into non-equilibrium stationary states which differ from the thermodynamic equilibrium one in terms of the number of phases, phase composition, and morphology. To classify these non-equilibrium states, we numerically solve Eqs. (3.9) together with Eq. (3.11), initializing the system with one droplet of total volume fractions and A-B-composition taken from the corresponding thermodynamic phase diagrams. We then track the interfaces between A-rich, B-rich, and solvent-rich domains, shown by dashed blue and red lines in Fig. 4.1 a) and d), defined via a threshold in the functions $\phi_A(x)$ and $\phi_B(x)$ respectively. As in the previous chapter, we have chosen the threshold based on the conserved quantity ϕ_{tot}, namely

$$\phi_A^* = \phi_B^* = (\phi_{\text{tot}}^{\text{max}} + \phi_{\text{tot}}^{\text{min}})/2 + \delta_{\text{tot}} \, , \tag{4.1}$$

where $\phi_{\text{tot}}^{\text{max}}$ and $\phi_{\text{tot}}^{\text{min}}$ correspond to the maximum and minimum value of $\phi_{\text{tot}}(x)$, for a given time, while $\delta_{\text{tot}} = 0.4\,(\phi_{\text{tot}}^{\text{max}} - \phi_{\text{tot}}^{\text{min}})$. We find the emergence of various patterns ranging from equally sized droplets to rings and stripes (see Fig. 4.1 a), b), d), e), and SI movies I-VII in Ref [40]). In our analysis, we focus on two sets of parameters:

Class (i) is defined by weak A-solvent interactions: $\chi_{A0} \ll \chi_{B0}$, while $\chi_{AB} \sim \chi_{B0}$, we find that the ϕ_{tot}-rich phase is mainly composed of B and that the inside composition hardly varies due to the presence of fuel; Fig. 4.1 c). However, the fuel can induce the formation of patterns that are significantly different from the corresponding equilibrium state, composed of a single droplet. We find that there is an extended region in the $k_{\rightarrow}$-$k_{\leftarrow}$ state diagrams where patterns emerge, enclosed by the grey line in Fig. 4.1 c). Close to the onset of pattern formation, we observe stable ring-like patterns, see Fig. 4.1 a). For increasing effective backward rate $\bar{\phi}_{\text{F}}\, k_{\leftarrow}$, we often observe rings coexisting with droplets, see SI Movie II. For even larger effective rates $\bar{\phi}_{\text{F}}\, k_{\leftarrow}$, rings break up leading to the emergence of equally sized droplets (Fig. 4.1 b). Equally sized droplets have been reported in a model using a Ginzburg-Landau type of free energy [48]. Droplets can also strongly deviate from their spherical shape (see SI Movie IV in Ref. [40]) and deform into elongated domains reminiscent of stripes.

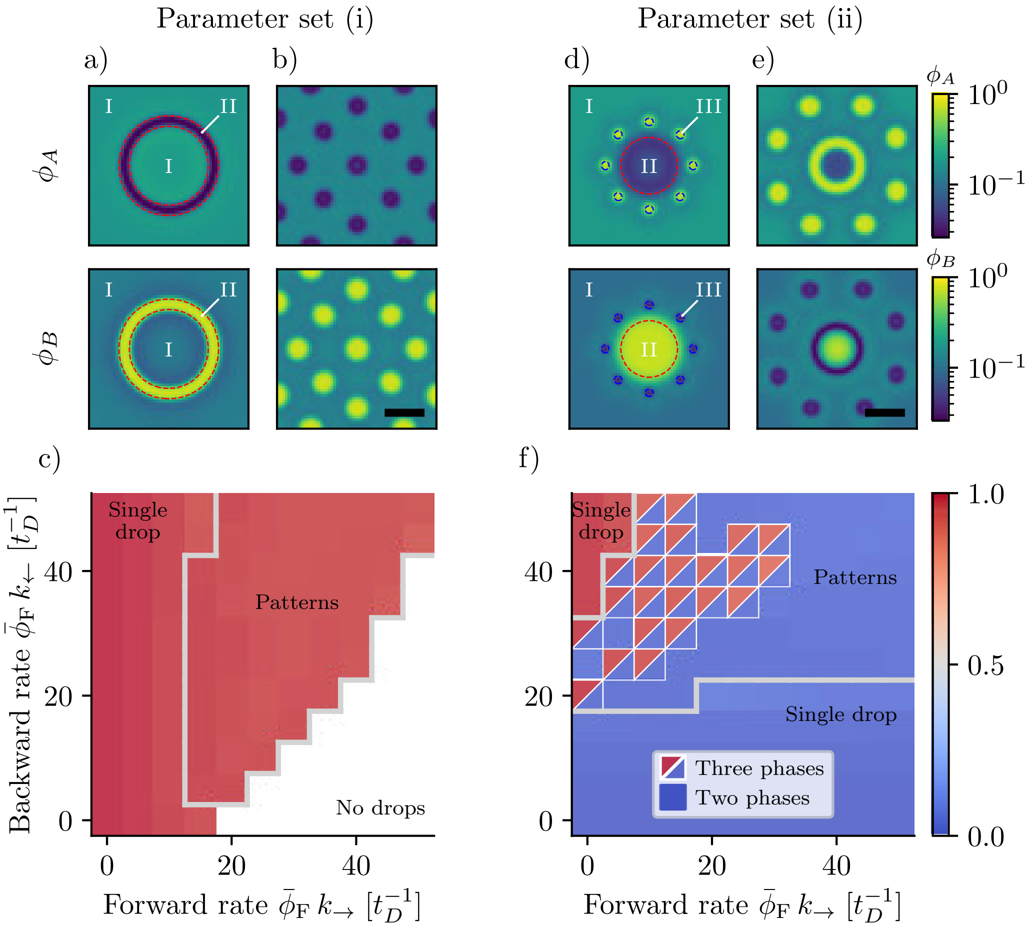

FIGURE 4.1: **Molecular transition breaking detailed balance leads to non-equilibrium stationary states.** We monitor the emergence of patterns by tracking the interface between solvent-rich (I), A-rich (II), and B-rich (III) domains (defined in Eq. (4.1)). For example, such tracked interfaces are shown by the dashed lines in a) and d), where the red and blue lines enclose B-rich and A-rich domains, respectively. These domains are the analogue of demixed phases at thermodynamic equilibrium. In a) and b) we display two prototypical fuel-induced non-equilibrium stationary states belonging to parameter set (i) defined by weak A-S interactions, namely $\chi_{A0} \ll \chi_{B0}$, $\chi_{AB} \simeq \chi_{B0}$. The state diagram in c) indicates out-of-equilibrium patterns corresponding to different values of the effective forward and backward rates ($\bar{\phi}_F\, k_\leftarrow$ and $\bar{\phi}_F\, k_\rightarrow$, respectively, entering in Eq. (3.11)), for parameter set (i). Here, the colour code indicates the composition of the dense domain in terms of the relative B amount (i.e. ϕ_B/ϕ_{tot}). For strong A-S interactions, $\chi_{A0} = \chi_{B0}$, $\chi_{AB} > \chi_{B0}$, corresponding to parameter set (ii), stationary patterns emerge composed of three domains distinct in composition d), e). In the state diagram f), such domains are indicated with two triangles of different colours in which each colour corresponds to the composition of the two distinct dense phases.

Class (ii) is characterized by strong A-solvent and A-B interactions: $\chi_{A0} \sim \chi_{B0}$, with $\chi_{AB} > \chi_{B0}$, the behavior in the $k_\rightarrow$-$k_\leftarrow$ state diagram changes significantly. In contrast to the previous case, for the temperature value chosen ($T = 0.525T_0$) the initial equilibrium state is a droplet composed mainly of A. Increasing the effective forward rate for low effective backward rates leads to a transition from an A-rich droplet to a B-rich droplet. In other words, for a large effective forward rate, this leads to a droplet of switched composition. Between the two regions in the $k_{\rightarrow}$-$k_{\leftarrow}$ plane corresponding to single droplets of different composition, there is a region where observe various kinds of patterns, see Fig. 4.1 d),e). In particular, for a low effective forward rate corresponding to the onset of pattern formation, we typically find that the shape of the A-rich domain deviates significantly from the initial single drop at thermodynamic equilibrium, while the composition of such domains remains close to the equilibrium value. Besides rings and equally sized drops, we also find patterns reminiscent of bubbly-phase separation [52], see SI Movie V in Ref. [40]. For higher effective forward rates and low backward rates, we find patterns where three domains of different compositions stably coexist, see the region marked with two triangles of different colours in Fig. 4.1 f). Representative stationary patterns composed of three domains are shown in Fig. 4.1 d), e). These patterns are spherically symmetric with a centered droplet enriched in B that is surrounded by a ring of smaller A-rich droplets of equal size. As mentioned above, for even higher effective forward rates, the system settles in a non-equilibrium stationary state composed of a single B-rich droplet. The rates for which these patterns emerge are influenced by the partitioning of fuel into the droplets. For details, see Fig.5 in Ref. [40]

4.2 Fuel-driven chemical reactions lead to vacuole formation

Among the patterns identified in the previous section, arguably the most interesting is the ring-like structure. What makes this pattern intriguing is the presence of two interfaces, which are penalised by the surface tension, and thus forbidden at equilibrium. To better characterise such a ring-like pattern, and study its 3D analogue, we now introduce a simplified kinetic description of multicomponent mixtures. This powerful approximation is usually referred to as the effective droplet description [32, 33] and can be exploited in the limit of sharp interfaces between different phases. This approach assumes local phase equilibrium at the interface.

4.2.1 The effective droplet model

We study first the case of a spherically symmetric system composed of two phases, separated by an interface at position R. We will call phase I the domain from $r = 0$ to $r = R$, and phase II the domain from $r = R$ to $r = R_{\text{sys}}$, the system boundary. For $\kappa_{ij} \to 0$, the interfaces among different phases become infinitely thin. The idea behind the effective droplet model is to expand the volume fraction around certain values, e.g. their values at the interface, defined as $\Phi_i^{\mathrm{I/II}} = \phi_i(r \to R^{\pm})$, where R is the droplet radius. Then, by means of appropriate relations, these volume fraction values and R must be determined self-consistently. We chose to linearise the dynamics in Eq. (2.48) with respect to the volume fraction values at the interface

$\phi_i(r \to R^{\pm}) = \Phi_i^{\mathrm{I/II}}$ leading to

$$\frac{\partial \phi_i}{\partial t} = -\nabla \cdot \mathbf{j}_i + c_i^{\mathrm{I/II}} + \sum_{j=1}^{M} k_{ij}^{\mathrm{I/II}} \left(\phi_i - \Phi_i^{\mathrm{I/II}} \right) , \tag{4.2}$$

with

$$\mathbf{j}_i = -\sum_{j=1}^{M} D_{ij}^{\mathrm{I/II}} \nabla \phi_j \, , \tag{4.3a}$$

$$k_{ij}^{\mathrm{I/II}} = \frac{\partial r_i}{\partial \phi_j} \, , \tag{4.3b}$$

$$c_i^{\mathrm{I/II}} = r_i(\Phi^{\mathrm{I/II}}) \, , \tag{4.3c}$$

and we have defined the diffusion coefficient

$$D_{ij}^{\mathrm{I/II}} = \sum_{k=1}^{M} \Lambda_{ik} \frac{\partial \bar{\mu}_k}{\partial \phi_j} \Big|_{\Phi^{\mathrm{I/II}}} . \tag{4.4}$$

Providing the appropriate boundary conditions at $r = R_{\text{sys}}$, these equations can be solved to get the spatial profiles $\phi_i^{\mathrm{I/II}}(r)$ of each component i in phases I and II, respectively, as a function of $\Phi_i^{\mathrm{I/II}}$, R. Following Ref. [19], we now assume that is possible to decouple the slow kinetic of $R(t)$ from the fast dynamics of the volume fraction fields. In other words, neglect transients in Eq. (4.2) and use its stationary solutions to compute the motion of the interface $R(t)$. In particular, starting from Eq. (4.2), adopting a reference frame comoving with the interface, and integrating between R^{-} and R^{+}, we get

$$\dot{R} \left(\Phi_i^{\mathrm{I}} - \Phi_i^{\mathrm{II}} \right) = \left(\mathbf{j}_i^{\mathrm{I}}(R^{-}) - \mathbf{j}_i^{\mathrm{II}}(R^{+}) \right) \hat{n}_r \, , \tag{4.5}$$

with $\hat{n}_r$ denoting the radial vector. The equation above relates fluxes and volume fractions at the interface to the motion of the interface. Considering the dynamics of conserved quantities, we get constraints on the possible values of $\dot{R}$. In fact, according to Eq. (2.53), we obtain

$$\frac{\mathrm{d}\psi_i^{\mathrm{I/II}}}{\mathrm{d}t} = -\nabla \cdot \mathbf{j}_i^{\psi\,\mathrm{I/II}} \, , \tag{4.6}$$

where the linearised currents read $\mathbf{j}_i^{\psi\,\mathrm{I/II}} = \sum_k Q_{ik} \mathbf{j}_k^{\mathrm{I/II}}$. Eq. (4.6) implies that, at steady state, the flux of conserved quantities is divergence-free. In this work, we focus on the case of closed systems imposing no flux of material through the system boundary. This assumption implies that the flux of conserved quantities also vanishes at R_{sys}:

$$\mathbf{j}_i^{\psi\,\mathrm{II}} \left(R_{\text{sys}} \right) = 0 \, . \tag{4.7}$$

This equation, together with the vanishing flux at $R = 0$, and Eq. (4.6) implies that, at a steady state, the current associated with conserved quantities must be zero everywhere: $\mathbf{j}_i^{\psi} = 0$. Applying Q_{ij} on both sides of Eq. (4.5), we find

$$\dot{R}\left(\Psi_i^{\mathrm{I}} - \Psi_i^{\mathrm{II}}\right) = 0\,, \tag{4.8}$$

where $\Psi_i^{\mathrm{I/II}}$ indicate the values of the conserved quantities at the interface. Equation (4.8) states that, in closed systems that are stationary with respect to Eq. (4.2), if the value of any conserved quantity differs across the interface, the interface velocity must vanish. Thus, unless the interaction parameters lead to $\Psi_i^{\mathrm{I}} = \Psi_i^{\mathrm{II}}$, we can use the effective droplet model only to study the stationary state of the system, and not the slow relaxation kinetics of $R(t)$.

In any case, we need to determine the $2M$ volume fractions $\Phi_i^{\mathrm{I/II}}$ and $R(t)$. To this aim, we impose local equilibrium across the interface:

$$\bar{\mu}_i\big(\{\Phi_j^{\mathrm{I}}\}\big) = \bar{\mu}_i\big(\{\Phi_j^{\mathrm{II}}\}\big)\,, \tag{4.9a}$$

$$\Pi\big(\{\Phi_j^{\mathrm{I}}\}\big) = \Pi\big(\{\Phi_j^{\mathrm{II}}\}\big) + 2\frac{\gamma}{R}\,, \tag{4.9b}$$

where we modified Eq. (2.9b) to account for the surface tension γ. These equations must be supplemented by global and local conservation laws. In particular, the conserved quantities obey the following global conservation laws

$$4\pi\int_0^R \psi_i(r) r^2\, dR + 4\pi\int_R^{R_{\mathrm{sys}}} \psi_i(r) r^2\, dR = \bar{\psi}_i\, V_{\mathrm{sys}}\,. \tag{4.10}$$

The remaining constraints can be found applying the matrix E_{ai}, defined in Eq. (2.18), to the expression for the interface velocity in Eq. (4.5), leading to

$$\dot{R} = \frac{\mathbf{j}_a^{\xi^{\mathrm{I}}} - \mathbf{j}_a^{\xi^{\mathrm{II}}}}{\Xi_a^{\mathrm{I}} - \Xi_a^{\mathrm{II}}}\,\hat{n}_r\,, \tag{4.11}$$

where we introduced $\Xi_a^{\mathrm{I/II}}$ as the values of the reaction extents at the interface. Equation (4.11) represents a set of local conservation laws for the fluxes of reaction extents. It states that molecules have to be provided (or removed) by the mismatch of the fluxes while moving the interface between two phases and having a finite difference in the volume fraction at the phase boundaries. Summing up, we have to distinguish between two cases:

i **All conserved quantities are continuous at the interface**. In this case, which requires a very specific choice of interaction parameters and molecular volumes, Eq. 4.8 does not constrain the interface velocity of volume fraction profiles that are stationary with respect to Eq. (4.2). For a given value of the radius R, we have to determine $2M$ values of the volume fractions at the interface, $\Psi_i^{\mathrm{I/II}}$ and the velocity $\dot{R}$. To this aim, we use the $M + 1$ local equilibrium conditions in Eq. (4.9), plus the $(M - R)$ conservation laws in Eq. (4.10), together with the R interface conditions in Eq. (4.11).

ii **At least a conserved quantity jumps at the interface**. In this case, according to Eq. 4.8, the assumption that volume fraction profiles are stationary states of the dynamics in Eq. (4.2), implies that the interface velocity vanishes. Even if, within the stationarity assumption of the volume fraction fields, we cannot study the slow relaxation kinetics of $R(t)$, we can still make use of the effective droplet model to find the stationary radius R^* and the corresponding interface values $\Phi_i^{\mathrm{I/II}}$. To this aim, we use the same set of constraints, namely the $M+1$ local equilibrium conditions in Eq. (4.9), the $M-R$ global conservation laws in Eq. (4.10), and the R interface conditions in Eq. (4.11).

4.2.2 Spinodal instability at the centre of chemically active droplets

As an example, we study the ternary mixture already introduced in the previous chapters, composed of the solvent, C_0, and two components A and B. We allow the chemical reaction $A \leftrightharpoons B$ and impose A and B to have the same molecular volume $v_A = v_B = \nu\, v_0$. We chose the conserved quantity $\psi = \phi_{\text{tot}} = \phi_A + \phi_B$ and the reaction extent $\xi = \phi_B/\nu$. We do not restrict the choice of interaction parameters and molecular volumes and allow jumps in the conserved quantity at the interface: $\phi_{\text{tot}}^{\mathrm{I}} \neq \phi_{\text{tot}}^{\mathrm{II}}$. According to the discussion in the previous chapter, this implies that the interface velocity $\dot{R}$ must vanish, at steady state of Eq. (4.2). Nevertheless, we can resort to the effective droplet model to determine the stationary radius and volume fraction profiles associated with a chemically active droplet and discuss its stability. For a ternary mixture, the reaction-diffusion equations in Eq. (4.2) read

$$\partial_t \phi_A = D^{\mathrm{I/II}} \nabla^2 \phi_A - k_{BA}^{\mathrm{I/II}} \phi_A + k_{AB}^{\mathrm{I/II}} \phi_B \,, \tag{4.12a}$$

$$\partial_t \phi_B = D^{\mathrm{I/II}} \nabla^2 \phi_B + k_{BA}^{\mathrm{I/II}} \phi_A - k_{AB}^{\mathrm{I/II}} \phi_B \,. \tag{4.12b}$$

In principle, the diffusion coefficients D_{ij} and the rate coefficients k_{ij} depend on the boundary values Φ_A around which we expanded, via Eq. (4.4) and Eq. (4.3b), respectively. In the following, we consider the possibility that both coefficients differ between the phases, however, for simplicity, we neglect any further volume fraction dependence of $D_{ij}(\Phi_i)$ and $k_{ij}(\Phi_i)$ in each phase. This assumption greatly simplifies the determination of the boundary values Φ_i without altering the qualitative results that can be obtained within the effective droplet model. Here, for simplicity, we have set $D_{ij}^{\mathrm{I/II}} = 0$ for $i \neq j$ and chosen equal diffusion coefficients for A and B, $D_{ii}^{\mathrm{I/II}} = D^{\mathrm{I/II}}$. Furthermore, we have set c_i, defined in Eq. (4.3c), to be zero in both phases. The last assumption should be taken with care since it implies that we can linearise the volume fractions around values corresponding to phase equilibrium and chemical equilibrium simultaneously. With these assumptions, the stationary solutions have the general form

$$\phi_A^{\mathrm{I/II}}(r) = \frac{a_1^{\mathrm{I/II}}}{r} + a_2^{\mathrm{I/II}} + a_3^{\mathrm{I/II}}\,\frac{\sinh\left(r\lambda^{\mathrm{I/II}}\right)}{r} + a_4^{\mathrm{I/II}}\,\frac{\cosh\left(r\lambda^{\mathrm{I/II}}\right)}{r}\,, \tag{4.13a}$$

$$\phi_B^{\mathrm{I/II}}(r) = \frac{k_{BA}^{\alpha}}{k_{AB}^{\alpha}}\left(\frac{a_1^{\mathrm{I/II}}}{r} + a_2^{\mathrm{I/II}}\right) - a_3^{\mathrm{I/II}}\,\frac{\sinh\left(r\lambda^{\mathrm{I/II}}\right)}{r} - a_4^{\mathrm{I/II}}\,\frac{\cosh\left(r\lambda^{\mathrm{I/II}}\right)}{r}\,, \tag{4.13b}$$

with

$$\lambda^{\mathrm{I/II}} = \sqrt{\frac{k_{AB}^{\mathrm{I/II}} + k_{BA}^{\mathrm{I/II}}}{D^{\mathrm{I/II}}}}\,, \tag{4.14}$$

and $a_i^{\mathrm{I/II}}$ integration constants to be fixed via boundary conditions. Imposing vanishing flux at the droplet centre and identifying $\phi_i^{\mathrm{I}} = \Phi_i^{\mathrm{I}}$, we can recast the solutions in phase I as:

$$\phi_A^{\mathrm{I}}(r) = \frac{\Phi_A^{\mathrm{I}} k_{BA}^{\mathrm{I}} - \Phi_B^{\mathrm{I}} k_{AB}^{\mathrm{I}}}{k_{AB}^{\mathrm{I}} + k_{BA}^{\mathrm{I}}}\,\frac{\mathrm{i}_0(\lambda^{\mathrm{I}} r)}{\mathrm{i}_0(\lambda_A^{\mathrm{I}} R)} + k_{AB}^{\mathrm{I}}\,\frac{\Phi_A^{\mathrm{I}} + \Phi_B^{\mathrm{I}}}{k_{AB}^{\mathrm{I}} + k_{BA}^{\mathrm{I}}}\,, \tag{4.15a}$$

$$\phi_B^{\mathrm{I}}(r) = \frac{\Phi_B^{\mathrm{I}} k_{AB}^{\mathrm{I}} - \Phi_A^{\mathrm{I}} k_{BA}^{\mathrm{I}}}{k_{AB}^{\mathrm{I}} + k_{BA}^{\mathrm{I}}}\,\frac{\mathrm{i}_0(\lambda^{\mathrm{I}} r)}{\mathrm{i}_0(\lambda_A^{\mathrm{I}} R)} + k_{BA}^{\mathrm{I}}\,\frac{\Phi_A^{\mathrm{I}} + \Phi_B^{\mathrm{I}}}{k_{AB}^{\mathrm{I}} + k_{BA}^{\mathrm{I}}}\,, \tag{4.15b}$$

where $\mathrm{i}_0(x) = \sinh(x)/x$ denote the spherical modified Bessel function of the first kind and 0th order. In phase II stationary solutions read:

$$\begin{aligned}\phi_A^{\mathrm{II}}(r) = {} & \frac{\Phi_A^{\mathrm{II}} k_{BA}^{\mathrm{II}} - \Phi_B^{\mathrm{II}} k_{AB}^{\mathrm{II}}}{k_{AB}^{\mathrm{II}} + k_{BA}^{\mathrm{II}}}\,\frac{\mathrm{k}_1(\lambda^{\mathrm{II}} R_{\mathrm{sys}})\mathrm{i}_0(\lambda^{\mathrm{II}} r) + \mathrm{i}_1(\lambda^{\mathrm{II}} R_{\mathrm{sys}})\mathrm{k}_0(\lambda^{\mathrm{II}} r)}{\mathrm{k}_1(\lambda^{\mathrm{II}} R_{\mathrm{sys}})\mathrm{i}_0(\lambda^{\mathrm{II}} R) + \mathrm{i}_1(\lambda^{\mathrm{II}} R_{\mathrm{sys}})\mathrm{k}_0(\lambda^{\mathrm{II}} R)} \\ & + k_{AB}^{\mathrm{II}}\,\frac{\Phi_A^{\mathrm{II}} + \Phi_B^{\mathrm{II}}}{k_{AB}^{\mathrm{II}} + k_{BA}^{\mathrm{II}}}\,,\end{aligned} \tag{4.16a}$$

$$\begin{aligned}\phi_B^{\mathrm{II}}(r) = {} & \frac{\Phi_B^{\mathrm{II}} k_{AB}^{\mathrm{II}} - \Phi_A^{\mathrm{II}} k_{BA}^{\mathrm{II}}}{k_{AB}^{\mathrm{II}} + k_{BA}^{\mathrm{II}}}\,\frac{\mathrm{k}_1(\lambda^{\mathrm{II}} R_{\mathrm{sys}})\mathrm{i}_0(\lambda^{\mathrm{II}} r) + \mathrm{i}_1(\lambda^{\mathrm{II}} R_{\mathrm{sys}})\mathrm{k}_0(\lambda^{\mathrm{II}} r)}{\mathrm{k}_1(\lambda^{\mathrm{II}} R_{\mathrm{sys}})\mathrm{i}_0(\lambda^{\mathrm{II}} R) + \mathrm{i}_1(\lambda^{\mathrm{II}} R_{\mathrm{sys}})\mathrm{k}_0(\lambda^{\mathrm{II}} R)} \\ & + k_{BA}^{\mathrm{II}}\,\frac{\Phi_A^{\mathrm{II}} + \Phi_B^{\mathrm{II}}}{k_{AB}^{\mathrm{II}} + k_{BA}^{\mathrm{II}}}\,,\end{aligned} \tag{4.16b}$$

where Φ_A^{II}, Φ_B^{II} are the interface volume fractions at $r = R$ and R_{sys} is the system size. Moreover, $\mathrm{k}_0(x) = \exp(-x)/x$ is the spherical modified Bessel function of the second kind and 0th order. The spherical modified Bessel function of the first and second kind and first order (i_1 and k_0, respectively) are defined through $\mathrm{i}_1(x) = \mathrm{i}_0'(x)$ and $\mathrm{k}_1(x) = -\mathrm{k}_0'(x)$. The A and B fluxes read

$$j_i^{\mathrm{I/II}}(r) = -D^{\mathrm{I/II}}\partial_r\phi_i^{\mathrm{I/II}}\,. \tag{4.17}$$

Now we can self-consistently determine the boundary values $\Phi_i^{\mathrm{I/II}}$, and the interface position R making use of the following $(M+1)$ conditions:

- **Phase equilibrium**

$$\bar{\mu}_A\big(\{\Phi_j^{\mathrm{I}}\}\big) = \bar{\mu}_A\big(\{\Phi_j^{\mathrm{II}}\}\big)\,, \tag{4.18a}$$

$$\bar{\mu}_B\big(\{\Phi_j^{\mathrm{I}}\}\big) = \bar{\mu}_B\big(\{\Phi_j^{\mathrm{II}}\}\big)\,, \tag{4.18b}$$

$$\Pi\big(\{\Phi_j^{\mathrm{I}}\}\big) = \Pi\big(\{\Phi_j^{\mathrm{II}}\}\big) + 2\frac{\gamma}{R}\,. \tag{4.18c}$$

- **Global material conservation**

$$\begin{aligned} V_{\mathrm{sys}}\,\bar{\phi}_{\mathrm{tot}} &= \int dV\,(\phi_A + \phi_B) \\ &= \frac{4}{3}\pi\left[(\Phi_A^{\mathrm{I}} + \Phi_B^{\mathrm{I}})R^3 + (\Phi_A^{\mathrm{II}} + \Phi_B^{\mathrm{II}})(R_{\mathrm{sys}}^3 - R^3)\right]\,. \end{aligned} \tag{4.18d}$$

- **Conservation across the interface**

$$j_B^{\mathrm{I}} = -j_B^{\mathrm{II}}\,. \tag{4.18e}$$

In the following, we introduce the time scale

$$\tau = R_{\mathrm{sys}}^2/D^{\mathrm{II}} \tag{4.19}$$

that will be the natural unit to measure rates. Two examples of the radial profiles ϕ_A and ϕ_B resulting from the solution of the equations above are displayed in Fig. 4.2 a) and b), for two different values of k_{AB}^{I}. Due to chemical reactions, moving away from the interface $r = R$, the volume fractions can vary from the values $\Phi_i^{\mathrm{I/II}}$, around which we have linearised. The variation becomes significant at distances from R comparable with the length scale $1/\lambda^{\mathrm{I/II}}$, introduced in Eq. (4.14). In both cases illustrated, the reaction-diffusion length scale λ^{II} is much larger than the system size, $1/\lambda^{\mathrm{II}} \sim 10R_{\mathrm{sys}}$, corresponding to flat profiles outside of the droplet. On the other hand, $1/\lambda^{\mathrm{I}} \sim 0.6R_{\mathrm{sys}}$ in a) and $1/\lambda^{\mathrm{I}} \sim 0.3R_{\mathrm{sys}}$ in b). As a result, A and B profiles vary mildly in a) while in b) the volume fractions at the droplet centre (red and blue circles) and at the $r = R$ (red and blue triangles) differ significantly. In Fig. 4.2 c) we plot volume fraction variations in the dense phase, on top of the phase diagram, for the same parameters used in a) and b). Since we imposed phase equilibrium across the interface, the volume fractions at $r = R$ (circles) must lie in the proximity of the binodal. The discrepancy is to the presence of surface tension γ. As mentioned before, chemical reactions lead to variations of the volume fraction profile with r. In particular, the volume fraction at the droplet centre may lie in the spinodal region, as is the case for parameters in b). Inside the spinodal region, homogeneous states become unstable for any perturbation. Thus, if volume fractions at $r = 0$ cross the spinodal line, spontaneous demixing occurs at the droplet centre. In Fig. 4.2 d) we depict the dependence of the volume fractions at the centre $\phi_i(0)$ on the rate k_{AB}^{I}, highlighting the value k^*, corresponding to crossing the spinodal. In Fig. 4.2 e) we depict the variation of the interface radius as a function of the rate k_{AB}^{I}, again highlighting k^*. Values above k^* are dashed since in this regime the droplet state becomes unstable.

We have shown that for $k^{\mathrm{I}}_{AB} > k^*$ chemical reactions lead to volume fractions at $r = 0$ that lie in the spinodal region. This would correspond to spontaneous demixing at the droplet centre, and thus the emergence of a third phase. We speculate that indeed for $k^{\mathrm{I}}_{AB} > k^*$ the stationary state of the system is composed of three phases separated by two interfaces. Unfortunately, to study this regime we cannot resort to the set of linearised equations in Eqs. (4.18). In fact, there we considered D^{I}_i to be constant, as given by the expression in Eq. (4.4). On the other hand, if the volume fractions in the dense phase deviate from their boundary values, this approximation can lead to contradictions. This becomes evident when the droplet centre crosses the spinodal, leading to a negative diffusion coefficient considering equations linearised around $\phi_i(0)$. For this reason, in the next session, we will introduce a new theoretical framework that will reveal to be useful for characterizing the stationary state in the regime $k^{\mathrm{I}}_{AB} > k^*$.

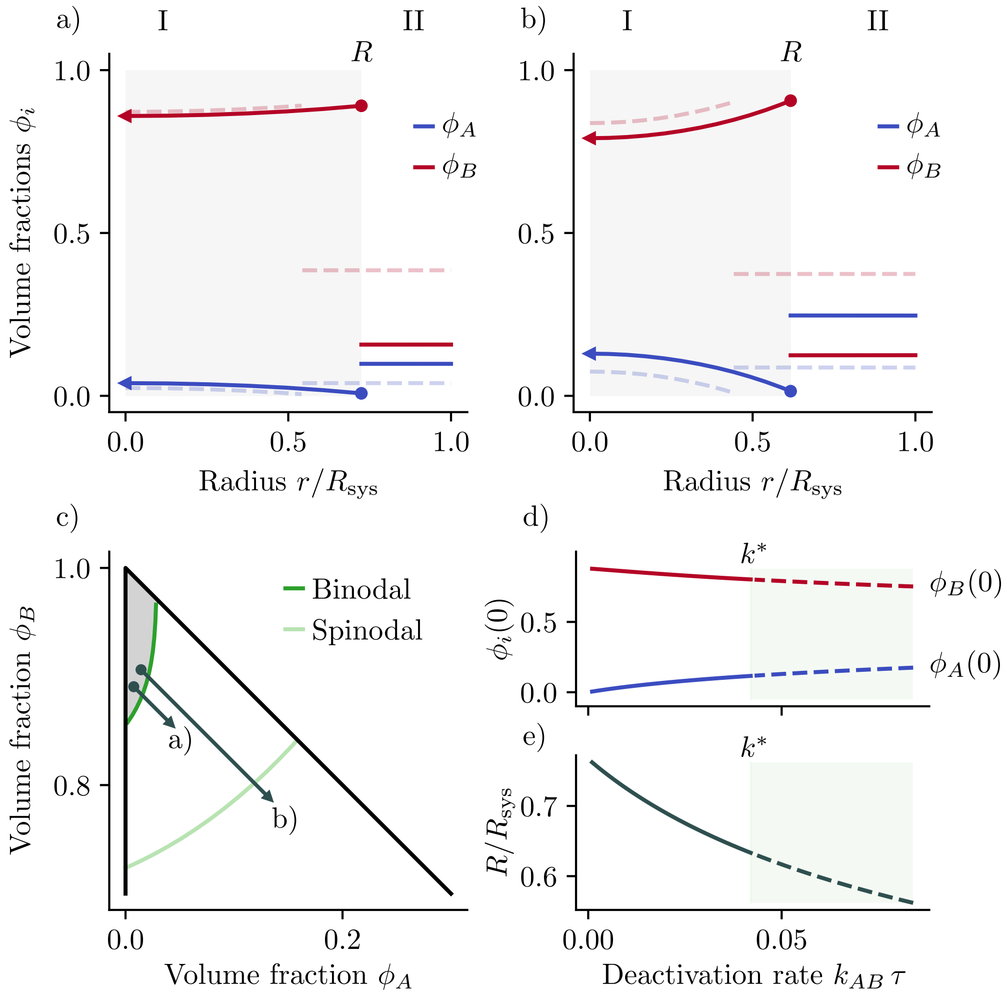

FIGURE 4.2: **Chemical reactions lead to spinodal instability at the droplet centre**. a) and b) concentration profiles corresponding to $k^{\mathrm{I}}_{AB} = 0.01$ and $k^{\mathrm{I}}_{AB} = 0.05$. Solid and dashed lines represent stable and unstable solutions of Eqs. (4.18), respectively. c) Concentrations at the interface R(circles) and at the droplet centre (triangles) for the parameters corresponding to a) and b) plotted on top of the phase diagram. For high values of the rate k^{I}_{AB}, the volume fractions at the droplet centre cross the spinodal region thus the droplet state becomes unstable. The dependence of R and of the volume fraction at the centre on k^{I}_{AB} are plotted in panels d) and e), respectively. Here, k^* denotes the onset of the spinodal instability at the droplet centre, where the droplet state becomes unstable. For this reason, we dash values of the radius and volume fraction at the centre above k^*.

4.2.3 Describing vacuoles within the effective droplet model

We study now the case of a spherically symmetric system composed of three phases, separated by an inner and an outer interface at position R_{in} and R_{out}, respectively. We will call phase I the domain from 0 to R_{in}, and phase II the domain from R_{out} to R_{sys}, the system boundary, and phase III the shell between R_{in} and R_{out}. We focus on the ternary mixture described in Sec 4.2.2 and previous chapters. Again, we assume the interfaces among different phases to be infinitely thin and solve reaction-diffusion equations analogue to Eqs. (4.2), namely

$$\partial_t \phi_A = D^\alpha \nabla^2 \phi_A - k^\alpha_{BA} \phi_A + k^\alpha_{AB} \phi_B \,, \tag{4.20a}$$

$$\partial_t \phi_B = D^\alpha \nabla^2 \phi_B + k^\alpha_{BA} \phi_A - k^\alpha_{AB} \phi_B \,, \tag{4.20b}$$

in the phases $\alpha = \mathrm{I}, \mathrm{II}, \mathrm{III}$. In the following, we will use the superscripts "I", "in", "out", and "II" to indicate quantities evaluated at R^-_{in}, R^+_{in}, R^-_{out}, R^+_{out}, respectively. For example, with this notation, the volume fractions at the boundaries read

$$\Phi^{\mathrm{I}}_i = \phi_i(r \to R^-_{\text{in}}) \,, \tag{4.21a}$$

$$\Phi^{\text{in}}_i = \phi_i(r \to R^+_{\text{in}}) \,, \tag{4.21b}$$

$$\Phi^{\text{out}}_i = \phi_i(r \to R^-_{\text{out}}) \,, \tag{4.21c}$$

$$\Phi^{\mathrm{II}}_i = \phi_i(r \to R^+_{\text{out}}) \,, \tag{4.21d}$$

for $i = A, B$. The stationary solutions of the reaction-diffusion equations (Eq. (4.20)) in phases I and II are identical to those presented in Eq. (4.15) and Eq. (4.15), respectively. The stationary profiles inside of the shell, instead, read

$$\begin{aligned}
\phi^{\mathrm{III}}_A(r) = {} & \frac{(\Phi^{\text{out}}_A k^{\mathrm{III}}_{BA} - \Phi^{\text{out}}_B k^{\mathrm{III}}_{AB}) \left[\mathrm{k}_0(\lambda^{\mathrm{III}} R_{\text{in}}) \mathrm{i}_0(\lambda^{\mathrm{III}} r) - \mathrm{i}_0(\lambda^{\mathrm{III}} R_{\text{in}}) \mathrm{k}_0(\lambda^{\mathrm{III}} r)\right]}{(k^{\mathrm{III}}_{AB} + k^{\mathrm{III}}_{BA}) \left[\mathrm{k}_0(\lambda^{\mathrm{III}} R_{\text{in}}) \mathrm{i}_0(\lambda^{\mathrm{III}} R_{\text{out}}) - \mathrm{i}_0(\lambda^{\mathrm{III}} R_{\text{in}}) \mathrm{k}_0(\lambda^{\mathrm{III}} R_{\text{out}})\right]} \\
& + \frac{(\Phi^{\text{in}}_A k^{\mathrm{III}}_{BA} - \Phi^{\text{in}}_B k^{\mathrm{III}}_{AB}) \left[\mathrm{k}_0(\lambda^{\mathrm{III}} R_{\text{out}}) \mathrm{i}_0(\lambda^{\mathrm{III}} r) - \mathrm{i}_0(\lambda^{\mathrm{III}} R_{\text{out}}) \mathrm{k}_0(\lambda^{\mathrm{III}} r)\right]}{(k^{\mathrm{III}}_{AB} + k^{\mathrm{III}}_{BA}) \left[\mathrm{k}_0(\lambda^{\mathrm{III}} R_{\text{in}}) \mathrm{i}_0(\lambda^{\mathrm{III}} R_{\text{out}}) - \mathrm{i}_0(\lambda^{\mathrm{III}} R_{\text{in}}) \mathrm{k}_0(\lambda^{\mathrm{III}} R_{\text{out}})\right]} \\
& + k^{\mathrm{III}}_{AB} \frac{(\Phi^{\text{in}}_A + \Phi^{\text{in}}_B - \Phi^{\text{out}}_A - \Phi^{\text{out}}_B) R_{\text{in}} R_{\text{out}}}{(k^{\mathrm{III}}_{AB} + k^{\mathrm{III}}_{BA})(R_{\text{out}} - R_{\text{in}}) r} \\
& + k^{\mathrm{III}}_{AB} \frac{(\Phi^{\text{out}}_A + \Phi^{\text{out}}_B) R_{\text{out}} - (\Phi^{\text{in}}_A + \Phi^{\text{in}}_B) R_{\text{in}}}{(k^{\mathrm{III}}_{AB} + k^{\mathrm{III}}_{BA})(R_{\text{out}} - R_{\text{in}})} \,,
\end{aligned} \tag{4.22a}$$

$$\begin{aligned}
\phi^{\mathrm{III}}_B(r) = {} & \frac{(\Phi^{\text{out}}_B k^{\mathrm{III}}_{AB} - \Phi^{\text{out}}_A k^{\mathrm{III}}_{BA}) \left[\mathrm{k}_0(\lambda^{\mathrm{III}} R_{\text{in}}) \mathrm{i}_0(\lambda^{\mathrm{III}} r) - \mathrm{i}_0(\lambda^{\mathrm{III}} R_{\text{in}}) \mathrm{k}_0(\lambda^{\mathrm{III}} r)\right]}{(k^{\mathrm{III}}_{AB} + k^{\mathrm{III}}_{BA}) \left[\mathrm{k}_0(\lambda^{\mathrm{III}} R_{\text{in}}) \mathrm{i}_0(\lambda^{\mathrm{III}} R_{\text{out}}) - \mathrm{i}_0(\lambda^{\mathrm{III}} R_{\text{in}}) \mathrm{k}_0(\lambda^{\mathrm{III}} R_{\text{out}})\right]} \\
& + \frac{(\Phi^{\text{in}}_B k^{\mathrm{III}}_{AB} - \Phi^{\text{in}}_A k^{\mathrm{III}}_{BA}) \left[\mathrm{k}_0(\lambda^{\mathrm{III}} R_{\text{out}}) \mathrm{i}_0(\lambda^{\mathrm{III}} r) - \mathrm{i}_0(\lambda^{\mathrm{III}} R_{\text{out}}) \mathrm{k}_0(\lambda^{\mathrm{III}} r)\right]}{(k^{\mathrm{III}}_{AB} + k^{\mathrm{III}}_{BA}) \left[\mathrm{k}_0(\lambda^{\mathrm{III}} R_{\text{in}}) \mathrm{i}_0(\lambda^{\mathrm{III}} R_{\text{out}}) - \mathrm{i}_0(\lambda^{\mathrm{III}} R_{\text{in}}) \mathrm{k}_0(\lambda^{\mathrm{III}} R_{\text{out}})\right]} \\
& + k^{\mathrm{III}}_{BA} \frac{(\Phi^{\text{in}}_A + \Phi^{\text{in}}_B - \Phi^{\text{out}}_A - \Phi^{\text{out}}_B) R_{\text{in}} R_{\text{out}}}{(k^{\mathrm{III}}_{AB} + k^{\mathrm{III}}_{BA})(R_{\text{out}} - R_{\text{in}}) r} \\
& + k^{\mathrm{III}}_{BA} \frac{(\Phi^{\text{out}}_A + \Phi^{\text{out}}_B) R_{\text{out}} - (\Phi^{\text{in}}_A + \Phi^{\text{in}}_B) R_{\text{in}}}{(k^{\mathrm{III}}_{AB} + k^{\mathrm{III}}_{BA})(R_{\text{out}} - R_{\text{in}})} \,,
\end{aligned} \tag{4.22b}$$

where we have imposed no flux boundary conditions at $r = 0$ and, since we restrict to closed systems, at $r = R_{\text{sys}}$. Furthermore, we have introduced

$$\lambda^{\text{III}} = \sqrt{\frac{k_{AB}^{\text{III}} + k_{BA}^{\text{III}}}{D^{\text{III}}}} \,. \tag{4.23}$$

The currents read

$$j_i^\alpha(r) = -D^\alpha \partial_r \phi_i^\alpha \,, \tag{4.24}$$

with $\alpha =$ I,II,III. We can now study the interfaces kinetics fixing R_{in} and determine the boundary values ϕ_i^{I}, ϕ_i^{in}, ϕ_i^{out}, ϕ_i^{II}, the outer interface position $\dot{R}_{\text{in}}$, and the interface velocities $\dot{R}_{\text{out}}$ and R_{out}, making use of the following conditions:

- **Phase equilibrium across the inner interface R_{in}**

$$\bar{\mu}_A\big(\{\Phi_j^{\text{I}}\}\big) = \bar{\mu}_A\big(\{\Phi_j^{\text{in}}\}\big) \,, \tag{4.25a}$$

$$\bar{\mu}_B\big(\{\Phi_j^{\text{I}}\}\big) = \bar{\mu}_B\big(\{\Phi_j^{\text{in}}\}\big) \,, \tag{4.25b}$$

$$\Pi\big(\{\Phi_j^{\text{I}}\}\big) = \Pi\big(\{\Phi_j^{\text{in}}\}\big) + 2\frac{\gamma}{R^{\text{in}}} \,. \tag{4.25c}$$

- **Phase equilibrium across the outer interface R_{out}**

$$\bar{\mu}_A\big(\{\Phi_j^{\text{out}}\}\big) = \bar{\mu}_A\big(\{\Phi_j^{\text{II}}\}\big) \,, \tag{4.25d}$$

$$\bar{\mu}_B\big(\{\Phi_j^{\text{out}}\}\big) = \bar{\mu}_B\big(\{\Phi_j^{\text{II}}\}\big) \,, \tag{4.25e}$$

$$\Pi\big(\{\Phi_j^{\text{out}}\}\big) = \Pi\big(\{\Phi_j^{\text{II}}\}\big) + 2\frac{\gamma}{R^{\text{out}}} \,. \tag{4.25f}$$

- **Global material conservation**

$$\bar{\phi}_{\text{tot}}\, V_{\text{sys}} = \int dV\, (\phi_A + \phi_B) \,. \tag{4.25g}$$

- **Unicity of the inner interface velocity $\dot{R}_{\text{in}}$**

$$\dot{R}_{\text{in}} = \frac{\mathbf{j}_A^{\text{in}} - \mathbf{j}_A^{\text{I}}}{\Phi_A^{\text{in}} - \Phi_A^{\text{I}}} \hat{n}_r = \frac{\mathbf{j}_B^{\text{in}} - \mathbf{j}_B^{\text{I}}}{\Phi_B^{\text{in}} - \Phi_B^{\text{I}}} \hat{n}_r \,. \tag{4.25h}$$

- **Unicity of the outer interface velocity $\dot{R}_{\text{out}}$**

$$\dot{R}_{\text{out}} = \frac{\mathbf{j}_A^{\text{out}} - \mathbf{j}_A^{\text{II}}}{\Phi_A^{\text{out}} - \Phi_A^{\text{II}}} \hat{n}_r = \frac{\mathbf{j}_B^{\text{out}} - \mathbf{j}_B^{\text{II}}}{\Phi_B^{\text{out}} - \Phi_B^{\text{II}}} \hat{n}_r \,. \tag{4.25i}$$

As demonstrated for the case with one interface only, see Eq. (4.6)), at stationary state, the current associated with the conserved quantity ϕ_{tot}, namely

$$\mathbf{j}_{\text{tot}}^\alpha = -D^\alpha \nabla \phi_{\text{tot}}^\alpha \,, \tag{4.26}$$

must be constant in the phases. For closed system, this implies $\mathbf{j}_{\text{tot}}^{\text{I}} = \mathbf{j}_{\text{tot}}^{\text{II}} = 0$ while, in principle, $\mathbf{j}_{\text{tot}}^{\text{III}}$ does not have to vanish. Thus, we can rewrite the interface velocities, defined in Eq. (4.25h) and Eq. (4.25h), as

$$\dot{R}_{\text{in}} = \frac{\mathbf{j}_{\text{tot}}^{\text{III}}}{\phi_{\text{tot}}^{\text{in}} - \phi_{\text{tot}}^{\text{I}}} \hat{n}_r \,, \tag{4.27a}$$

$$\dot{R}_{\text{out}} = \frac{\mathbf{j}_{\text{tot}}^{\text{III}}}{\phi_{\text{tot}}^{\text{out}} - \phi_{\text{tot}}^{\text{II}}} \hat{n}_r \,. \tag{4.27b}$$

The last pair of equations allows slaving the velocities at the two interfaces:

$$\dot{R}_{\text{out}} = \dot{R}_{\text{in}} \frac{\phi_{\text{tot}}^{\text{in}} - \phi_{\text{tot}}^{\text{I}}}{\phi_{\text{tot}}^{\text{out}} - \phi_{\text{tot}}^{\text{II}}} \,, \tag{4.28}$$

implying that if an interface velocity vanishes so does the velocity of the other interface.

To determine the steady state radii (R_{in} and R_{out}) and volume fraction profiles at interfaces (ϕ_i^{I}, ϕ_i^{in}, ϕ_i^{out}, ϕ_i^{II}, the outer interface position , for $i = A, B$), we solve the set of equations in Eqs. (4.25), supplemented with

$$\dot{R}_{\text{in}} = 0 \,. \tag{4.29}$$

As outlined above (see Eq. (4.28)), the last equation implies that both interface velocities simultaneously vanish.

An example of interface kinetics is reported in Fig. 4.3. For different values of R_{in}, we solve the set of equations in (4.25) to get the corresponding outer interface positions R_{out}, the volume fractions at both interfaces and the interface velocities, $\dot{R}_{\text{in}}$ and $\dot{R}_{\text{out}}$, respectively. In Fig. 4.3 a), we show $\dot{R}_{\text{in}}$ and $\dot{R}_{\text{out}}$ as a function of $\dot{R}_{\text{in}}$. We measure velocities in units of

$$v_D = D^{\text{II}} / R_{\text{sys}} \,. \tag{4.30}$$

The system admits two stationary radii (black dots) for which both velocities simultaneously vanish. The one at lower R_{in}, with the (u) label, is unstable while at higher R_{in} we find the stable one, labelled with (s). In Fig. 4.3 b), we depict the evolution of both radii in time, initialising the system with R_{in} slightly higher than the unstable value. After both radii increase, they saturate to the steady state value corresponding to the stable point, see (s) black dot in Fig. 4.3 a). In panel c), we show the stationary state volume fraction profiles, highlighting ϕ_A and ϕ_B in blue and red, respectively. Solid lines and dashed lines correspond to the stable and unstable stationary states, black dots labeled as (s) and (u) in Fig. 4.3 a), respectively.

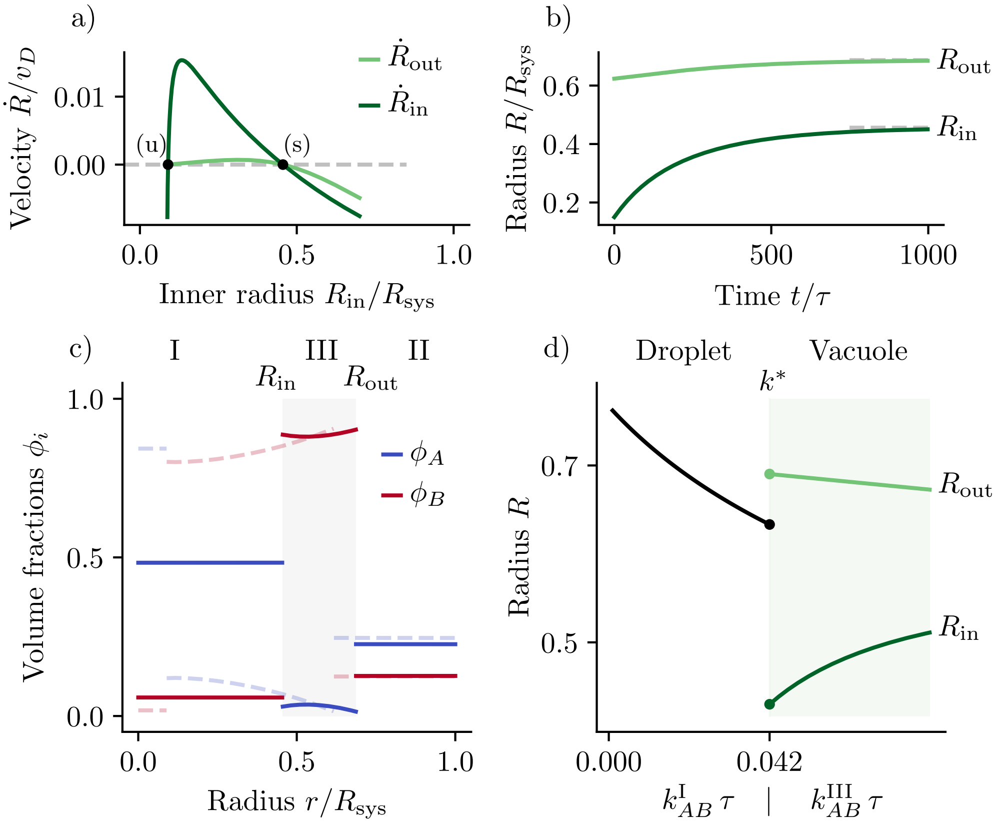

FIGURE 4.3: **Fuel-sustained chemical reactions can lead to the emergence of stationary vacuoles**. a) Interface velocities as a function of the inner radius position derived solving Eqs. (4.25). We find two stationary points (black dots) at which both velocities simultaneously vanish. The one corresponding to lower R_{in}, labelled with (u), is unstable while the one at higher R_{in}, , labelled with (s), is stable. b) Time evolution of both R_{in} and R_{out}, starting from an initial condition in the vicinity of the unstable point. Indeed the radii approach the stationary values corresponding to the stable point (s) highlighted in panel a). c) Stationary profiles of the volume fraction ϕ_A (in blue) and ϕ_B (in red) in the three phases I, II, and III. Solid and dashed lines correspond respectively to the stable and unstable stationary solutions discussed in a). In d) we discuss the different stationary states reached as a function of the B to A rate k_{BA} in the phase with higher ϕ_{tot}. For low rates, the system can be described by a single interface between a ϕ_{tot}-dense (I) and a ϕ_{tot}-dilute (II) phase. The position of the interface R, separating phases I and II, depends on k^{I}_{AB}, as already shown in Fig. 4.2 e). At $k^{\text{I}}_{AB} = k^*$, the volume fractions at the droplet centre cross the spinodal. Above k^*, the state stable is a vacuole composed of three phases I, II (the one with higher ϕ_{tot}), and III. In this regime, green shaded area, we plot the dependence of the two interface positions (R_{in} and R_{out}) on k^{III}_{AB}.

The shaded area between the two stable interface positions indicates phase III, the ϕ_{tot}-rich shell. Fig. 4.3 d) is an extension of Fig. 4.3 e), where we quantify the effect of the rate $k_B A$ in the phase with higher ϕ_{tot}. For low rates, the system can be described by a single interface between a ϕ_{tot}-dense and a ϕ_{tot}-dilute phase, which we label phase I and II, respectively. The interface position R, as well as the volume fraction profiles, depend on k^{I}_{AB}. For $k^{\text{I}}_{AB} = k^*$ the droplet centre crosses the binodal and the droplet state becomes unstable. Above k^*, the stable state becomes a vacuole composed of three phases I, II (the one with higher ϕ_{tot}), and III. In this regime, we plot the dependence of the two interface positions (R_{in} and R_{out}) on k^{III}_{AB} see the green shaded area in Fig. 4.3 d).

4.3 Theory of active vacuole compared with experiments using chemically-active coacervates

4.3.1 Experimental system using active coacervates

Recently, the Boekhoven lab has performed a set of experiments in which spherical shells, that are reminiscent of active vacuoles described in the previous chapter, were observed. Here, we shortly describe their experimental setup and compare the theory presented in Sec. 4.2 with the experimental results.

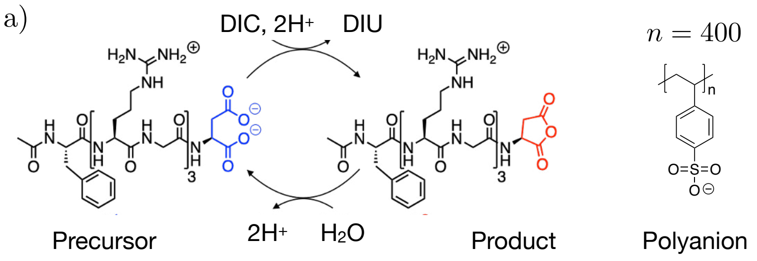

FIGURE 4.4: **Chemical reaction network underlying active coacervate formation**. The chemical reaction involves the peptide (ac-FRGRGRGD) with +1 net charge, which we refer to as "Precursor" in the following. The peptide can react with the chemical fuel, N,N'-diisopropylcarbodiimide (DIC), to form the corresponding anhydride with +3 net charge, which we call "Product". The reaction byproduct, DIU, will be referred to as "waste". In dilute solutions without fuel, the product is unstable and rapidly hydrolyzes to convert back to the precursor. At these conditions, the half-life of the product can be estimated to be roughly 45 seconds. Both precursor and product can interact with a polyanion, the poly sodium styrene sulfonate (PSS), which has a net charge of -400, on average.

In Fig. 4.4, we present the chemical reaction network, that involves a peptide, namely ac-FRGRGRGD (where F stands for phenylalanine, R for arginine, G for glycine, and D for aspartic acid) that is made of three $+1$ charged groups and a group with -2 charge. This peptide will be referred to as the "Precursor" molecule. The precursor can react with the chemical fuel, namely the N,N'-diisopropylcarbodiimide (DIC), to form the corresponding anhydride that has only the three positively charged groups. The anhydride will be referred to as the "Product" molecule. The product can also hydrolyze to revert to the precursor. In dilute conditions, the equilibrium of the first chemical reaction is shifted towards the product and the second towards the precursor. As a consequence, once the fuel is supplied, it rapidly reacts with a precursor producing product molecules, that then decay back into the precursor. The estimated half-life of the product is roughly 45 seconds. Both precursor and product can interact with a polyanion, the poly sodium styrene sulfonate (PSS), made of negatively charged units. The average number of units is $n = 400$, thus polyanion polymers have a net charge of -400, on average.

4.3.2 Phase diagram for coacervates

$\bar{c}$ [mM]			c^{I} [mM]			c^{II} [mM]		
Pre	Pro*	Pm	Pre	Pro*	Pm	Pre	Pro*	Pm
20	0	5	2500 ± 907	0	403 ± 227	5.76 ± 0.66	0	2.7 ± 0.4
9	1	5	1443 ± 403	231 ± 56	606 ± 205	3.2 ± 0.3	0.08 ± 0.03	2.6 ± 0.2
0	2	5	0	700 ± 434	1486 ± 227	0	0.78 ± 0.08	2.4 ± 0.0

TABLE 4.1: Concentrations measured in mM of precursor (Pre), stabilised product (Pro*), and polyanion monomer (Pm), in vacuole forming systems. The first group of columns contains concentrations averaged over the entire system volume. The second group of columns contains concentrations inside the coacervates (phase I), while the last group contains concentrations in the supernatant (phase II).

In a passive binary mixture composed of precursor and polyanion only, the experimental quantification of phase behavior is straightforward. However, determining the complete phase diagram for a system that also contains the product components is challenging due to the rapid hydrolyzation of the product. To circumvent this problem, the product was stabilised against hydrolysis by mutating the C terminal aspartic acid for an asparagine. This chemical modification yields a peptide that is stable and should have similar interaction propensities as the product. For sufficiently high concentrations of precursor and stabilised product, the formation of stable coacervates was observed. In Table 4.1, we display the concentrations of precursor (Pre), stabilised product (Pro*), and polyanion monomers. We chose to show the concentrations of polyanion monomers and not of the entire polyanion chains, to compare the number of similarly charged compounds. We show concentrations averaged over the entire system volume but also inside and outside the coacervate (phase I and II, respectively).

Here we aim at a minimal description of this experimental system. To this end, we consider the case where all the precursor and product molecules cluster around polyanion monomers being in excess. We identify the precursor and product belonging to these complexes as the effective components A and B. In Fig. 4.4 a), we show a sketch of the precursor, the stabilised product, and polyanion, while in panel b), we illustrate the effective components A and B. We further assume that coacervates are made of A and B only and that the excess polyanion monomers which are not surrounded by precursor or product are localised in the remaining supernatant phase [1]. These assumptions allow us to reduce the number of degrees of freedom and describe the system as an effective ternary mixture composed of A, B plus the

---

[1] We can confirm this hypothesis by calculating the number of precursors and products per polyanion monomer $p_A = c^{\mathrm{I}}_{\mathrm{Pm}}/c^{\mathrm{I}}_{\mathrm{Pre}}$, in the system composed of precursor and polyanion only, focusing on

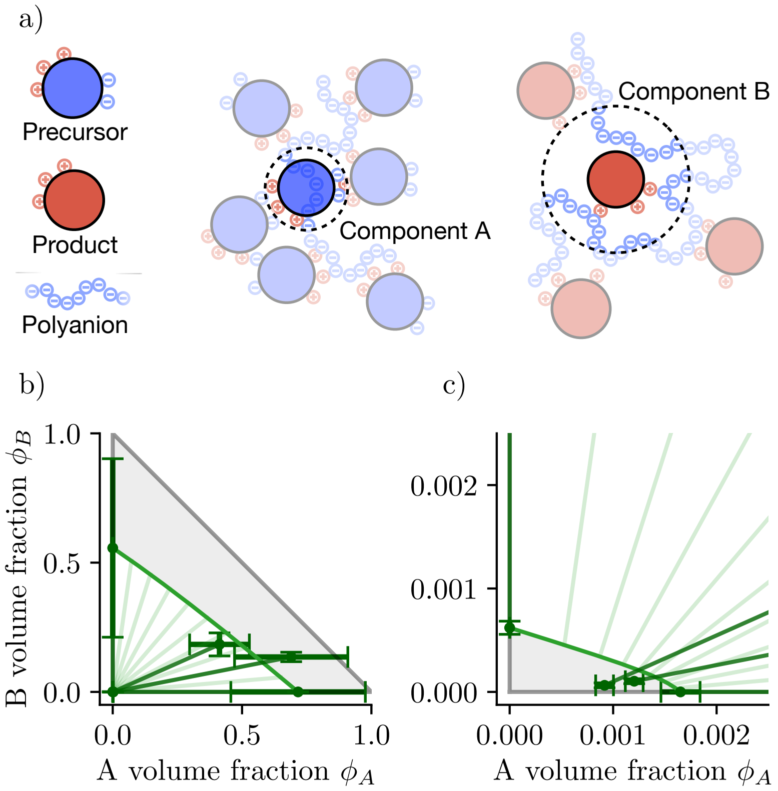

FIGURE 4.5: **Phase behaviour of effective components A and B.** a) Sketch of the precursor, product, and polyanion, that get combined to form the effective components shown to the right of panel a). In particular, component A is formed by a precursor molecule plus a strand belonging to the polyanion. Component B is composed of a precursor molecule surrounded by pieces of polyanion strands. Counterions that make the system neutral are not shown. b) and c) depict the phase diagram for the two-component A and B. Data points from experiments performed in the Boekhoven lab (TUM) are shown in green (including error bars related to the HPLC concentration measurement). Theoretical fits using a ternary Flory Huggins model are shown by green solid lines. Gray-shaded domains correspond to the mixed domains based on the theoretical fits.

solvent, in which we include water, buffer, and the polyanion monomers in excess. Furthermore, the concentrations of A and B are easy to calculate, since they are in 1-1 correspondence with the precursor and stabilised product concentrations. The Flory Huggins free energy (see Eq. (2.3)) that best fits the experimental values corresponds to the relative molecular volumes

$$\nu_A = 15.9\,, \quad \nu_B = 44.2\,, \tag{4.31}$$

and the interaction propensities

$$\chi_{A0} = 1.15\, k_BT\,, \quad \chi_{B0} = 0.869\, k_BT\,, \quad \chi_{AB} = -0.025\, k_BT\,. \tag{4.32}$$

---

the inside phase (first raw of Table 4.1). The same can be done in the system with the stabilised product only, to get p_B. We can now focus on the case in which both precursor and product are present, and calculate the expected amount of polyanion in the coacervate phase, assuming that p_A and p_B are constant. The estimation yields $c^{\mathrm{I}}_{\mathrm{Pm}} = 715$, which agrees with the measured value 606 ± 205.

The difference in relative molecular volumes can be explained considering that in the effective component B, a product molecule is surrounded by more polyanion monomers, as represented in Fig. 4.4 b). This is consistent with the data presented in Table 4.1. Once the relative molecular volumes are known, we can convert concentrations to volume fractions and construct the binary phase diagram as a function of the volume fractions ϕ_A and ϕ_B, see Fig. 4.4 c).

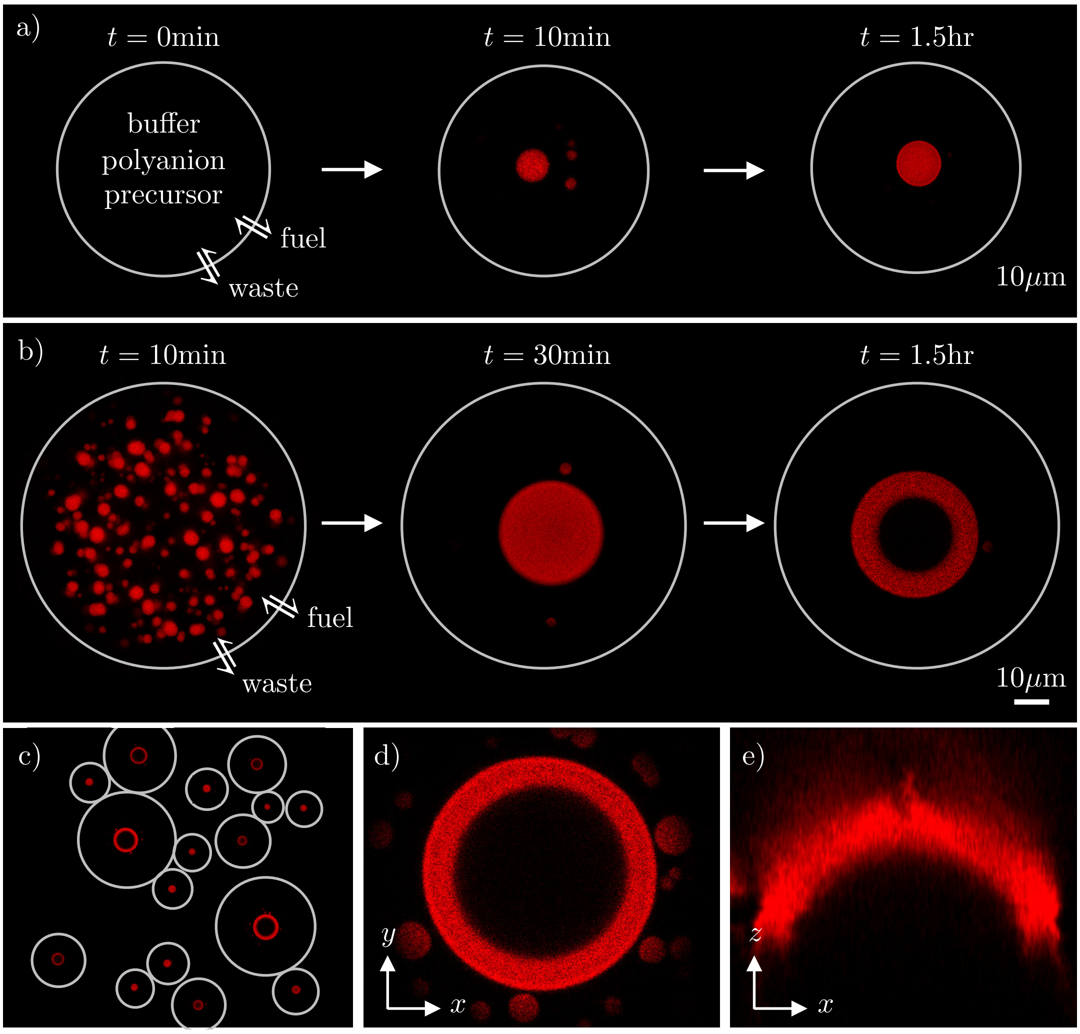

FIGURE 4.6: **Experimental realization of spherical shells with fuel-activated coacervates**. a) Microfluidic reactor composed of a water droplet loaded with buffer, polyanion, and precursor, in contact with an oil phase containing fuel. After a rapid transient, the fuel concentration in the water phase can be considered constant $c_F = 18$mM. Due to the fuel-mediated production of the product, droplets nucleate and start to fuse until a stationary state composed of a single drop is reached. b) In larger microreactors the single drop state, reached after approximately 30min, is not stable. After sinking to the bottom of the microreactor, it becomes a spherical shell of uniform thickness. c) Snapshot of many reactors with different sizes, the bigger ones containing spherical shells. d) top and e) lateral view of a spherical shell sitting at the interface between the water droplet and oil phase.

4.3.3 Vacuole formation in coacervate systems coupled to a fuel reservoir

In the last chapter, we have studied the phase equilibrium of the system corresponding to a fixed product and precursor amount in the absence of fuel. In this case, the product component was stable due to a chemical modification. We introduced a minimal description in terms of A and B effective components and used the experimental data to shed light on their size and interaction propensities. In this section, we now study the kinetics of the original system where the composition of A and B is regulated by the fuel-driven chemical reaction network introduced in Fig. 4.4. Experimentally, the fuel is provided by a reservoir. In particular, a microreactor-like setup was used by preparing a stable emulsion of water droplets in a fluorinated oil phase, as shown in Fig. 4.6 a), first panel. The water droplets (enclosed by a white circle) contain buffer, polyanion, and precursor, but initially no fuel. At $t = 0$, 500 mM of fuel was injected into the oil phase. The fuel rapidly diffuses into the droplets where it reacts with the precursor. Since the solubility of fuel in water is 18 mM and thereby much lower than the amount of fuel in the oil phase, and its diffusion is very quick, we consider the fuel concentration in the water phase constant $c_\mathrm{F} = 18\mathrm{mM}$. Importantly, the reaction waste (DIU) crystallises in the oil phase. Therefore, this method allows us to continuously maintain a steady fuel concentration and simultaneously avoid the challenges typically encountered with waste accumulation. Within seconds after preparing the microreactors, the coacervate droplets nucleate and start to fuse.

We find that the long-time behaviour depends on the size of the microreactor. In small microreactors, Fig. 4.6 a), the droplets coalesce until a stationary state composed of a single drop is reached. We observe the formation of a single drop also in larger microreactors, see Fig. 4.6 b), but this final drop is not stable. After about 30 minutes, it sinks to the bottom of the microreactor, and its core dissolves, giving rise to a spherical shell of uniform thickness. The spherical shell remains stable for at least 12 hours and thus can be considered a stationary state. Studying its fluorescence recovery after photobleaching, showed that the shell is liquid. Once the fuel concentration was lowered in the system, e.g., by diluting the fluorinated oil, the amount of product decreases and the spherical shell gradually collapses until the system become homogeneous (data not shown). In Fig. 4.6 c), we show many polydispersed reactors, the bigger ones containing spherical shells. In Fig. 4.6 d) and e), we show a top and lateral view of a spherical shell. Note that, at the interface between the water droplet and oil phase, the wetting angle is approximately 90°.

4.3.4 Recapitulating experimental findings with the effective droplet model

We now use the theory outlined in Sec. 4.2 to characterise the steady state of the system and benchmark the experimental findings. We resort to the simplified theory that considers combinations of precursor, product, and polyanion strands leading to the effective components A and B, introduced in Sec. 4.3.2. The starting point of this theory is the free energy density f, see Eq. (2.3). We neglect all other chemical species and consider the fuel maintained at a constant concentration. The thermodynamic parameters contained in f, namely the molecular volume ratios and the interaction propensities, were obtained in Sec. 4.3.2 by fitting the experimental phase diagram, see Eq. (4.32) and Eq. (4.31). The drawback of using effective components with different molecular volumes is that the chemical reaction between 1 precursor and 1 product gets translated into

$$\nu_B A \rightleftharpoons \nu_A B \,. \tag{4.33}$$

In fact, this choice of stoichiometric coefficients leads to a volume-conserving reaction.

The last thermodynamic parameter that the theory requires is surface tension. Since a direct measure in the microreactors is not feasible, we use a value

$$\gamma = 50\mu\mathrm{N}/\mathrm{m}^2 \,, \tag{4.34}$$

which is in agreement with the literature on complex coacervation [53]. The missing parameters entering the linearised equations (4.12) are the diffusion coefficients and the reaction rates. As anticipated, we neglect their dependence on composition and use for the effective components A and B the experimental estimates for the product and precursor diffusivities, namely

$$D_A^{\mathrm{I}} = D_B^{\mathrm{I}} = 0.03\mu\mathrm{m}^2/s \,, \quad D_A^{\mathrm{II}} = D_B^{\mathrm{II}} = 10\mu\mathrm{m}^2/s \,. \tag{4.35}$$

Getting an estimate for the chemical rates associated with the effective components is not an easy task, given the difference between the chemical reaction in Eq. (4.33) and the one involving the same amount of product and the precursor, shown in Fig. 4.4. For the reaction from B to A we use the experimental value measured for the product hydrolyzation, namely,

$$k_{AB}^{\mathrm{I}} = k_{AB}^{\mathrm{II}} = 0.015 s^{-1} \,. \tag{4.36}$$

The rate of precursor activation k_{act} is fuel-dependent, as is clear from Fig. 4.4. We assume the fuel concentration in the supernatant phase to be set by the solubility of fuel in water $c_{\mathrm{F}}^{\mathrm{II}} = 18\mathrm{mM}$. This value, together with the experimental estimate $k_{\mathrm{act}} = c_{\mathrm{F}}\, 0.1 s^{-1}$, allows to get

$$k_{\mathrm{act}}^{\mathrm{II}} = 0.002 s^{-1} \,. \tag{4.37}$$

Unfortunately, the amount of fuel in the vacuole phase is impossible to measure, leaving us without knowledge of the precursor activation rate in phase I, $k_{\mathrm{act}}^{\mathrm{I}}$. Good agreement with the experimental results is found setting

$$k_{\text{BA}}^{\text{II}} = 0.0016s^{-1}\,, \quad k_{\text{BA}}^{\text{I}} = 0.00016s^{-1}\,. \tag{4.38}$$

Both values are not too far from the experimental estimate for the rate of precursor conversion into the product. We are finally ready to apply the theory developed in Sec. 4.2 to describe the transition from stable droplets to stable vacuoles. We first look for stationary profiles corresponding to a single interface, solving the set of equations in (4.18). In Fig. 4.7, we plot two representative radial volume fraction profiles corresponding to a) small reactors ($R_{\text{sys}} = 15\mu\text{m}$) and b) big reactors ($R_{\text{sys}} = 30\mu\text{m}$). As the system size increases, the volume fractions ϕ_A and ϕ_B (in blue and red, respectively) in the centre of the coacervate phase (shaded area) deviate significantly from their values at the coacervate interface R. The changes in volume fraction when moving from the coacervate boundary R, indicated by dots in a), to the coacervate centre at $r = 0$ are indicated with the triangular arrowhead, as well as plotted in the phase diagram in Fig. 4.7 c). In the case of big microreactors, as in b), the coacervate centre crosses the spinodal and the droplet state becomes unstable. The stable state for these large values of R_{sys} can be described by solving the Eqs. (4.25), corresponding to two interfaces. The stationary radial profile corresponding to $R_{\text{sys}} = 30$ is shown in Fig. 4.7 d). In this figure, the ϕ_{tot}-rich shell is shaded in gray. Unfortunately, experimentally, the spatial profiles of precursor and product are currently not available preventing comparison with the theoretical profiles. Instead, the dependence of the stable droplet radius on the microreactor volume and the onset of the vacuole formation could be determined experimentally. These results are shown in Fig. 4.7 e) (orange dots), together with the dependence of the inner and outer radius on reactor volume above the onset of the vacuole formation (blue dots). For comparison, the orange and blue lines show the same quantities calculated within the theory developed in Sec. 4.2.

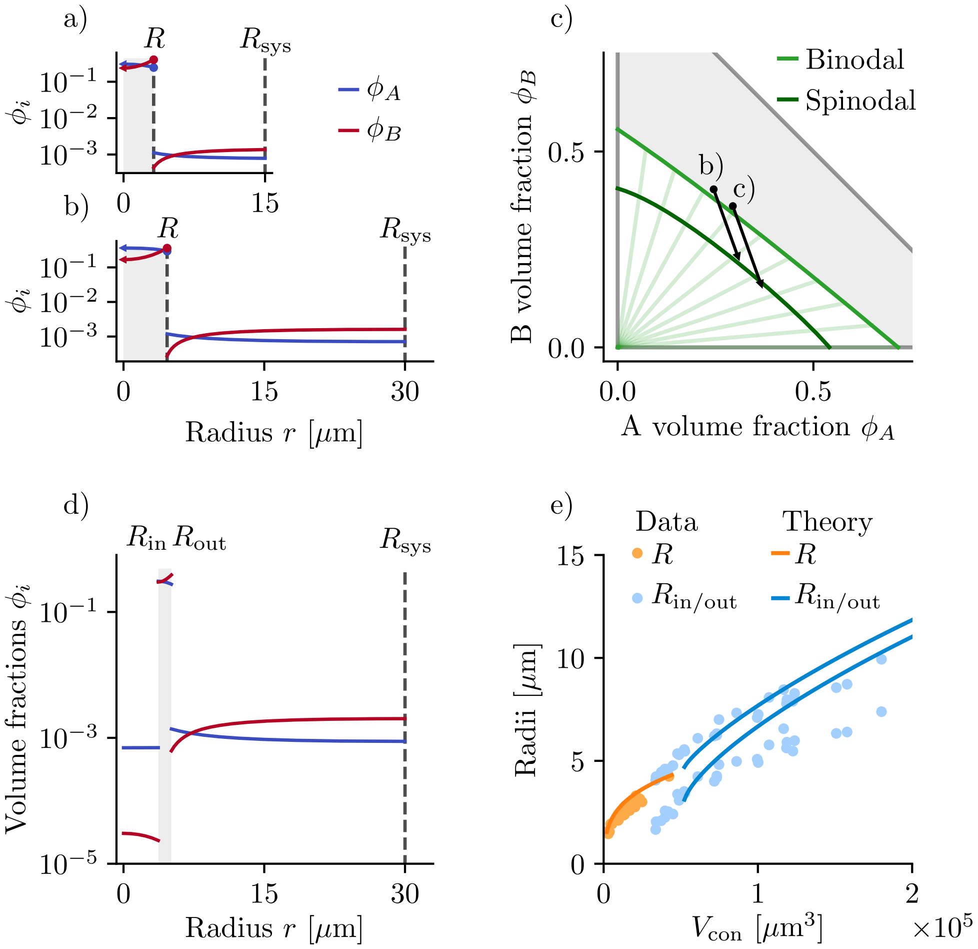

FIGURE 4.7: **Theoretical description of active coacervate vacuoles agrees with the experimental results**. Radial volume fraction profiles representative of a) small reactors ($R_{\text{sys}} = 15\mu\text{m}$). and b) big reactors ($R_{\text{sys}} = 30\mu\text{m}$). For large reactor sizes, ϕ_A and ϕ_B (in blue and red, respectively) at the coacervate interface $r = R$ (dots) differ significantly from the values in the centre of the coacervate phase $r = 0$ (triangles). c) The discrepancy between the coacervate boundary R, indicated with dots, and the coacervate center, indicated with the triangle at the arrow tip, are plotted in the phase diagram. We show the variations corresponding to small and large microreactors, with system sizes corresponding to a) and b), respectively. For reactors bigger than a threshold, the coacervate centre crosses the spinodal and the droplet state becomes unstable. d) The stationary radial profile for $R_{\text{sys}} = 30$, representative of large reactor sizes. The shaded area corresponds to the ϕ_{tot}-rich spherical shell. In panel e), we locate the reactor size threshold corresponding to the emergence of vacuoles. Orange dots display experimentally measured droplet radius for different microreactor volumes, while blue ones the variation of inner and outer radius measured as a function of the reactor volume, after the onset of vacuoles. The same quantities derived from the theoretical analysis are depicted with the orange and blue lines, showing good agreement with the experimental data.

Chapter 5

Controlling phase composition in the limit of a large number of components

In the previous chapters, we discussed how to study the composition of coexisting phases in the presence of chemical reactions. Controlling the composition of coexisting phases becomes crucial when the number of components in a mixture and the number of reactions among them rise. In this chapter, we use chemical reaction networks to describe proteins that, in addition to driving phase separation, can assemble and form aggregates of different sizes. This model is motivated by the observation that many biologically relevant proteins form clusters, that can collectively phase separate from the solvent [54, 55]. The interplay between phase separation and protein aggregation becomes particularly interesting in the limit of infinite maximum aggregate size. This work is done in collaboration with Thomas Michaels and Christoph Weber. The illustrations shown in this chapter are made with *Biorender.com*

5.1 Equilibrium theory of aggregation and phase separation

5.1.1 A chemical reaction network to describe aggregation

Here, we apply the theory developed in chapter 2 to that case in which the M components are different aggregation states of the same molecule, resulting from the formation of internal bonds. In particular, component C_1 represents the monomeric form, C_2 the dimer, etc etc. We focus on monomers with the same molecular volume of the solvent, $v_1 = v_0$ leading to a scaling of the relative molecular volumes of the form $\nu_i = i$. Aggregates can convert into each other via monomer pick-up, described through the set of $M-1$ chemical reactions

$$C_1 + C_i \rightleftharpoons C_{i+1} \,. \tag{5.1}$$

This reaction network is exemplified in Fig. 5.1 a), and its associated stoichiometric matrix σ_{ia}, defined in Eq. (2.14), reads

$$\sigma = \begin{array}{c} \begin{array}{ccccc} a=1 & a=2 & a=3 & \dots & a=M-1 \end{array} \\ \left(\begin{array}{ccccc} -2 & -1 & -1 & \dots & -1 \\ +1 & -1 & 0 & \dots & 0 \\ 0 & +1 & -1 & \dots & 0 \\ \vdots & \vdots & \vdots & \ddots & \vdots \\ 0 & 0 & 0 & \dots & -1 \\ 0 & 0 & 0 & \dots & +1 \end{array}\right) \begin{array}{l} C_1 \\ C_2 \\ C_3 \\ \vdots \\ C_{M-1} \\ C_M \end{array} \end{array} \,. \tag{5.2}$$

We chose the conserved quantity

$$\phi_{\text{tot}} = \sum_{i=1}^{M} \phi_i \,, \tag{5.3}$$

which represents the total volume fraction occupied by the macromolecule in all possible aggregation states. The reaction extents, defined in Eq. (2.18), can be chosen to be

$$\xi_a = \sum_{i=a+1}^{M} \frac{\phi_i}{i} \,. \tag{5.4}$$

In a homogeneous mixture, ξ_a can be related to the progress of the chemical reactions, starting from an initial state composed of monomers only.

5.1.2 Scaling laws in the multicomponent aggregation free energy

Recalling the form of the free energy density in Eq. (2.3), the key parameters of this model are the internal free energy of aggregates, ω_i, and the interaction energies of aggregates among themselves and with the solvent, χ_{ij}. We begin discussing a scaling form for ω_i, with the cluster size i. We recall that the internal free energies can be interpreted as the free energy cost of producing i-th components. Discussing aggregating particles, this descends from the formation of internal bonds, that keep a cluster of size i together. For this reason, we introduce the number of oligomerization domains per monomer, z. The total number of bonds formed in an aggregate of size i receives contributions coming from monomers at the boundaries of the cluster, which are i_b), and the bulk ones, $i - i_\text{b}$. Monomers in the bulk can saturate all their z oligomerization domains while, in general, monomers at the boundaries are able to saturate only $z_\text{b} < z$ of them, for steric reasons. Summing up, we get

$$\omega_i = \frac{z(i - i_\text{b}) + z_\text{b} i_\text{b}}{2i}\,\Delta\omega = \frac{z}{2}\,\Delta\omega - (z - z_\text{b})\frac{i_\text{b}}{2i}\,\Delta\omega\,, \tag{5.5}$$

where $\Delta\omega$ is the free energy associated with the formation of a single bond, and the factor 2 avoids double counting.

We introduce three species of aggregates with different spatial dimensions: rod-like (d=1), disc-like (d=2) and spherical (d=3), see Fig. 5.1 b). These can be realised by varying the number of oligomerization domains and their orientation. Rod-like aggregates (d=1) are defined to have only two oligomerization domains with a fixed orientation. They can be pictured as one-dimensional aggregates with no loops, leading to $i_\text{b} = 2, z = 2, z_\text{b} = 1$. Disk-like aggregates (d=2) are defined to have $z > 2$ coplanar oligomerization domains. For disks, the total number of monomers and the number of boundary monomers scale respectively with the area and the perimeter of the aggregate. As a consequence, in $d = 2$, $i_\text{b} \simeq \sqrt{i}$. Spherical aggregates (d=3) are characterized by $z > 2$ oligomerization domains with no precise orientation. In this case, the total number of monomers and the number of monomers at the boundary scale with the volume and the area, respectively, leading to $i_\text{b} \simeq i^{2/3}$. Inserting there the relations for i_b in Eq (5.5) leads to the following scaling relationships for the internal free energies of rod-like ($d = 1$), disk-like ($d = 2$) and spherical ($d = 3$):

$$\omega_i \simeq \omega_\infty + \frac{\Delta\omega}{i^{1/d}}\,. \tag{5.6}$$

Here, $\omega_\infty = \lim_{i\to\infty}\omega_i$ is a constant that does not affect both chemical and phase equilibrium. In the bond free energy $\Delta\omega$, we include an enthalpic and entropic contribution

$$\Delta\omega = e_\text{int} - s_\text{int}T\,. \tag{5.7}$$

For the scaling of interaction energies, we focus on the case

$$\chi_{ij} = 0 \text{ for } i, j > 0\,, \qquad \chi_{i0} = \chi\,. \tag{5.8}$$

Inserting both scaling ansatzes in the Florry Huggins free energy density defined in Eq. (2.3), we get

$$\begin{aligned} f = \frac{\omega_\infty}{v_0}\phi_{\text{tot}} + \frac{k_B T}{v_0}\Bigg[\sum_{i=1}^{M}\frac{\phi_i}{i}\ln\frac{\phi_i}{i} + \frac{\Delta\omega}{k_B T}\frac{\phi_i}{i^{1/d}} + \\ + (1-\phi_{\text{tot}})\ln(1-\phi_{\text{tot}}) + \frac{\chi}{k_B T}\,\phi_{\text{tot}}\,(1-\phi_{\text{tot}})\Bigg]\,, \end{aligned} \tag{5.9}$$

with $\Delta\omega$ defined in Eq. (5.7) Examining the free energy above, we notice that our choice of interaction parameters led to an interaction term that depends only on the total amount of macromolecule ϕ_{tot}. This corresponds to the case in which monomers have the same interaction propensities independently of the aggregate they belong.

5.1.3 Chemical equilibrium in homogeneous systems

We start by using the free energy in Eq. (5.9) to study aggregation equilibrium in a homogeneous system. According to Eq. (2.28), the monomer transitions between clusters are at equilibrium if

$$\frac{\bar{\mu}_i}{i} = \bar{\mu}_1 = \text{const.} \quad \forall\, i = 2 \ldots M\,, \tag{5.10}$$

where $\bar{\mu}_i$ is the i-th exchange chemical potential defined in Eq. (2.5). Using the free energy of Eq.(5.9) in Eq. (5.10) leads to the following expression for the volume fraction of the cluster of size i as a function of the monomer volume fraction ϕ_1:

$$\phi_i = i\,\phi_1^i\,\exp\left(-i\,\frac{\omega_i-\omega_1}{k_B T} + i - 1\right)\,, \tag{5.11}$$

$$= i\left(\frac{\phi_1}{\phi^*}\right)^i \exp\left(\frac{\Delta\omega}{k_B T}\,i^{\frac{d-1}{d}} - 1\right)\,, \tag{5.12}$$

where we have used the internal free energy (5.6) and introduced the volume fraction threshold, $\phi^* = \exp(\Delta\omega/k_B T - 1)$. As we will discuss in the following, ϕ^* represents the ϕ_{tot} value corresponding to the emergence of large clusters. Note that, due to our choice of interaction scaling (Eq. (5.8)), the value of χ does not influence chemical equilibrium. The equation above together with conservation of monomers (5.3), allows us to calculate the volume fraction of each aggregate of size i, $\phi_i(\phi_{\text{tot}})$, as a function of the conserved quantity ϕ_{tot}.

In Fig. 5.1, we show the cluster size distribution in homogeneous mixtures obtained by solving numerically Eq. (5.11) together with Eq. (5.3), with a cut-off $M = 50$. As anticipated, for dilute solutions corresponding to $\phi_{\text{tot}} \ll \phi^*$, the size distribution is

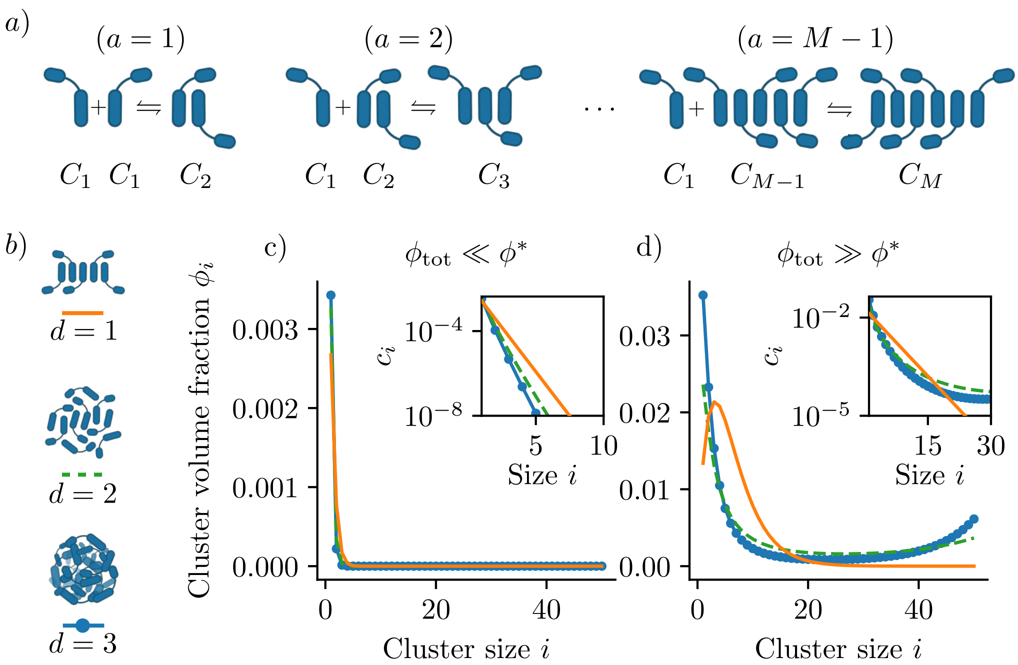

FIGURE 5.1: **A volume fraction threshold separates two aggregation regimes in homogeneous systems**. a) Chemical reaction network associated with monomer aggregation. b) Illustration of aggregates of different spatial dimensions. c) Cluster size distribution for $M = 50$, at low total macromolecular volume fraction: $\phi_{\text{tot}} \ll \phi^*$. Irrespective of aggregate dimension, d, the macromolecules are mainly in the monomer state, i.e., $\phi_1 \simeq \phi_{\text{tot}}$. d) For $\phi_{\text{tot}} \gg \phi^*$, the monomer concentration saturates at $\phi_1 \simeq \phi^*$ and large clusters begin to populate the system. For rod-like aggregates (corresponding to $d = 1$ in (5.6)), the distribution becomes peaked at an intermediate value $i_{\text{max}} > 1$ and then exponentially cut off. For disk-like and spherical aggregates, $d = 2, 3$, the distribution becomes bimodal, with peaks at $i = 1$ and $i = M$, the maximum cluster size ($M = 50$). This bimodal behaviour hints at the emergence of a gelation transition in the limit $M \to \infty$. In the insets, we show aggregate concentrations $c_i = \phi_i/i$, measured in units of $1/v_0$, and their scaling with the aggregate size.

dominated by monomers while larger aggregates have vanishing volume fraction, i.e., $\phi_1 \simeq \phi_{\text{tot}}$. For $\phi_{\text{tot}} \gg \phi^*$, the monomer concentration saturates at $\phi_1 \simeq \phi^*$ and aggregates begin to populate the system. Above this threshold, the size distribution depends crucially on cluster dimensionality d. For rod-like aggregates, $d = 1$ in (5.6), the distribution becomes peaked at a value $M > 1$ and then exponentially cut off. For disk-like and spherical aggregates, $d = 2, 3$ in (5.6), the distribution becomes bimodal peaked at $i = 1$ and at $i = M$, the maximum cluster size ($M = 50$ in Fig. 5.1). The emergence of this threshold and the behaviour of the system at high density can be exemplified in the case of rod-like aggregates (d=1), in the limit $M \to \infty$, see App. C. There we find an explicit form for the volume fraction distribution $\phi_i = \phi_i(\phi_{\text{tot}})$ and we show that, at $\phi_{\text{tot}} = \phi^*$, the cluster size corresponding to the maximum of this distribution (i_{max}) becomes greater than 1.

For $d = 2, 3$ the bimodal behaviour observed at $\phi_{\text{tot}} \sim \phi^*$ for $M = 50$ suggests that, in the limit $M \to \infty$, the system undergoes a gelation transition. This transition is defined as the emergence of an aggregate that is comparable with the system size [56, 57]. In App D we discuss a criterion to confirm that indeed gelation occurs for $\phi_{\text{tot}} \sim \phi^*$. To precisely locate this transition point and describe what happens above the transition, we have to relax the assumption that the system is homogeneous. In the next section, we are going to describe systems that can spatially compartmentalise as the result of phase separation, applying the theory presented in Sec. 2.1.

5.1.4 Phase and thermodynamic equilibrium

As discussed in Chapter 2, n_{p} phases are at equilibrium in an incompressible, multicomponent if the exchange chemical potentials $\bar{\mu}_i$ (defined in Eq. (2.5)) and the osmotic pressure (Eq. (2.7)) balance in each phase:

$$\bar{\mu}_i\big(\{\phi_j^{\text{I}}\}\big) = \bar{\mu}_i\big(\{\phi_j^{\alpha}\}\big) \,, \tag{5.13}$$

$$\Pi\big(\{\phi_i^{\text{I}}\}\big) = \Pi\big(\{\phi_i^{\alpha}\}\big) \,, \tag{5.14}$$

where the index α runs over all phases different from I, i.e. $\alpha = \text{II}, \ldots, n_{\text{p}}$. For a detailed discussion see Sec. 2.1.2. We now focus on mixtures at thermodynamic equilibrium, i.e. when aggregation and phase equilibrium hold simultaneously. As outlined in the previous section, aggregation equilibrium allows finding each volume fraction as a function of the total macromolecule amount, i.e. $\phi_i\left(\phi_{\text{tot}}\right)$ (combining Eq. (5.11) and Eq. (5.3)). The free energy density (2.3), in turn, can be written as a function of the conserved variable, ϕ_{tot}. Chemical equilibrium also restricts the maximum number of coexisting phases, see Eq. (2.31) and related discussion. In the case of aggregation, we have M solute components and $M-1$ reactions, leading to a maximum number of coexisting phases $n_{\text{p}}^* = 3$. For this reason, we restrict to two-phase coexistence and rewrite the phase equilibrium as:

$$\bar{\mu}(\phi_{\text{tot}}^{\text{I}}) = \bar{\mu}(\phi_{\text{tot}}^{\text{II}}) \,, \tag{5.15a}$$

$$\bar{\mu}(\phi_{\text{tot}}^{\text{I}}) = \frac{f(\phi_{\text{tot}}^{\text{II}}) - f(\phi_{\text{tot}}^{\text{I}})}{\phi_{\text{tot}}^{\text{II}} - \phi_{\text{tot}}^{\text{I}}} \,. \tag{5.15b}$$

To exemplify the behaviour of the system at thermodynamic equilibrium, we discuss rod-like aggregates ($d = 1$) in the limit $M \to \infty$. As shown in App. C, in this special case we can find an analytic expression for $f\left(\phi_{\text{tot}}\right)$. Due to the presence of the interaction term χ, the system can demix into two phases with different total volume fractions $\phi_{\text{tot}}^{\text{I}}$ and $\phi_{\text{tot}}^{\text{II}}$, given by Eqs.(5.15). By means of $\phi_{\text{tot}}^{\text{I/II}}$, we can reconstruct the whole assembly size distribution $\phi_i^{\text{I/II}}$ via the set of equations coming from chemical equilibrium, see Eq. (5.11) and Eq. (5.3).

We first focus on the regime where the interaction and internal energy scales are comparable $e_{\text{int}} \simeq \chi$. In Fig. 5.2 a), we show the phase diagram as a function of ϕ_{tot} and the rescaled temperature T/T_0 with $T_0 = \chi/k_B$. The domain enclosed by the binodal corresponds to phase separation while the colour code depicts the monomer fraction ϕ_1/ϕ_{tot} in each phase. The green dashed line is the volume fraction threshold

$\phi^*(T)$, at which intermediate-sized aggregates start to appear. These two curves define distinct regions in the phase diagram. In region "1" the system is homogeneous and composed of monomers only, see Fig. 5.2 b) left, while in region "2" is homogeneous but populated by larger aggregates. In region "3" the system phase separates but, in both phases, monomers dominate the size distribution, see Fig. 5.2 b) centre. The intersection with the binodal line locates the temperature below which the total aggregate volume fraction in the dilute phase lies below the threshold, $\phi_{\text{tot}}^{\text{II}} < \phi^*$, while in the dense phase lies above $\phi_{\text{tot}}^{\text{I}} > \phi^*$. As described in the previous section and Fig. 5.1, below this temperature we expect the cluster size distribution to significantly differ in the two phases. Indeed this is the case in region "4" as displayed in Fig 5.2 b) right. In Fig 5.2 b)-c) we illustrate states corresponding to fixed ϕ_{tot} and decreasing temperature T, starting from a homogeneous monomeric state, region "1", to a demixed state with the same composition, region "3", and finally to a demixed state with only monomers outside while inside larger aggregates are present, region "4". In Fig. 5.2 d)-f) we discuss the thermodynamic behaviour of linear aggregates ($d = 1$), in the regime where the internal energy is much stronger than the interaction scale $e_{\text{int}} \gg \chi$. As is clear from the phase diagram presented in Fig. 5.2 d), for a wide range of temperatures the aggregation threshold precedes in ϕ_{tot} the dilute branch of the binodal. In addition to cases already discussed above (Fig. 5.2 b)), this gives rise to region "5", where both the dilute and the dense phase are enriched in large aggregates, see Fig. 5.2 e), right panel. In Fig 5.2 f) we illustrates states corresponding to fixed T and increasing ϕ_{tot}. Starting from a homogeneous monomeric state, "1", increasing the total aggregate volume fraction ϕ_{tot} the system crosses the volume fraction threshold ϕ^*, entering region "2". Here, intermediate aggregates appear, with the maximum and the average of the distribution ϕ_i scaling with $\sqrt{\phi_{\text{tot}}}$, see Appendix C. Finally, once $\phi_{\text{tot}} > \phi_{\text{tot}}^{\text{II}}$, the system enters region "5", where it demixes in two phases both populated by intermediate aggregates.

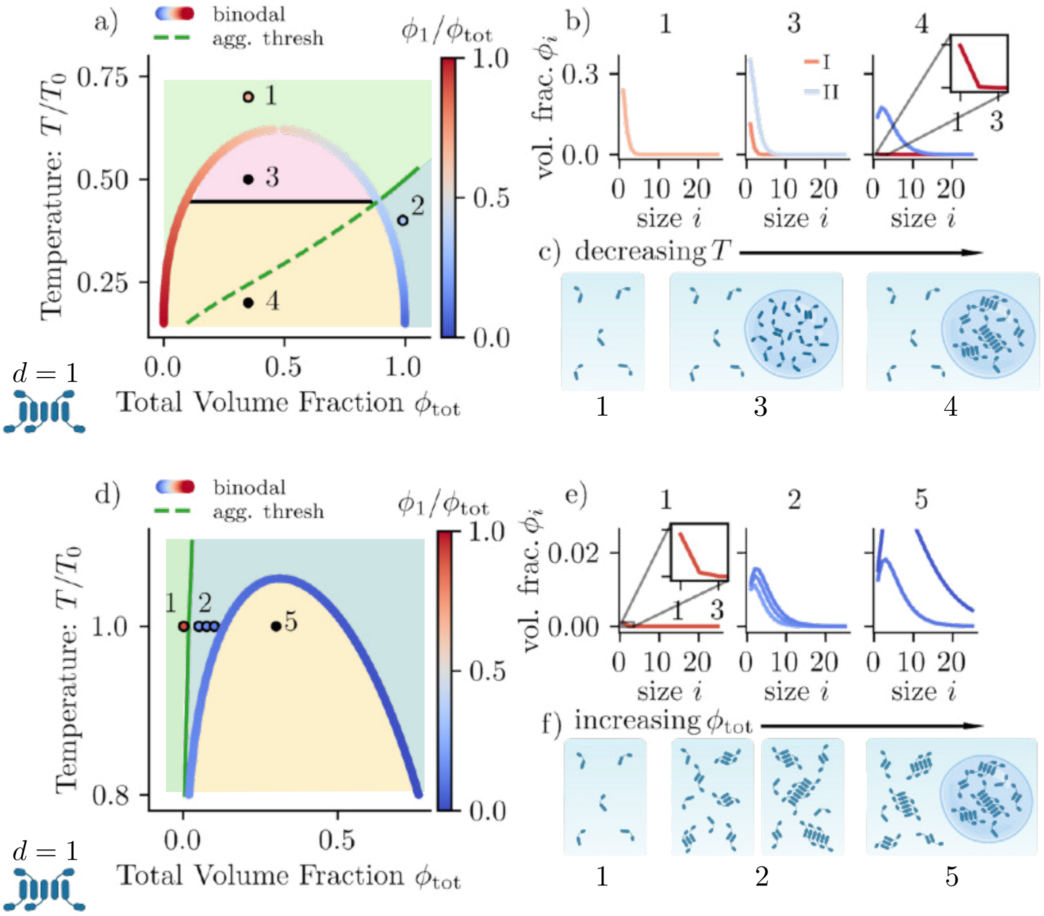

FIGURE 5.2: **Phase diagram and for rod-like aggregates aggregate in the two regimes $e_{\mathrm{int}} \sim \chi$ and $e_{\mathrm{int}} \gg \chi$.** a) Phase diagram in the regime $e_{\mathrm{int}} \simeq \chi$, as a function of ϕ_{tot} and the rescaled temperature T/T_0 with $T_0 = \chi/k_B$. The coloured curve represents the binodal, enclosing the phase separation regime, with the colour code depicting the monomer fraction $\phi_1/\phi_{\mathrm{tot}}$ in each phase. The green dashed line is the volume fraction threshold $\phi^*(T)$, at which intermediate-sized aggregates start to appear. b) Size distributions in different regions of the phase diagram, defined by the interception of the binodal with the aggregation threshold. In region "1" the system is homogeneous and composed of monomers only. In region "3" the system phase separates, but in both phases, monomers dominate the size distribution, while in region "4" the dense phase becomes populated by intermediate aggregates. Progressively lowering the temperature allows switching between these regions, as depicted in c). In d)-f) we focus on the regime where the internal energy is much stronger than the interaction scale $e_{\mathrm{int}} \gg \chi$. In phase diagram a), the aggregation threshold precedes in ϕ_{tot} the dilute branch of the binodal. In this regime, we can identify a new region, "5", characterised by intermediate aggregates in both phases. In e) we illustrate states representative of these regions, corresponding to fixed T and increasing ϕ_{tot}. Starting from a homogeneous monomeric state, "1", and increasing the total aggregate volume fraction ϕ_{tot} the system enters in region "2" where intermediate aggregates appear. Here, the sizes corresponding to the maximum and the average of the distribution ϕ_i scaling with $\sqrt{\phi_{\mathrm{tot}}}$, see Appendix C. Finally, once $\phi_{\mathrm{tot}} > \phi_{\mathrm{tot}}^{\mathrm{II}}$, the system enters region "5" and demixes in two phases, both rich in intermediate aggregates.

5.1.5 The interplay between phase separation and aggregation equilibrium

We now fix the interaction propensity χ, the temperature and T/T_0, and the total macromolecule volume fraction ϕ_{tot} to values corresponding to two-phase coexistence at thermodynamic equilibrium. We then compare the aggregate size distribution (after averaging over both phases), with the distribution in the corresponding homogeneous state, with the same values of T and ϕ_{tot}. We recall that, due to our choice of interaction propensity scaling in Eq. (5.8), the size distribution in the homogeneous system, Eq. (5.11), is insensitive to χ. For this reason, the homogeneous state can be thought of as an unstable state corresponding to the same χ as the phase separating one, which has not reached phase equilibrium yet, but also as the equilibrium state of a system with the same parameters as the phase separating one, except suppressed hydrophobicity ($\chi = 0$).

In Fig. 5.3 a), we display results for rod-like aggregates (d=1) with the same parameters as in Fig. 5.2, $T/T_0 = 0.2$, and $\phi_{\text{tot}} = 0.016$, just inside the binodal. There, we compare the size distribution in the homogeneous system ϕ_i, with the weighted average over compartments, defined as

$$\bar{\phi}_i = \frac{V^{\text{I}}}{V}\phi_i^{\text{I}} + \frac{V^{\text{II}}}{V}\phi_i^{\text{II}} , \tag{5.16}$$

in the corresponding phase-separated system. Clearly, the two distributions differ, proving that the presence of compartments can lead to larger aggregates. The difference in distributions can be quantified by means of the functional distance

$$\delta(h,g) = \sup_i \left| \frac{h_i}{\sum_i h_i} - \frac{g_i}{\sum_i g_i} \right| , \tag{5.17}$$

that quantifies the distance among two normalised functions as the largest possible distance among values that they assign to the same element. This distance is sometimes referred to as "statistical distance". The distance between the homogeneous size distribution and the distribution defined in Eq. (5.16), depends on the temperature T and the total volume fraction ϕ_{tot} chosen, which in turn determines the droplet size. In Fig. 5.2 b) we display distance differences corresponding to different temperatures and droplet volumes. In the limits $V^{\text{I}}/V \to 0$ and $V^{\text{I}}/V \to 1$, the phase-separated state approaches the homogeneous one, thus distribution distance vanishes. Notice that the volume corresponding to the maximum distribution distance shifts towards lower values.

We now compare systems with the phase behaviour of systems with the same interaction propensity χ, but with increasing aggregation strength. This is achieved by increasing the ratio e_{int}/χ containing the energy associated with internal bonds e_{int} see Eq. (5.7). In figure Fig. 5.2 c) we show the binodal lines corresponding to $e_{\text{int}}/\chi = 0.5, -1 and -2$. We compare it to a binary mixture made of monomers and solvent only (black curve), which corresponds to an infinite energy penalty for bond formation, i.e. $e_{\text{int}}/\chi \to \infty$. The region enclosed by the binodal, corresponding to phase separation, expands even in the case of slightly penalised bond formation $e_{\text{int}}/\chi = 0.5$. This is can be explained considering that cluster formation, even if energetically disfavoured, reduces the mixing entropy (see the first term in (5.9)). In the region enclosed by the back curve, we can compare the total droplet volumes in the binary mixture (composed of monomers only), $e_{\text{int}}/\chi \to \infty$, and in the mixtures with aggregates $e_{\text{int}}/\chi = -1$. At low ϕ_{tot}, V^{I}/V is greater in the presence of aggregates with respect to the binary mixture while, above the dashed grey line, aggregates lead to smaller V^{I}/V. Finally, in Fig. 5.2 d), we quantify the upshift in critical temperature and downshift in critical volume fraction observed lowering $e_{\text{int}}/\chi = -1$, i.e. making aggregates more energetically favourable.

Critical volume fractions lower than $1/2$ and critical temperatures higher than $T_0/2$ are reminiscent of mixtures containing two components with unequal molecular volumes. Indeed aggregation causes the average molecular volume of the species in the mixture to exceed the solvent molecular volume. It must be noticed, however, that in our theory the size distribution, and hence average molecular volume, is different in the two phases.

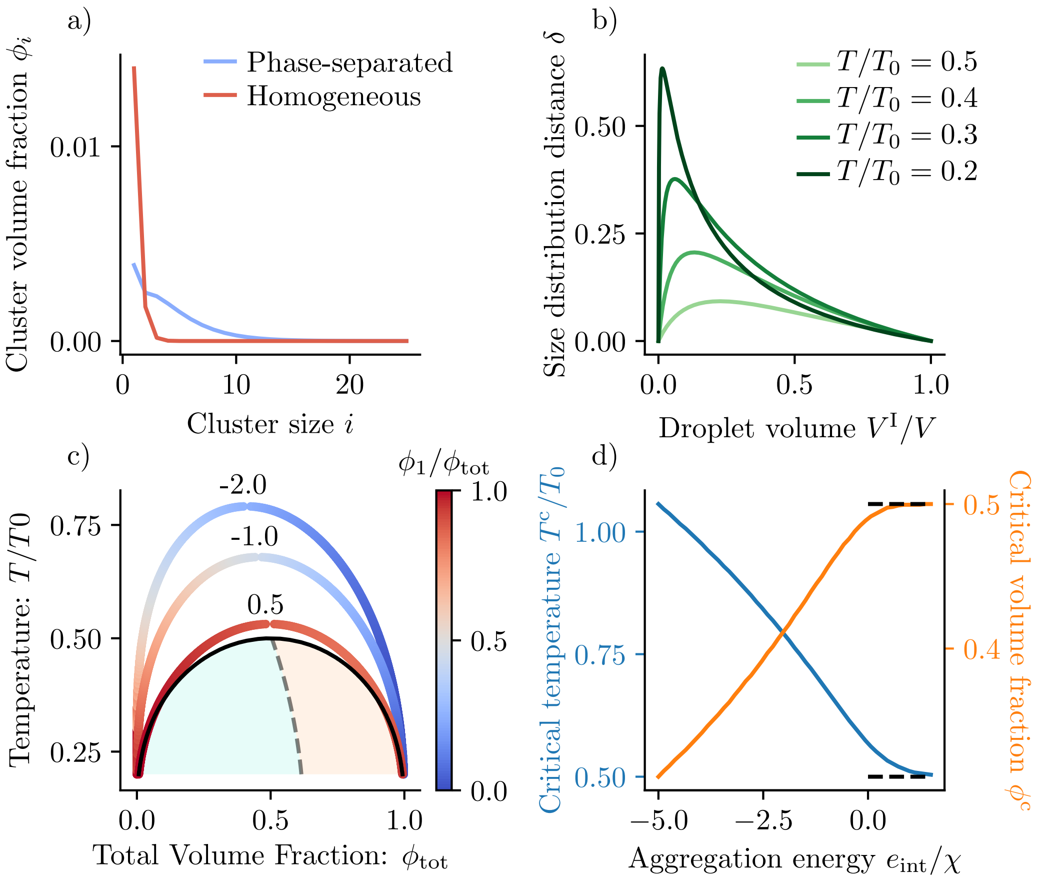

FIGURE 5.3: **The interplay between phase separation and aggregation**. a) Comparison between the size distribution in a homogeneous system, and in the corresponding phase-separated system (averaged in both compartments). Here, we consider rod-like aggregates (d=1), $M \to \infty$, and the same parameters as in Fig. 5.2. Furthermore, both distributions correspond to $\phi_{\mathrm{tot}} = 0.016$ and $T/T_0 = 0.2$. We notice that the presence of compartments can favour aggregate formation, even when the corresponding homogeneous mixture is populated mainly by monomers. The difference in distributions can be quantified by means of the functional distance defined in Eq. (5.17). b) The magnitude of this distance depends on the droplet size, and on the temperature chosen. The volume corresponding to the maximum distribution distance shifts towards lower values with decreasing temperature $T/T0$. The distributions separated by the maximum distance, for $T/T0 = 0.2$, are the ones displayed in a). c) Comparison between three binodal lines corresponding to aggregation energies $e_{\mathrm{int}}/\chi = 0.5, -1, -2$ (coloured curve) and the reference binary mixture composed of monomers and solvent only (black curve). The latter can be associated with the limit $e_{\mathrm{int}}/\chi \to \infty$. The region enclosed by the binodal, corresponding to phase separation, expands even if aggregates are slightly penalised $e_{\mathrm{int}}/\chi = 0.5$. This can be explained by the entropic advantage caused by size polydispersity. Aggregation influences also droplet size: the area shaded in blue corresponds to V^{I}/V greater in the presence of aggregates with respect to the reference binary mixture. On the other hand, above the dashed grey line (orange area) aggregation lead to smaller V^{I}/V. d) Dependence of the critical volume fraction and critical temperature on the aggregation energy e_{int}/χ. Decreasing e_{int}/χ, T^c and ϕ^c deviate from the reference values (black dashed lines) corresponding to a binary mixture with monomers and solvent only ($e_{\mathrm{int}}/\chi \to \infty$).

5.1.6 Gelation transition in the limit of infinitely large aggregates

As outlined in discussing Fig. 5.1, in the case of a homogeneous mixture populated by disk-like (d=2) and spherical (d=3) aggregates with maximum size $M = 50$, above ϕ^* the size distribution becomes bimodal. As shown in App. D, the peak appearing at the upper bound $M = 50$ is a finite-size manifestation of the gelation transition occurring in the limit $M \to \infty$. In App. D, we also introduced ϕ^{GS}, which estimates the volume fraction corresponding to gel formation, after which the system cannot be described as homogeneous anymore. We now study the onset of gelation in systems that can phase separate, and locate both these phase transitions in the same phase diagram.

In the limit $M \to \infty$, calculating the phase diagram for 2- and 3-dimensional aggregates becomes difficult. The reason is that, for $d > 1$ case, it is not possible to calculate the series in Eq. (5.3). To cope with this limitation, introduce the following free energy:

$$f^{\mathrm{sg}} = f + f^{\mathrm{gel}} \,, \tag{5.18}$$

where f is defined in Eq. 5.9, with M finite, and

$$f^{\mathrm{gel}} = \frac{\omega_\infty}{v_0}\, \delta\left(1 - \phi_{\mathrm{tot}}\right) \,, \tag{5.19}$$

can be thought of as the free energy of a state with no solvent, where all monomers belong to an aggregate of size $i \to \infty$. In fact, the free energy in Eq. 5.9, in the limit $\phi_i = 0$ for all finite i, and $\phi_{\mathrm{tot}} = 1$, gives $f = \omega_\infty / v_0$. We can now perform the Maxwell construction (see Eqs. (5.15)) using the free energy f^{sg} in Eq. 5.18, which accounts for aggregates up to a finite cut-off M and for an infinitely large cluster. In Fig. 5.4, we show the result of this construction for three different temperature values. The phase diagram is displayed Fig. 5.5 a). There, the coloured curve represents the binodal, and its colour code depicts the monomer fraction $\phi_1/\phi_{\mathrm{tot}}$ in the coexisting phases. The grey dashed line represents $\phi^{\mathrm{SG}}(T)$, introduced in App. D. In homogeneous systems, ϕ^{SG} estimates the volume fraction at which the gel appears. In phase-separating systems, on the other hand, gelation can be considered as a special case of phase coexistence between a dilute phase (the "sol") in which $\phi^{\mathrm{sol}} < 1$ and the gel phase, corresponding to $\phi^{\mathrm{gel}} = 1$.

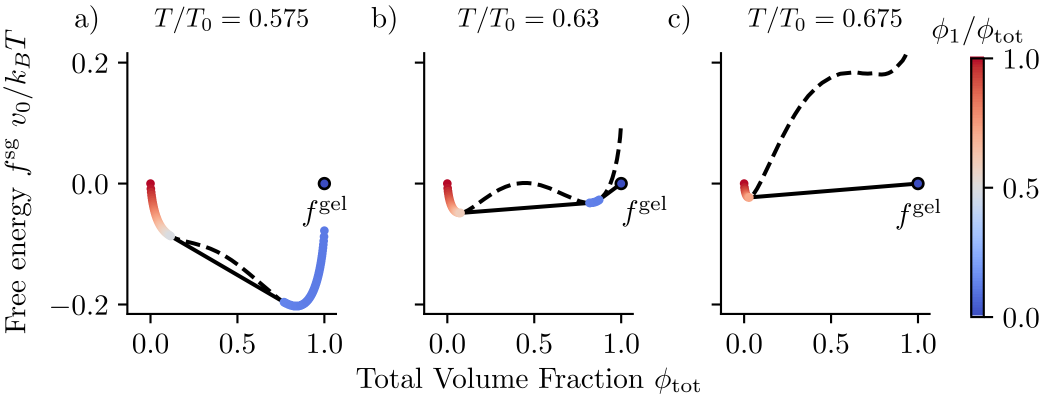

FIGURE 5.4: **Free energy for disk-like (d=2) and spherical (d=3) aggregates.** Illustration of f^{sg} defined in Eq. (5.18), for three different temperatures. This free energy includes contributions coming from clusters up to size $M = 50$, f, and from a macroscopic cluster, f^{gel}. Here, dashed lines correspond to unstable free energy branches, while black lines connect coexisting phases. Furthermore, we have set $\omega_\infty = 0$. a) At high temperatures both coexisting phases have $\phi_{\mathrm{tot}} < 1$. b) At intermediate temperatures, there are two ϕ_{tot} domains corresponding to the coexistence of qualitatively different phases. For intermediate ϕ_{tot} values, $\phi_{\mathrm{tot}} < 1$ in both coexisting phases, as in a). At higher ϕ_{tot}, instead, a phase (the "sol") with $\phi_{\mathrm{tot}}^{\mathrm{sol}} < 1$ coexists with the gel, corresponding to $\phi_{\mathrm{tot}}^{\mathrm{gel}} < 1$. c) At lower temperatures, only the "gel-sol" coexistence is present.

The area in the phase diagram where the gel is present is shaded in blue and labelled as "sol-gel" in Fig. 5.5 a). There we show that at high ϕ_{tot}, lowering the temperature leads to a transition from the homogeneous state to the sol-gel coexistence. Notice that, in this regime, the binodal is very close to the volume fraction estimate ϕ^{SG}. For intermediate volume fractions, instead, the system transit first in a region, shaded light blue and labelled as "sol-sol" in Fig. 5.5 a), corresponding to two-phase coexistence where $\phi_{\mathrm{tot}} < 1$ in both phases. In Fig. 5.5 b) we display aggregate size distribution representative of the "sol-sol" and "sol-gel" regions. Transitions from the "sol-sol" to the "sol-gel" region are accompanied by a jump in the dense phase total volume fraction $\phi_{\mathrm{tot}}^{\mathrm{I}}$, see Fig. 5.5 c) for an illustration.

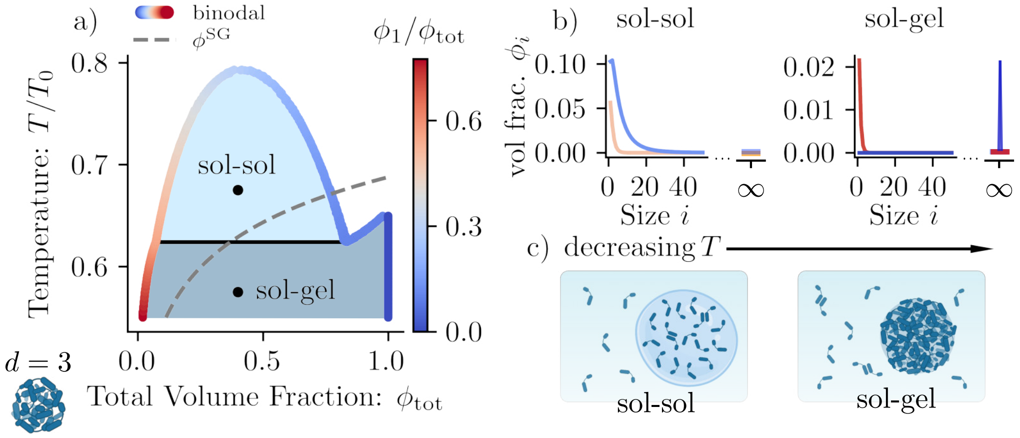

FIGURE 5.5: **Gelation transition in phase separating systems**. a) Phase diagram for disk-like (d=2) and spherical (d=3) aggregates in the limit $M \to \infty$, as a function of ϕ_{tot} and the rescaled temperature T/T_0 (with $T_0 = \chi/k_B$). The coloured curve represents the binodal, obtained performing the Maxwell construction (see Eqs. (5.15)) on the free energy f^{sg}, that accounts for the emergence of an infinite cluster. The colour code depicts the monomer fraction ϕ_1/ϕ_{tot} in the phases. The grey dashed line represents $\phi^{SG}(T)$, introduced in App. D. ϕ^{SG} is an estimate of the volume fraction at which the gelation transition emerges in homogeneous systems. In the region labelled as "sol-sol", the system demixes into two phases both populated mainly by monomers, see panel b), with $\phi_{tot}^{I/II} < 1$. In the region labelled as "sol-gel", on the other hand, a phase (the "sol"), obeying $\phi_{tot}^{sol} < 1$, coexists with a phase (the "gel") that is a macroscopic aggregate, occupying a finite portion of the system (V^{gel}/V) and containing no solvent ($\phi_{tot}^{sol} = 1$). The latter scenario is represented in panel b), right side. c) Lowering the temperature allows moving from the "sol-sol" to the "sol-gel" region. This transition is accompanied by a jump in the dense phase total volume fraction, from $\phi_{tot}^{I} < 1$ to $\phi_{tot}^{gel} = 1$.

5.2 Aggregation kinetics at phase equilibrium

In this section, we consider systems that are initially composed of monomers only and study their relaxation to thermodynamic equilibrium. We assume a finite bound in aggregate size M and aggregates diffusion much faster than aggregate interconversion. The last assumption allows us to impose phase equilibrium at all times, and study the slow aggregation kinetics in the presence of spatial compartments. To this aim, we apply the theoretical framework developed in Sec. 2.2.2. We focus on control parameters choice such that the initial mixture, composed of monomers in solution, phase separates. Eq. (2.42) allows to write the evolution of volume fractions in both phases as follows:

$$\frac{\mathrm{d}\phi_i^{\mathrm{I/II}}}{\mathrm{d}t} = -j_i^{\mathrm{I/II}} + r_i^{\mathrm{I/II}} + \phi_i^{\mathrm{I/II}} \sum_{i=0}^{M} j_i^{\mathrm{I/II}} \,. \tag{5.20}$$

The rates $r_i^{\mathrm{I/II}}$ can be found evaluating Eq. (2.43) with the stoichiometric matrix in Eq. (5.2), to get:

$$
\begin{aligned}
r_1^{\mathrm{I/II}} &= -r_{2,1}^{\mathrm{I/II}} - \sum_{i=1}^{M-1} i\, r_{i+1,i}^{\mathrm{I/II}} \,, \\
r_i^{\mathrm{I/II}} &= (i-1)\, r_{i,i-1}^{\mathrm{I/II}} - i\, r_{i+1,i}^{\mathrm{I/II}} \,, \qquad \text{for } i = 2, ..M-1 \,, \\
r_M^{\mathrm{I/II}} &= (M-1)\, r_{M,M-1}^{\mathrm{I/II}} \,.
\end{aligned}
\tag{5.21}
$$

where, $r_{i,i+1}$ quantifies the net reaction flux associated with the reaction $C_1 + C_i \rightleftharpoons C_{i+1}$, and reads

$$
r_{i+1,i}^{\mathrm{I/II}} = \Lambda_i^{\mathrm{I/II}} \left[1 - \exp\left(\frac{(i+1)\bar{\mu}_{i+1}^{\mathrm{I/II}} - i\bar{\mu}_i^{\mathrm{I/II}} - \bar{\mu}_1^{\mathrm{I/II}}}{k_B T} \right) \right] . \tag{5.22}
$$

To gain some intuition on the reaction fluxes, we can substitute the expression for the chemical potential derived from Eq. (5.9), leading to

$$
r_{i+1,i}^{\mathrm{I/II}} = \Lambda_i^{\mathrm{I/II}} \left(1 - \frac{i}{i+1} \frac{\phi_{i+1}^{\mathrm{I/II}}}{\phi_i^{\mathrm{I/II}}\, \phi_1^{\mathrm{I/II}}} K_i^{-1} \right) \tag{5.23}
$$

Where we have introduced

$$
K_i = \exp\left(1 - \frac{(i+1)\omega_{i+1} - i\omega_i - \omega_1}{k_B T} \right) . \tag{5.24}
$$

We chose $\Lambda_i = \phi_i \phi_1 K_i / \phi_i \, \Lambda$ in order to recover a finite rate in the limit $\phi_1, \phi_i \ll 1$. We can then recast the flux in Eq.s (5.22) as

$$
r_{i+1,i}^{\mathrm{I/II}} = \Lambda \left(\frac{\phi_i}{i}^{\mathrm{I/II}} \phi_1^{\mathrm{I/II}} K_i - \frac{\phi_{i+1}^{\mathrm{I/II}}}{i+1} \right) . \tag{5.25}
$$

We finally identify K_i, defined in Eq. (5.24) as the aggregation kernel. In general, this kernel depends on the cluster size i, but in the simple case of rod-like assemblies, $d = 1$ in Eq. (5.6), we get a constant kernel [1]

$$
K_i = K = \exp\left(1 + \frac{\Delta\omega}{k_B T} \right) . \tag{5.26}
$$

Having obtained the form of $r_{i,i+1}$ as functions of the volume fraction, we determine the diffusive currents $j_i^{\mathrm{I/II}}$ through Eqs. (2.47). The expressions for $j_i^{\mathrm{I/II}}$ found in this way guarantee that the mixture remains at phase equilibrium at all times.

In Fig. 5.6, we display an example of the slow relaxation to thermodynamic equilibrium in a compartmentalized system, with a maximum aggregate size $M = 15$. At $t = t_0$, the system is composed of two compartments at phase equilibrium, both filled with monomers and solvent. In a) and b) we show how the size distribution in phases II and I, respectively, changes in time. At late times, the distributions approach their equilibrium values (black dots), calculated as described in Sec. 5.1.4. The area below the curves in a) and b) represents the total macromolecule volume fraction in the two phases, $\phi_{\text{tot}}^{\text{I/II}}$. In Fig. 5.6 c) we show time traces of $\phi_{\text{tot}}^{\text{I/II}}$, showing that the ϕ_{tot}-dense phase (I) becomes denser while the dilute phase (II) becomes more dilute. As a consequence, phase volumes change slightly, in a non-monotonous way, see Fig. 5.6 d). In conclusion, for this choice of parameters, aggregates selectively appear in the dense phase, increasing its volume V^{I} and total volume fraction $\phi_{\text{tot}}^{\text{I}}$, as depicted in Fig. 5.6 e), we illustrate the changes in phase volume and composition as aggregation proceeds. With our choice of parameters, aggregates selectively appear in the dense phase, causing its volume V^{I} and total volume fraction $\phi_{\text{tot}}^{\text{I}}$ to increase.

---

[1] This may be the reason why, in aggregation and fragmentation literature, size-independent kernels define the so-called string model [58].

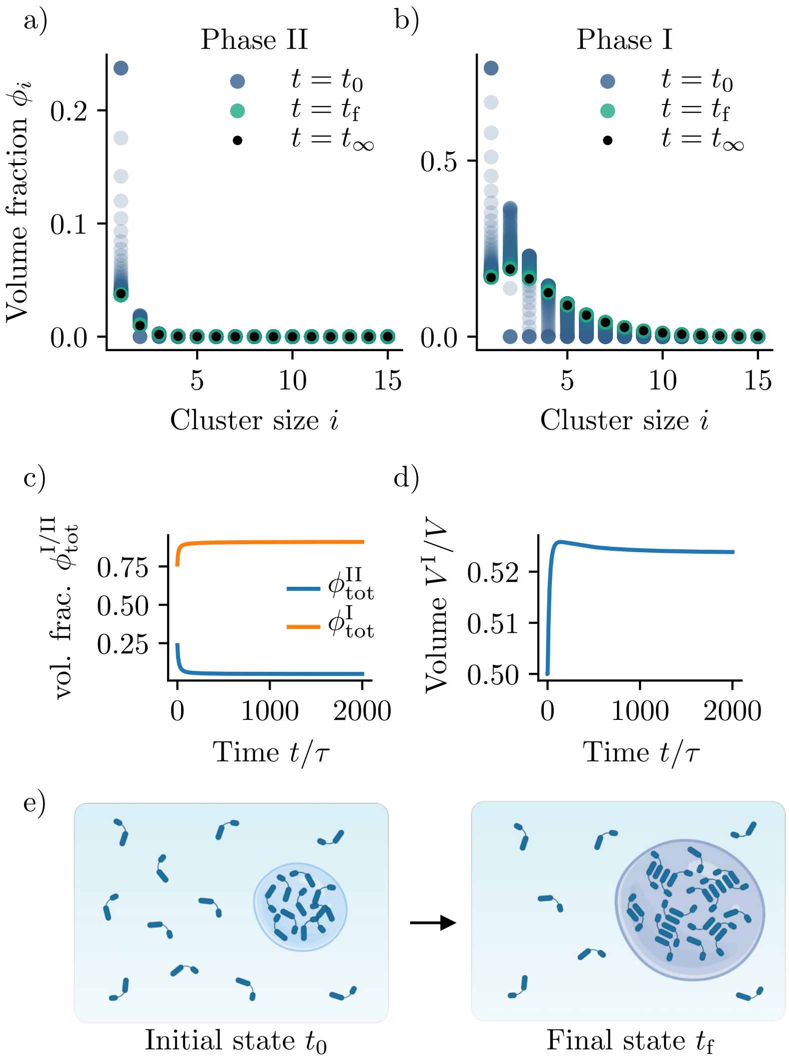

FIGURE 5.6: **Aggregation kinetics at phase equilibrium**. Assuming that aggregate diffusion is fast, we study the slow relaxation to chemical equilibrium in a compartmentalized system. In a) and b) we show the time evolution of the size distribution in phases II and I, respectively, starting from an initial state composed of monomers and solvent only. Black dots show the equilibrium distributions calculated in Sec. 5.1.4. c) As time proceeds, the total macromolecule volume fraction in the two phases, $\phi_\mathrm{tot}^\mathrm{I/II}$ changes. In particular, the ϕ_tot-dense phase (I) becomes denser while the dilute phase (II) becomes more dilute. Concomitantly, d) phase volumes change slightly, in a non-monotonous way. In conclusion, for this choice of parameters, aggregates selectively appear in the dense phase, increasing its volume V^I and total volume fraction $\phi_\mathrm{tot}^\mathrm{I}$.

Chapter 6

Conclusion and future perspectives

In this thesis, we studied the complexity of mixtures with more than two components that undergo chemical reactions that relax towards equilibrium and that are maintained away from equilibrium.
In chapter 2, we have started with a review of the mean-field approach to discuss thermodynamic equilibrium and reviewed the upper bound on the number of phases that can coexist in a multi-component mixture at phase equilibrium. We discussed how chemical equilibrium leads to a reduction in the number of degrees of freedom needed to characterise the state of a mixture, and how this reduction affects the maximum number of phases that can coexist. We then presented a few selected approaches to study the relaxation dynamics toward the equilibrium state.

In chapter 3, we applied these concepts to a minimal system composed of a solvent and a macromolecule that can exist in two different molecular states. We modeled the conversion between these two states with a chemical reaction, and study the equilibrium behaviour of the mixture. We have emphasised the qualitative differences between the phase behaviour of binary mixtures and ternary mixtures at chemical equilibrium, despite both their equilibrium state can be characterised by the same number of degrees of freedom. In particular, we discussed how molecular transitions can control the relative amount of molecular states in both, the dilute and the dense phase as a function of temperature, leading to a reentrant phase behaviour. Strikingly, if both components have similar interaction propensities with the solvent, the dense phase can undergo a discontinuous switch between states where most macromolecules are either in one or the other state. We then generalised the mixture kinetics to account for the presence of a fuel component that is maintained at a constant level. Continuous fuel replenishment leads to breaking the detailed balance of the reaction rates. We then probed the kinetics of systems initially at thermodynamic equilibrium, once the fuel is added to the system. In particular, we have shown that a switch in phase composition can also be triggered via fuel – a more likely control pathway in living cells in contrast to temperature. Furthermore, driving the system out of equilibrium via fuel addition can change the number of distinct coexisting phases. In our example, in fact, releasing the constraints coming from the Gibbs phase rule, which allows three-phase coexistence only for fine-tuned values of the control parameters.

In chapter 4, chemical reactions with broken detailed balance of the rates lead to the emergence of stationary states different from spherical drops. We have then introduced the theoretical framework referred to as the effective droplet model and used it to characterise ring-like patterns. Intuitively, rings emerge because, due to chemical reactions, the volume fraction at the centre of droplets can cross the spinodal line and become unstable. Experimental evidence that similar patterns can emerge in mixtures leading to the formation of coacervate droplets coupled to a fuel reservoir has been recently found by the Boekhoven lab at TUM. For this reason, we conclude the chapter by showing that our theoretical framework can be used to recapitulate their experimental findings. Our key result is that we confirmed that such vacuoles are indeed non-equilibrium steady states where continuous chemical and diffusive fluxes prevent the vacuole from collapsing into a single spherical droplet.

In chapter 5, we developed a theory for aggregating units that can phase separate in the presence of a solvent. In this theory, the number of components M is equal to the maximum aggregate size. Furthermore, aggregates can convert into each other via monomer pick-up, described through a set of $(M-1)$ chemical reactions. We first characterise the equilibrium of the system in the limit $M \to \infty$. Focusing on two-phase coexistence, we show that the aggregate size distribution, in general, differs between the two phases. In particular, monomers are not necessarily the most abundant species, and distribution tails can deviate from the exponential decay known for classical assembly at dilute conditions. Third, we show that by lowering the temperature, the system can gelate, i.e., the dense phase becomes a single macroscopic aggregate. We then show an example of aggregation kinetics in the two phases, in the limit where the exchange between the phases is fast compared to the transition rate among clusters. In particular, we monitor two phases initially composed of monomer and solvent only, showing the evolution of size distributions, total volume fraction in the phases, and phase volumes.

This work set the foundation to investigate several questions at the interface between biology, chemistry, and physics in the future. For example, our framework for the interplay between aggregation and phase separation can be extended to more complex molecular assemblies that are composed of different monomers. Such monomers could correspond to different nucleotides, thus paving the way to study the interplay of oligonucleotide assembly and phase separation. Such studies are of particular importance for biomolecular condensates in cells since they are composed of various proteins, and mRNA of specific sequence patterns and lengths [9, 10]. Moreover, such an extended framework could also be applied to investigate the role of phase separation in the emergence of the first self-replicating RNA strands. Recently, we applied a simplified framework to make the first step in this direction; see Ref. [18].

Finally, our theoretical framework for aggregating and phase-separating mixtures can be extended by fuel-driven chemical reactions, following the concepts laid out in our studies of minimalistic chemical systems. We speculate that maintaining the formation of sequence-dependent and phase-separating assemblies out of equilibrium will give rise to complex-shaped assemblies that can carry specific sequence information – a complexity that is essential to understand processes in living cells and crucial to engineering life-like processes, such as synthetic cells.

Appendix A

Phase equilibrium in multicomponent mixtures

Here we perform the minimization of the free energy of a system where $n_{\rm p}$ phases coexist, namely

$$F = \sum_{\alpha=\rm I}^{n_{\rm p}} f^{\alpha} V^{\alpha} \,, \tag{A.1}$$

where we have introduced the notation $f^{\alpha} = f(\{\phi_i^{\alpha}\})$, and the index α runs over all coexisting phases, i.e. $\alpha = \mathrm{I}, \dots, n_{\rm p}$. We impose volume and material conservation, that read, respectively

$$V\bar{\phi}_i = \sum_{\alpha} V^{\alpha} \phi_i^{\alpha} \,, \tag{A.2a}$$

$$V = \sum_{\alpha} V^{\alpha} \,. \tag{A.2b}$$

We adopt as independent variables v^{α} and $\{\phi_i^{\alpha}\}$, with $\alpha > \mathrm{I}$, and use the constraints in Eqs. (A.2) to express the dependent variables as

$$\phi^{\rm I} = \frac{V\bar{\phi}_i - \sum_{\alpha > \rm I} V^{\alpha} \phi_i^{\alpha}}{V - \sum_{\alpha > \rm I} V^{\alpha}} \,, \tag{A.3}$$

$$V^{\rm I} = V - \sum_{\alpha > \rm I} V^{\alpha} \,. \tag{A.4}$$

From which we derive the following expression, for $\alpha > \mathrm{I}$

$$\frac{\partial \phi_i^{\rm I}}{\partial \phi_j^{\alpha}} = -\frac{V^{\rm I}}{V^{\alpha}} \delta_{ij} \,, \qquad \frac{\partial \phi_i^{\rm I}}{\partial V^{\alpha}} = \frac{\phi_i^{\rm I} - \phi_i^{\alpha}}{V^{\rm I}} \,, \tag{A.5}$$

$$\frac{\partial V^{\rm I}}{\partial V^{\alpha}} = -1 \,, \qquad \frac{\partial V^{\rm I}}{\partial \phi_i^{\alpha}} = 0 \,. \tag{A.6}$$

We minimise the total free energy in Eq. (2.8) with respect to variation of ϕ_i^α, with $\alpha > 1$

$$\begin{aligned} 0 = \frac{\partial F}{\partial \phi_i^\alpha} &= \frac{\partial\left(f^{\mathrm{I}} V^{\mathrm{I}}\right)}{\partial \phi_i^\alpha} + \sum_{\beta > \mathrm{I}} \frac{\partial\left(f^\beta V^\beta\right)}{\partial \phi_i^\alpha} \\ &= V^{\mathrm{I}}\left(-\frac{\partial f^{\mathrm{I}}}{\partial \phi_i^{\mathrm{I}}} + \frac{\partial f^\alpha}{\partial \phi_i^\alpha}\right) \\ &= \frac{V^{\mathrm{I}}}{v_i}\left(-\mu_i^{\mathrm{I}} + \mu_i^\alpha\right), \end{aligned} \tag{A.7}$$

where we made use of the exchange chemical potential, defined in Eq. (2.5), and introduced the notation $\mu_i^\alpha = \mu_i\big(\{\phi_j^\alpha\}\big)$. Having justified Eq. (2.9a), we now minimize the total free energy with respect to variation of V^α, with $\alpha > 1$

$$\begin{aligned} 0 = \frac{\partial F}{\partial V^\alpha} &= \frac{\partial\left(f^{\mathrm{I}} V^{\mathrm{I}}\right)}{\partial V \alpha} + \sum_{\beta > \mathrm{I}} \frac{\partial\left(f^\beta V^\beta\right)}{\partial V^\alpha} \\ &= -f^{\mathrm{I}} + \sum_i \frac{\partial f^{\mathrm{I}}}{\partial \phi_i^{\mathrm{I}}}\left(\phi_i^{\mathrm{I}} - \phi_i^\alpha\right) + f^\alpha \\ &= -f^{\mathrm{I}} + \sum_i \frac{\partial f^{\mathrm{I}}}{\partial \phi_i^{\mathrm{I}}}\phi_i^{\mathrm{I}} + f^\alpha - \sum_i \frac{\partial f^{\mathrm{I}}}{\partial \phi_i^{\mathrm{I}}}\phi_i^\alpha \\ &= \Pi^{\mathrm{I}} - \Pi^\alpha, \end{aligned} \tag{A.8}$$

where we have used Eq. (A.7), the definition of osmotic pressure in Eq. (2.7), and the notation $\Pi^\alpha = \Pi\big(\{\phi_j^\alpha\}\big)$. The last equality proves Eq. (2.9b)in the main text.

Appendix B

Derivation of equilibrium fuel profile

We impose fuel conservation by keeping the spatial average of Eq. (3.12) fixed and equal to $\bar{\phi}_{\text{F}}$. This implies $\Gamma + \Upsilon\bar{\phi}_{\text{tot}} = 1$, with $\bar{\phi}_{\text{tot}}$ being the total average volume fraction of macromolecules (see Eq. (2.4)). In Eq. (3.12) we notice the coefficient Υ encodes correlations between fuel ϕ_{F} and total macromolecular material ϕ_{tot}. Maximal spatial correlation between ϕ_{F} and ϕ_{tot} is reached maximizing Υ with the constraints $\Gamma + \Upsilon\bar{\phi}_{\text{tot}} = 1$ and $0 < \phi_{\text{F}}(x) < 1$ everywhere in space. This leads to $\Gamma = 0$ and $\Upsilon = 1/\bar{\phi}_{\text{tot}}$. Maximal anti-correlation between ϕ_{F} and ϕ_{tot} is reached minimizing Υ with the same constraints, leading to $\Gamma = -\Upsilon = 1/(1 - \bar{\phi}_{\text{tot}})$. Finally, no correlation between ϕ_{F} and ϕ_{tot}, i.e. fuel homogeneously distributed in the system, is achieved for $\Upsilon = 0$ and, due to fuel conservation, $\Gamma = 1$. This explains the choices of Γ and Υ introduced at the end of Sec. 3.2.

At equilibrium and for the case where the fuel has only weak effects on the chemical flux (i.e., $k_{\leftarrow} \simeq 0, k_{\rightarrow} \simeq 0$), we can make the connection between the coefficients Γ and Υ in Eq. (3.12) and the fuel partitioning even more explicit. We recall the definition of partitioning coefficient of the fuel component, $P_{\text{F}} = \phi_{\text{F}}^{\text{I}}/\phi_{\text{F}}^{\text{II}}$, and of the total concentration, $P_{\text{tot}} = \phi_{\text{tot}}^{\text{I}}/\phi_{\text{tot}}^{\text{II}}$. Here, I and II denote the dense and the dilute phase, respectively. We can express the fuel and total volume fractions in I and II, respectively, in terms of the average fuel volume fraction $\bar{\phi}_{\text{F}}$ that is considered to be maintained at some constant value, and the conserved total volume fraction $\bar{\phi}_{\text{tot}}$:

$$\phi_i^{\text{I}} = \zeta_i \, P_i \, \bar{\phi}_i \, , \tag{B.1}$$

$$\phi_i^{\text{II}} = \zeta_i \bar{\phi}_i \, , \tag{B.2}$$

where $i = \{\text{F}, \text{tot}\}$. The partition degree [59] reads

$$\zeta_i = \frac{1}{1 + (P_i - 1)\frac{V^{\text{I}}}{V}} \, , \tag{B.3}$$

where the phase-separated volume reads, in the limit of dilute fuel

$$V^{\mathrm{I}} = V \frac{\bar{\phi}_{\mathrm{tot}} - \phi_{\mathrm{tot}}^{\mathrm{II}}}{\phi_{\mathrm{tot}}^{\mathrm{I}} - \phi_{\mathrm{tot}}^{\mathrm{II}}} \, . \tag{B.4}$$

Evaluating Eq. (3.12) inside and outside the dense phase, we find:

$$\Gamma = \zeta_{\mathrm{F}} \left(1 - \frac{P_{\mathrm{F}} - 1}{P_{\mathrm{tot}} - 1} \right) \, , \tag{B.5}$$

$$\Upsilon = \frac{\zeta_{\mathrm{F}}}{\zeta_{\mathrm{tot}}} \frac{1}{\bar{\phi}_{\mathrm{tot}}} \frac{P_{\mathrm{F}} - 1}{P_{\mathrm{tot}} - 1} \, . \tag{B.6}$$

If the fuel partitions equally strong into both phases ($P_{\mathrm{F}} = 1$, and thus $\zeta_{\mathrm{F}} = 1$), we get $\Gamma = 1$ and $\Upsilon = 0$. Consistently, this corresponds to a homogeneous fuel profile, $\phi_{\mathrm{F}}(x) = \bar{\phi}_{\mathrm{F}}$. For a fixed $P_{\mathrm{tot}} > 1$, the fuel partition coefficient P_{F} determines the localization of the fuel. In particular, $P_{\mathrm{F}} > 1$, corresponds to fuel co-localizing with the total volume fraction ϕ_{tot} with $\Upsilon > 0$. On the contrary, when $P_{\mathrm{F}} < 1$, the fuel and the total volume fraction ϕ_{tot} anti-co-localize with $\Upsilon < 0$.

Appendix C

One-dimensional aggregates infinite size

In the case of rod-like aggregates ($d = 1$), we can analytically derive the size distribution in the limit $M \to \infty$. In fact, for $d = 1$ the chemical equilibrium in (5.11), simplifies to

$$\phi_i = i \left(\frac{\phi_1}{\phi^*} \right)^i \phi^*, \tag{C.1}$$

And the series defined in the conservation law, (5.3), can be explicitly computed, leading to

$$\phi_{\text{tot}} = \frac{\phi_1}{\left(1 - \frac{\phi_1}{\phi^*}\right)^2} \,. \tag{C.2}$$

This can be inverted leading to

$$\frac{\phi_1}{\phi^*} = \frac{1 + 2\frac{\phi_{\text{tot}}}{\phi^*} - \sqrt{1 + 4\frac{\phi_{\text{tot}}}{\phi^*}}}{2\frac{\phi_{\text{tot}}}{\phi^*}} \,. \tag{C.3}$$

As anticipated, in the regime $\phi_{\text{tot}} \ll \phi^*$, this leads to monomers taking up all the mass, namely $\phi_1 \simeq \phi_{\text{tot}}$, while for $\phi_{\text{tot}} \gg \phi^*$ we get $\phi_1 \simeq \phi^*$, and bigger aggregates start to be populated, see Fig. 5.1. The maximum of the volume fraction distribution in (C.1) can be obtained imposing $\partial_i \phi_i = 0$, leading to

$$i^{\max} = \frac{1}{\ln\left(\phi^*/\phi_1\right)} \simeq \sqrt{\frac{\phi_{\text{tot}}}{\phi^*}} \,. \tag{C.4}$$

Where the approximation is obtained using (C.3) and expanding for $\phi_{\text{tot}}/\phi^* \gg 1$. The average can be calculated as well from its definition $\langle i \rangle = \sum i\phi_i / \sum \phi_i$, leading to

$$\langle i \rangle = \frac{\phi_1}{\phi_{\text{tot}}} \frac{3 - \phi_1/\phi^*}{(1 - \phi_1/\phi^*)^3} \simeq 2 i^{\max} \,, \tag{C.5}$$

again using (C.3) and expanding for $\phi_{\text{tot}}/\phi^* \gg 1$. We can derive an expression for the free energy as a function of the conserved quantity alone ϕ_{tot}, making use of Eq.(C.1) together with Eq.(C.3)

$$\begin{aligned} f = \frac{k_B T}{v_0} \Bigg[& (1-\phi_{\text{tot}}) \ln(1-\phi_{\text{tot}}) + \phi_{\text{tot}} \ln \frac{\phi_1}{\phi^*} \\ & - \frac{\phi_1}{1-\phi_1/\phi^*} + \frac{\chi}{k_B T} \phi_{\text{tot}} (1-\phi_{\text{tot}}) \Bigg] . \end{aligned} \tag{C.6}$$

Appendix D

Gelation transition for two and three-dimensional aggregates

We now prove the existence of a gelation transition for 2 and 3-dimensional aggregates, in the thermodynamic limit. For this purpose, we recall (5.11) and we scrutinize the series

$$\sum_{i=1}^{\infty} \phi_i = \sum_{i=1}^{\infty} i \left(\frac{\phi_1}{\phi^*}\right)^i \exp\left(\frac{\Delta\omega}{k_B T}\, i^{\frac{d-1}{d}} - 1\right) . \tag{D.1}$$

We notice that when $N \to \infty$, this series in converges only if $\phi_1/\phi^* \leq 1$. Thus we get an upper bound for the series, namely

$$\sum_{i=1}^{\infty} \phi_i \leq \sum_{i=1}^{\infty} i \exp\left(\frac{\Delta\omega}{k_B T}\, i^{\frac{d-1}{d}} - 1\right) \equiv \phi^{\mathrm{SG}} . \tag{D.2}$$

Approximating the series with the integral, we get an estimation of ϕ^{SG}

$$\phi^{\mathrm{SG}} = \begin{cases} 2\frac{\left(6-6\Delta\omega+3\Delta\omega^2-\Delta\omega^3\right)}{\Delta\omega^4}\phi^* & d=2\,, \\ -\frac{3}{2}\frac{\Delta\omega^3}{(2-2\Delta\omega+\Delta\omega^2)}\phi^* & d=3\,. \end{cases} \tag{D.3}$$

As outlined in the main section, the gelation transition occurs at $\phi^{\mathrm{SG}} \sim \phi^*$.

Bibliography

[1] David Foster Wallace. *This Is Water: Some Thoughts, Delivered on a Significant Occasion about Living a Compassionate Life*. Little, Brown, New York, 1st ed edition, 2009.

[2] Laura Tripaldi. *Parallel Minds: Discovering the Intelligence of Materials*. Urbanomic, Falmouth England, May 2022.

[3] Lars G. M. Pettersson. A Two-State Picture of Water and the Funnel of Life. In Leonid A. Bulavin and Limei Xu, editors, *Modern Problems of the Physics of Liquid Systems*, Springer Proceedings in Physics, pages 3–39, Cham, 2019. Springer International Publishing.

[4] Kyung Hwan Kim, Katrin Amann-Winkel, Nicolas Giovambattista, Alexander Späh, Fivos Perakis, Harshad Pathak, Marjorie Ladd Parada, Cheolhee Yang, Daniel Mariedahl, Tobias Eklund, Thomas. J. Lane, Seonju You, Sangmin Jeong, Matthew Weston, Jae Hyuk Lee, Intae Eom, Minseok Kim, Jaeku Park, Sae Hwan Chun, Peter H. Poole, and Anders Nilsson. Experimental observation of the liquid-liquid transition in bulk supercooled water under pressure. *Science*, 370(6519):978–982, November 2020.

[5] Ron Milo & Ron Philips. » What are the time scales for diffusion in cells?

[6] Clifford P. Brangwynne, Christian R. Eckmann, David S. Courson, Agata Rybarska, Carsten Hoege, Jöbin Gharakhani, Frank Jülicher, and Anthony A. Hyman. Germline P Granules Are Liquid Droplets That Localize by Controlled Dissolution/Condensation. *Science*, 324(5935):1729–1732, June 2009.

[7] Anthony A. Hyman, Christoph A. Weber, and Frank Jülicher. Liquid-Liquid Phase Separation in Biology. *Annual Review of Cell and Developmental Biology*, 30(1):39–58, October 2014.

[8] Salman F. Banani, Hyun O. Lee, Anthony A. Hyman, and Michael K. Rosen. Biomolecular condensates: Organizers of cellular biochemistry. *Nature Reviews Molecular Cell Biology*, 18(5):285–298, May 2017.

[9] Simon Alberti, Amy Gladfelter, and Tanja Mittag. Considerations and Challenges in Studying Liquid-Liquid Phase Separation and Biomolecular Condensates. *Cell*, 176(3):419–434, January 2019.

[10] Simon Alberti and Dorothee Dormann. Liquid–Liquid Phase Separation in Disease. *Annual Review of Genetics*, 53(1):171–194, December 2019.

[11] Avinash Patel, Hyun O. Lee, Louise Jawerth, Shovamayee Maharana, Marcus Jahnel, Marco Y. Hein, Stoyno Stoynov, Julia Mahamid, Shambaditya Saha, Titus M. Franzmann, Andrej Pozniakovski, Ina Poser, Nicola Maghelli, Loic A. Royer, Martin Weigert, Eugene W. Myers, Stephan Grill, David Drechsel, Anthony A. Hyman, and Simon Alberti. A Liquid-to-Solid Phase Transition of the ALS Protein FUS Accelerated by Disease Mutation. *Cell*, 162(5):1066–1077, August 2015.

[12] William M. Aumiller and Christine D. Keating. Phosphorylation-mediated RNA/peptide complex coacervation as a model for intracellular liquid organelles. *Nature Chemistry*, 8(2):129–137, February 2016.

[13] Byoung-jin Jeon, Dan T. Nguyen, Gabrielle R. Abraham, Nathaniel Conrad, Deborah K. Fygenson, and Omar A. Saleh. Salt-dependent properties of a coacervate-like, self-assembled DNA liquid. *Soft Matter*, 14(34):7009–7015, August 2018.

[14] Michi Nakata, Giuliano Zanchetta, Brandon D. Chapman, Christopher D. Jones, Julie O. Cross, Ronald Pindak, Tommaso Bellini, and Noel A. Clark. End-to-end stacking and liquid crystal condensation of 6 to 20 base pair DNA duplexes. *Science (New York, N.Y.)*, 318(5854):1276–1279, November 2007.

[15] G. Zanchetta, M. Nakata, M. Buscaglia, N. A. Clark, and T. Bellini. Liquid crystal ordering of DNA and RNA oligomers with partially overlapping sequences. *Journal of Physics: Condensed Matter*, 20(49):494214, November 2008.

[16] Dan T. Nguyen and Omar A. Saleh. Tuning phase and aging of DNA hydrogels through molecular design. *Soft Matter*, 13(32):5421–5427, August 2017.

[17] Zhongyang Xing, Alessio Caciagli, Tianyang Cao, Iliya Stoev, Mykolas Zupkauskas, Thomas O’Neill, Tobias Wenzel, Robin Lamboll, Dongsheng Liu, and Erika Eiser. Microrheology of DNA hydrogels. *Proceedings of the National Academy of Sciences*, 115(32):8137–8142, August 2018.

[18] Giacomo Bartolucci, Adriana Calaça Serrão, Philipp Schwintek, Alexandra Kühnlein, Yash Rana, Philipp Janto, Dorothea Hofer, Christof B. Mast, Dieter Braun, and Christoph A. Weber. Selection of prebiotic oligonucleotides by cyclic phase separation, September 2022.

[19] David Zwicker, Rabea Seyboldt, Christoph A. Weber, Anthony A. Hyman, and Frank Jülicher. Growth and division of active droplets provides a model for protocells. *Nature Physics*, 13(4):408–413, April 2017.

[20] Jonathan Bauermann, Christoph A. Weber, and Frank Jülicher. Energy and Matter Supply for Active Droplets. *Annalen der Physik*, 534(9):2200132, 2022.

[21] Richard P. Sear and José A. Cuesta. Instabilities in Complex Mixtures with a Large Number of Components. *Physical Review Letters*, 91(24):245701, December 2003.

[22] William M. Jacobs and Daan Frenkel. Phase Transitions in Biological Systems with Many Components. *Biophysical Journal*, 112(4):683–691, February 2017.

[23] Krishna Shrinivas and Michael P. Brenner. Phase separation in fluids with many interacting components. *Proceedings of the National Academy of Sciences*, 118(45):e2108551118, November 2021.

[24] Giorgio Carugno, Izaak Neri, and Pierpaolo Vivo. Instabilities of complex fluids with partially structured and partially random interactions. *Physical Biology*, 19(5):056001, September 2022.

[25] Paul J Flory. Thermodynamics of High Polymer Solutions. *The Journal of Chemical Physics*, 10(1):51–61, 1942.

[26] Maurice L. Huggins. Thermodynamic properties of solutions of long-chain compounds. *Annals of the New York Academy of Sciences*, 43(1):1–32, 1942.

[27] Michael Rubinstein and Ralph H. Colby. *Polymer Physics*. Oxford university press, Oxford, United Kingdom, 2003.

[28] Omar Adame-Arana, Christoph A. Weber, Vasily Zaburdaev, Jacques Prost, and Frank Jülicher. Liquid Phase Separation Controlled by pH. *Biophysical Journal*, 119(8):1590–1605, October 2020.

[29] Peng Gong and I. Szleifer. Competitive adsorption of model charged proteins: The effect of total charge and charge distribution. *Journal of Colloid and Interface Science*, 278(1):81–90, October 2004.

[30] Josiah Willard Gibbs. On the Equilibrium of Heterogeneous Substances. *Transactions of the Connecticut Academy of Arts and Sciences*, 3:300–320, 1879.

[31] Amir Faghri and Yuwen Zhang. 2 - Thermodynamics of multiphasic systems. In Amir Faghri and Yuwen Zhang, editors, *Transport Phenomena in Multiphase Systems*, pages 107–176. Academic Press, Boston, January 2006.

[32] Christoph A Weber, David Zwicker, Frank Jülicher, and Chiu Fan Lee. Physics of active emulsions. *Reports on Progress in Physics*, 82(6):064601, June 2019.

[33] Jonathan Bauermann, Christoph A. Weber, and Frank Jülicher. Energy and Matter Supply for Active Droplets. *Annalen der Physik*, 534(9):2200132, 2022.

[34] Y K Rao. Extended form of the Gibbs phase rule. *Chemical Engineering Education*, page 8, 1985.

[35] Joseph S. Alper. The Gibbs Phase Rule Revisited: Interrelationships between Components and Phases. *Journal of Chemical Education*, 76(11):1567, November 1999.

[36] Robert A. Alberty. *Thermodynamics of Biochemical Reactions*. John Wiley and Sons, New Jersey, United States, 2003.

[37] Jonathan Bauermann, Sudarshana Laha, Patrick M. McCall, Frank Jülicher, and Christoph A. Weber. Chemical Kinetics and Mass Action in Coexisting Phases, December 2021.

[38] Sybren Ruurds de Groot and Peter Mazur. *Non-Equilibrium Thermodynamics*. Courier Corporation, January 1984.

[39] J. S. Langer, M. Bar-on, and Harold D. Miller. New computational method in the theory of spinodal decomposition. *Physical Review A*, 11(4):1417–1429, April 1975.

[40] Giacomo Bartolucci, Omar Adame-Arana, Xueping Zhao, and Christoph A. Weber. Controlling composition of coexisting phases via molecular transitions. *Biophysical Journal*, 120(21):4682–4697, November 2021.

[41] Salman F. Banani, Allyson M. Rice, William B. Peeples, Yuan Lin, Saumya Jain, Roy Parker, and Michael K. Rosen. Compositional Control of Phase-Separated Cellular Bodies. *Cell*, 166(3):651–663, July 2016.

[42] Christopher R. Carlson, Jonathan B. Asfaha, Chloe M. Ghent, Conor J. Howard, Nairi Hartooni, Maliheh Safari, Alan D. Frankel, and David O. Morgan. Phosphoregulation of Phase Separation by the SARS-CoV-2 N Protein Suggests a Biophysical Basis for its Dual Functions. *Molecular Cell*, 80(6):1092–1103.e4, December 2020.

[43] Zhenying Liu, Shengnan Zhang, Jinge Gu, Yilun Tong, Yichen Li, Xinrui Gui, Houfang Long, Chuchu Wang, Chunyu Zhao, Jinxia Lu, Lin He, Ying Li, Zhijun Liu, Dan Li, and Cong Liu. Hsp27 chaperones FUS phase separation under the modulation of stress-induced phosphorylation. *Nature Structural & Molecular Biology*, 27(4):363–372, April 2020.

[44] Frank Jülicher, Armand Ajdari, and Jacques Prost. Modeling molecular motors. *Reviews of Modern Physics*, 69(4):1269–1282, October 1997.

[45] Anja Nenninger, Giulia Mastroianni, and Conrad W. Mullineaux. Size Dependence of Protein Diffusion in the Cytoplasm of Escherichia coli. *Journal of Bacteriology*, 192(18):4535–4540, September 2010.

[46] Mark J. Hubley, Timothy S. Moerland, and Richard C. Rosanske. Diffusion coefficients of atp and creatine phosphate in isolated muscle: Pulsed gradient 31p nmr of small biological samples. *NMR in Biomedicine*, 8(2):72–78, 1995.

[47] Sharon C. Glotzer, Dietrich Stauffer, and Naeem Jan. Monte Carlo simulations of phase separation in chemically reactive binary mixtures. *Physical Review Letters*, 72(26):4109–4112, June 1994.

[48] David Zwicker, Anthony A. Hyman, and Frank Jülicher. Suppression of Ostwald ripening in active emulsions. *Physical Review E*, 92(1):012317, July 2015.

[49] Xiaofeng Yang, Jia Zhao, and Qi Wang. Numerical approximations for the molecular beam epitaxial growth model based on the invariant energy quadratization method. *Journal of Computational Physics*, 333:104–127, March 2017.

[50] Xueping Zhao and Qi Wang. A second order fully-discrete linear energy stable scheme for a binary compressible viscous fluid model. *Journal of Computational Physics*, 395:382–409, October 2019.

[51] Jie Shen and Xiaofeng Yang. Numerical approximations of Allen-Cahn and Cahn-Hilliard equations. *Discrete and Continuous Dynamical Systems*, 28(4):1669, 2010.

[52] Elsen Tjhung, Cesare Nardini, and Michael E. Cates. Cluster Phases and Bubbly Phase Separation in Active Fluids: Reversal of the Ostwald Process. *Physical Review X*, 8(3):031080, September 2018.

[53] Evan Spruijt, Joris Sprakel, Martien A. Cohen Stuart, and Jasper van der Gucht. Interfacial tension between a complex coacervate phase and its coexisting aqueous phase. *Soft Matter*, 6(1):172–178, December 2009.

[54] Oliver Beutel, Riccardo Maraspini, Karina Pombo-García, Cécilie Martin-Lemaitre, and Alf Honigmann. Phase Separation of Zonula Occludens Proteins Drives Formation of Tight Junctions. *Cell*, 179(4):923–936.e11, October 2019.

[55] Mrityunjoy Kar, Furqan Dar, Timothy J. Welsh, Laura Vogel, Ralf Kühnemuth, Anupa Majumdar, Georg Krainer, Titus M. Franzmann, Simon Alberti, Claus A. M. Seidel, Tuomas P. J. Knowles, Anthony A. Hyman, and Rohit V. Pappu. Phase separating RNA binding proteins form heterogeneous distributions of clusters in subsaturated solutions, February 2022.

[56] Jacob N. Israelachvili. *Intermolecular and Surface Forces*. Academic Press, May 2015.

[57] Dan Deviri and Samuel A. Safran. Equilibrium size distribution and phase separation of multivalent, molecular assemblies in dilute solution. *Soft Matter*, 16(23):5458–5469, 2020.

[58] Pavel L. Krapivsky, Sidney Redner, and Eli Ben-Naim. *A Kinetic View of Statistical Physics*. Cambridge University Press, Cambridge, 2010.

[59] Christoph Weber, Thomas Michaels, and L Mahadevan. Spatial control of irreversible protein aggregation. *eLife*, 8:e42315, May 2019.

Selbständigkeitserklärung

Hiermit versichere ich, dass ich die vorliegende Arbeit ohne unzulässige Hilfe Dritter und ohne Benutzung anderer als der angegebenen Hilfsmittel angefertigt habe; die aus fremden Quellen direkt oder indirekt übernommenen Gedanken sind als solche kenntlich gemacht. Die Arbeit wurde bisher weder im Inland noch im Ausland in gleicher oder ähnlicher Form einer anderen Prüfungsbehörde vorgelegt. Die Arbeit wurde in Dresden am Max-Planck-Institut für Physik komplexer Systeme unter der Betreuung von Prof. Dr. Frank Jülicher angefertigt.

Giacomo
Dresden, October 2022